



ScuDo
Scuola di Dottorato ~ Doctoral School
WHAT YOU ARE, TAKES YOU FAR



Doctoral Dissertation
Doctoral Program in Materials Science and Technology (33.rd cycle)

Nano-and micro-particles separation in acoustofluidic devices

A numerical evaluation of different microfluidic strategies

Luca Spigarelli

* * * * *

Supervisors

Prof. F.C. Pirri, Supervisor
Prof. G. Canavese Co-supervisor

Doctoral Examination Committee:

Prof. D. Carugo, Referee, UCL School of Pharmacy
Prof. J. Nilsson, Referee, Lund University
Prof. A. Troia, INRiM
Prof. S. Gonella, University of Minnesota
Prof. W. De Malsche, Vrije Universiteit Brussel

Politecnico di Torino
April 18,2021

This thesis is licensed under a Creative Commons License, Attribution - Noncommercial-NoDerivative Works 4.0 International: see www.creativecommons.org. The text may be reproduced for non-commercial purposes, provided that credit is given to the original author.

I hereby declare that, the contents and organisation of this dissertation constitute my own original work and does not compromise in any way the rights of third parties, including those relating to the security of personal data.

..... *Luca Spigarelli*

Luca Spigarelli
Turin, April 18, 2021

Acknowledgements

It is always both the best and worst moment when you start to think about acknowledgements. It means that your journey is over and another has to start. As always a lot of persons pass through this work and hopefully I will write about all without missing anyone.

I want to begin with my supervisors: Candido Fabrizio Pirri and Giancarlo Canavese. I would to thank them because they were always open for confrontation, giving me the right suggestion for going on, for thinking and improving myself. They gave me trust, even when I didn't believe in myself, and I will always be grateful for that.

To Per Augustsson, my Swedish supervisor. Literally speaking, I was not his PhD student but he always helped me to feel as part of his beautiful group. I got pushed forward and forward with his thoughts and curiosity. I can say that without him this work would not be the same. I would to thank also my colleagues in Lund University: Mahdi, Wei, Enrico, Franziska and Richard. It is beautiful when everyone in a group can give you something different to improve yourself and push you over your own limits.

To my office mates in Politecnico di Torino: Roberto Speranza, Alessandro Pedico, Marta Canta, Bianca Dumontel, Veronica Vighetto, Luisa Racca, Federica Barbaresco, Andrea Ancona. They changed at my sight a work environment in a friendly place. A special thank goes to Pietro. He is an unbelievable person: full of curiosity, knowledge and patience. I owe to him great part of my results, without him I would not be able to go on.

To the colleagues at Chilab: Valentina Bertana, Alberto Ballesio and Giorgio Scordo. Obviously to Matteo Parmeggiani, a friend more than a colleague.

I cannot forget Nicolò Vasile. He literally helped me to have a huge part of the presented data and when every numerical model scared like a monster he was there to support me.

*I would like to dedicate
this thesis to my loving
parents, to Chiara and
Damiano. You are my
strength.*

*"To see the world, things dangerous to come
to, to see behind walls, draw closer, to find
each other, and to feel. That is the purpose of
life."*

Contents

List of Tables	IX
List of Figures	X
1 Introduction	3
1.1 Exosomes	3
1.2 Separation of nanoparticles with microfluidics	7
1.2.1 Passive Separation	8
1.2.2 Size-exclusion devices for nanoparticles separation - An example of passive microfluidic technique	11
1.2.3 Active Separation	12
1.2.4 Acoustophoresis in BAW devices for particle manipulation - An example of active microfluidic technique	18
2 Theoretical Background	27
2.1 Microfluidic Theory	27
2.1.1 The continuum hypothesis	29
2.1.2 The continuity equation	30
2.1.3 The Navier-Stokes equations	30
2.1.4 Stokes Flow and Drag Force	31
2.2 Acoustofluidic Theory	32
2.2.1 Basic governing equations - Conservation of mass and momentum	33
2.2.2 Basic governing equations - Diffusive and advective transport of solute	33
2.2.3 Acoustic wave propagation	34
2.2.4 Acoustic energy density in the fluid domain	38
2.2.5 The acoustic radiation force and the acoustic contrast factor	38
2.2.6 Inhomogeneous fluids and acoustic streaming suppression	40
2.3 Numerical Model Background	41
2.3.1 The Finite Element Method	41
2.3.2 The Finite Volume Method	43

3	Size Exclusion Passive Microfluidic Device	47
3.1	Numerical model	48
3.1.1	Boundary conditions and convergence analysis	49
3.2	Materials and methods	50
3.2.1	Numerical optimization of the geometry	50
3.2.2	Fabrication process	54
3.2.3	Fluorescence tests	56
3.2.4	Pressure tests	57
3.3	Results	57
3.3.1	Fluorescence tests results	57
3.3.2	Pressure tests results	58
3.4	Conclusions	58
4	Parametric Numerical Study of Acoustophoretic Device	61
4.1	Rectangular cross-sectioned chamber	61
4.2	Numerical model, boundary conditions and convergence analysis	64
4.2.1	Numerical model	64
4.2.2	Boundary conditions	65
4.2.3	Mesh converge analysis	66
4.2.4	Particle tracing	66
4.3	Validation of 2D model	70
4.3.1	3D numerical model	71
4.3.2	Geometry and mesh	72
4.3.3	Comparison	72
4.4	Results	73
4.4.1	Constant channel width	74
4.4.2	Constant cross-sectional area	77
4.5	Conclusions	79
5	Acoustofluidics in inhomogeneous medium	81
5.1	Acoustic streaming suppression in inhomogeneous fluid	81
5.2	Sub-micrometer particles separation with fluid relocation	83
5.3	Shifting in acoustic resonance for different configurations	83
5.3.1	Inhomogeneous model	84
5.4	Pseudo 3D model	87
5.4.1	Idea behind the pseudo 3D model	89
5.4.2	Stabilized inhomogeneity	92
5.4.3	Fluid relocation	94
5.5	Continuous flow 3D model	95
5.6	Conclusions	97
6	Conclusions	99

A Acronyms	103
B Matlab Script for Pseudo 3D Model for inhomogeneous fluids	105
Bibliography	111

List of Tables

1.1	Advantages and Limitations of conventional techniques to separate Extracellular Vesicles. Adapted from [14]. DC: differential centrifugation, DGC: density gradient centrifugation, EV: extracellular vesicles, IC: immunocapture, Precip.: precipitation, SEC: size exclusion chromatography and UF: ultrafiltration. *The values come from studies that uses not only different isolation techniques but also different materials and methods thus values cannot be compared between the isolation approaches.	7
1.2	Summary of passive microfluidic technique for nanoparticles separation.	11
1.3	Summary of active microfluidic technique for nanoparticles separation.	19
1.4	General overview of exosome isolation methods. Advantages, disadvantages and main working principle are defined for each technique. The possible applications are identified for each method in the last four columns. Adapted from [64].	26
3.1	Properties of water at 25 °C.	49
4.1	Summary of the structure of the present study, where W is the width of the channel and S is the cross-sectional area of the channel defined as $W \times H$. Adapted from [112].	65
4.2	Properties for water at $T=25^{\circ}\text{C}$ and polystyrene. Adapted from [112].	67
4.3	Comparison of the fraction of particles collected in the central subdomain between the 2D and 3D model. Adapted from [112].	74
4.4	Summary of the height and the width for each aspect ratio value and the corresponding resonance frequency and wall displacement. Adapted from [112].	78
4.5	Summary of the height and the width for each aspect ratio value and the corresponding applied frequency. Adapted from [112].	79
5.1	Properties of blood cells from literature.	91

List of Figures

1.1	Schematic representation of exosomes genesis Multivesicular endosomes (Multivesicular Endosomes (MVEs)), which carry the exosomes, are formed in the intracellular space. They are released in extracellular space, after the fusion of MVEs with the cell membrane.[1].	4
1.2	Schematic representation of deterministic lateral displacement's phenomena. Two type of particles experience difference behaviours: the green one is moving following a "displacement mode", meanwhile the red one (smaller) is flowing with a zigzag mode, dependently on their centre of mass position respect to the fluid lamina. Adapted from [15].	10
1.3	(a) Schematic representation of a Field flow fractionation (FFF) device. the parabolic profile is shown and the vertical grey arrows represent the external applied field perpendicular to the flow. (b) Sketch of the common mechanism of separation: B component flows faster due to higher diffusion and its equilibrium position corresponds to higher velocity and thus collected earlier than A component. (c) A diagram that represents the collected fractions at the outlet of a FFF device. Adapted from [36].	13
1.4	Schematic representation of optophoresis principle. The sample contains micrometer particles ($\approx 1\mu\text{m}$, orange), submicrometer particles ($\approx 200\text{ nm}$, green) and the smallest nanometer particles ($\approx 50\text{nm}$, blue). For largest particles (orange), the scattering force is dominant, thus they are pushed away from the optical source. The green particles experience the optical gradient force which leads to a motion towards the optical source. The smallest particles (blue) are experiencing only the hydrodynamic force, so they follow the streamline. Adapted from [11].	14
1.5	On the top an example of polydimethylsiloxane electrophoresis device. On the bottom a schematic representation of the separation principle. The particles experience different electrophoretic forces as function of their properties when an electric field is applied. Adapted [43].	16
1.6	One cycle of harmonic wave traveling rightward.	20
1.7	Example of standing waves in a string. (a) The fundamental; (b) first harmonic; (c) second harmonic.	21

1.8	Schematic representation of free flow acoustophoresis (FFA) with a particle mixture [50]. As the acoustophoretic is size dependent, particles with same properties but different radius are moved differently toward the node (or the antinode). In this case for example bigger particles, which are focused faster can be easily collected in the central outlet. On the other hand, if the flow rates and the applied field are tuned correctly, it is possible to also isolate the yellow particles and the red ones in different outlets.	23
1.9	Sketch of binary acoustophoretic separation in a rectangular cross-section. Red blood cells which present a positive contrast factor are focused at the node of a standing acoustic wave. Lipids experience the opposite behaviour due to their negative contrast factor [61].	24
2.1	Sphere of radius a around which a fluid is flowing.	32
2.2	1-st order pressure field at mid-height of a rectangular cross-sectioned microchannel, 380 μm width, 160 μm height at an actuation frequency $f=1.9669$ MHz	36
2.3	Sketch of boundary-driven acoustic streaming in the rectangular cross-section of a channel of width W and height H . The magenta line represents the horizontal half-wave standing pressure field. Yellow lines represent the inner boundary layer streaming, Schlichting streaming. Black loops are the boundary-driven Rayleigh streaming rolls. Adapted from [83].	38
2.4	Sketch of the typical particle trajectories (red arrow) in a channel cross-section with a standing pressure half-wave acoustic field (orange line). A particle, with positive contrast factor ($\Phi_{ac} > 0$) and the size such that it can experience only acoustic radiation, is represented (blue circle).	40
2.5	Comparison of acoustic streaming between inhomogeneous fluid and the corresponding homogenized fluid. Adapted from [75].	41
2.6	Sketch of test function \hat{g}_n on the domain Ω	42
2.7	Sketch of the conservation in a discrete element \mathbf{C} of volume V_C	44
3.1	Sketch of the first geometrical layout of one filtering module. The distance from the wall to the posts is 52.5 μm , and the smaller gap between the posts is 2 μm . Reprinted from [107].	49
3.2	Residual of continuity, x-velocity, y-velocity and z-velocity for a maximum element size in bulk of 2 μm	50
3.3	Velocity contour plots obtained with (a)the first, (b) the second and (c) the third layout. Colourbars from blue (0 velocity) to red (highest magnitude). Reprinted from [107]	51
3.4	Mass flow rate through filtering modules for the first three layouts. Reprinted from [107].	52
3.5	Sketches of (a) fourth and (b) fifth layout. Reprinted from [107].	53

3.6	Velocity field contour plot in a filtering module of the fourth layout. Colourbars from blue (0 velocity) to red (highest magnitude). Reprinted from [107].	53
3.7	Velocity field contour plot in a filtering module of the fifth layout. Colourbars from blue (0 velocity) to red (highest magnitude). Reprinted from [107].	54
3.8	CAD drawing of the final layout for the microfluidic device. Dimensions are expressed in μm	55
3.9	Schematic representation of the fabrication process (1 to 7) and example of produced device.	56
3.10	Photograms obtained from fluorescence tests inside the COC filter with $4\ \mu\text{m}$ particles dispersion. (a) particles approaching the filter, (b) infusion after 3 min and (c) filtering modules after cleaning phase. Reprinted from [107].	58
4.1	3D sketch of a Bulk Acoustic Waves (BAW) microfluidic device.	62
4.3	Contours plot of the acoustic streaming velocity in $380\ \mu\text{m} \times 160\ \mu\text{m}$ (W×H) cross-section. (a) Particle trajectories with $5\ \mu\text{m}$ diameter. (b) Particle trajectories with $0.5\ \mu\text{m}$ diameter.	63
4.2	2D sketch of the considered fluidic control volume, where the lateral walls are actuated and the ceiling and bottom are considered as hard walls. The blue and grey arrows indicate a harmonic oscillation.	63
4.4	Mesh convergence analysis for different element sizes in the boundary domain. Reprinted from [112].	68
4.5	Schematic representation of the used rectangular cross section of the channel considered as reference system. The fluid domain was divided in 4 subdomains: 2 lateral bulk domains (lighter grey), 1 central bulk domain (darker grey) and a boundary domain close to the walls. A zoom of a squared zone defined with a red line is reported to show the mesh elements. Adapted from [112].	68
4.6	Fraction of the particles collected in the central subdomain as function of time for 0.42 aspect ratio (AR) and radius a of 250 nm. The number of particles used goes from 270 to 6756. Reprinted from [112].	70
4.7	Standard deviation of fraction of particles collected in the central subdomain. Reprinted from [112].	71
4.8	Full representation of the tetrahedral mesh used for the 3D model. Reprinted from [112].	73
4.9	Comparison of the first order pressure field between the 2D model (a) and 3D model (b). Second order velocity obtained with (c) 2D model and (d) 3D model. (e) 3D plot of p_1 . Reprinted from [112].	73

4.10	(a) Contour plots of acoustic streaming in different aspect ratio (0.42, 1, 1.2, 1.5 and 2 from left to right). (b) Acoustic energy density as function of the aspect ratio with an actuation frequency of 1.9669 MHz and a constant l_0 . Adapted from [112]	75
4.11	Fraction of particles collected in the central subdomain over time for particles with 250 nm radius. Adapted from [112]	76
4.12	Fraction of particles collected in the central subdomain as function of their radius. Reprinted from [112]	77
4.13	Fraction of particles collected in the central subdomain as function of their radius with a constant width of the channel. In this case the acoustic energy density was kept constant at 106 Pa and the walls displacement variable. (a) f was kept constant to 1.9669 MHz, the resonance frequency of the channel with 0.42 AR. (b) f was changed for each aspect ratio to the respective resonance value and the displacement was tuned to obtain the same E_{ac} for all AR. Reprinted from [112]	77
4.14	Fraction of particles collected in the central subdomain as function of their radius with a constant cross-sectional area. In this case the acoustic energy density was kept constant at 106 Pa and the walls displacement variable. (a) f was kept constant to 1.9669 MHz, the resonance frequency of the channel with 0.42 AR. (b) f was changed for each aspect ratio to the respective resonance value and the displacement was tuned to obtain the same E_{ac} for all AR. Reprinted from [112].	80
5.1	Sketch of the concentration profile with three inlet. The higher density fluid (dark blue) is an aqueous iodixanol solution. The lighter fluid is distilled water (light blue).	82
5.2	Acoustic streaming in a stabilized inhomogeneous fluid in stop flow at different time steps: 35 s (column 1), 55 s (column 2) and after total diffusion (column 3). Experimental particle positions (row a). Gray squares are spatial bins in experimental results (row b). Simulated acoustic streaming (row c). Reprinted from [75].	82
5.3	Properties Aqueous solution with iodixanol as function of concentration. Reprinted from [60].	85
5.4	Sketch of starting fluid streams for (a) stabilized and (b) relocation.	86
5.5	Acoustic energy density as function of frequency for different starting conditions.	86
5.6	Comparison of the "homogeneous" and "inhomogeneous" model for the acoustic streaming (left column) and the first order velocity field (right column). (a) It is sketched through line in the contour plots the reference location for the data. (b) Results for a chamber filled with water. (c) Results for a channel filled with 5% iodixanol.	88
5.7	Sketch of the transformation from a time-dependent problem to a space-dependent problem through the mean velocity $v_{p,i}(x, y, z)$	90

5.8	Contour plot of the velocity in the x direction $v_x(y, z)$ obtained with eq.5.8 for a flow rate of 500 $\mu\text{l}/\text{min}$	90
5.9	Properties of Ficoll Paque as function of the concentration.	92
5.10	(a) Sketch of the separation in stabilized configuration. (b) Three space frames of the concentration profile along the channel for an aqueous solution with 5% Ficoll Paque (inlet at the top and outlet at the bottom of the column). Colourbar from blue, lower density, to red, higher density.	93
5.11	Percentages of cells collected in the central outlet as function of the total applied flow rate at the inlet for a stabilized configuration.	93
5.12	(a) Sketch of the separation in fluid relocation configuration. (b) Three space frames of the concentration profile along the channel for an aqueous solution with 5% Ficoll Paque (inlet at the top and outlet at the bottom of the column). Colourbar from blue, lower density, to red, higher density.	94
5.13	Percentages of cells collected in the central outlet as function of the total applied flow rate at the inlet for a fluid relocation configuration.	95
5.14	Density profile in different slides along the channel with an aqueous solution of 10% Ficoll Paque injected in the central stream. Colourbar from blue, lower density, to red, higher density.	96
5.15	Density profile in different slides along the channel with an aqueous solution of 10% Ficoll Paque injected in the lateral streams. Colourbar from blue, lower density, to red, higher density.	97

Abstract

Early diagnosis has become one of the main tasks for modern medical research, in particular for genetic hereditary diseases and tumours. One of the most used approaches to perform a liquid biopsy is the blood test, in spite of two main limitations. Firstly, the knowledge about specific biomarkers is weak. The second limitation regards not just the type of biomarker, but also its concentration. Since a great amount of information about the body is carried inside the blood, an efficient blood analysis represents a powerful tool in healthcare strategy. Recently, attention turns to cell released vesicles called Extracellular Vesicles. Due to their role as carrier of information for intercellular communication Extracellular Vesicles represent a feasible way to support early diagnosis. Thus, their biogenesis, biostructure and efficient isolation have gained interest. One of the main expanding areas of research focuses on exosomes, which are lipid bilayer membrane vesicles released by almost every mammalian cell type.

Different laboratory protocols which exploit conventional techniques, such as ultracentrifugation, are widely used to separate exosomes/nanovesicles from biological fluids. However, despite their incredibly high efficiency, they are expensive, time consuming, technician dependent and they present low yield. Lab on a Chip technologies have emerged as alternative techniques to overcome these drawbacks.

Different microfluidic systems have been developed based on the most varied strategies for separating nanoparticles, such as acoustophoresis, dielectrophoresis, magnetophoresis, deterministic lateral displacement. This thesis presents the design and optimization of devices that can improve the separation of nanoparticles, e.g. exosomes, in a blood sample. There is heterogeneity in particles dimensions inside the blood, e.g. red blood cells, white blood cells, platelets and extracellular vesicles. Therefore, This thesis first focuses on a pre-cleaning stage, designing a "size-exclusion" device that separate bigger particles through a pillar structured filter. The trapezoidal shaped arrays were optimized using a numerical approach to obtain homogeneous mass flow rate over the filtering modules and low pressure drop along the channel. This led to developing a device that could efficiently stop particles bigger than $2 \mu\text{m}$. Subsequently a more pioneering technique, called acoustophoresis, was adopted with the aim of separating smaller particles. In this technique, ultrasound acoustic waves are used to generate a force for manipulation of particles inside a microfluidic channel. The main aim here was to increase the separation efficiency of the acoustophoretic systems and thus decrease the critical size of the particles, which is main limit of this technique. The first aspect that was attended to was the influence of the aspect ratio of the channel cross-section on the focusing efficiency of the particles. A 2D cross-section of a microfluidic channel was considered and validated with a 3D model implemented using the limiting velocity theory. The results show an increase in the focusing efficiency of the particles with higher aspect ratio of the channel cross-section, including sub-micrometer diameters.

Subsequently, the thesis investigates the effect of inhomogeneous fluid on the separation of sub-micrometer particles. "Stabilized concentration profile" was compared to an "acoustic fluid relocation". Both strategies were analysed using a finite element method numerical approach. The percentage of cells collected in the central outlet was computed using a pseudo 3D model with a plug flow assumption. A mixture of white blood cells and platelets was considered. Promising results were obtained for a stabilized concentration profile, showing an increasing separation efficiency with higher flow rates. On the other hand it was not possible to identify a trend for the fluid relocation approach, since the separation is strictly dependent on the switching position of the two fluids along the channel.

The insights gained from this thesis may be of assistance to further research about particles separation. In particular the novel microfluidic approaches presented in this study can pave the way to the development of diagnostic devices for Extracellular Vesicles isolation from a blood sample. Moreover, this work contributes to existing knowledge of acoustophoresis by providing a preliminary understanding about the influence of channel aspect ratio and of inhomogeneous fluid for particles separation.

Chapter 1

Introduction

A general background about exosomes and their separation is presented in this first chapter. The current common techniques used to obtain nanovesicles from a blood sample are introduced ([section 1.1](#)) in the first part of the chapter. Some of the disadvantages presented by conventional techniques are shown and possible alternative microfluidic techniques are illustrated at the end of this chapter ([section 1.2](#)).

1.1 Exosomes

Living cells usually release Extracellular Vesicles ([EVs](#)). These are classified as functions of their role in human body, size and cell of origin. In fact, the mechanism used by cells to exchange information is also through membrane vesicles that are secreted and present in low concentration in body fluids such as blood, saliva, breast milk and sperm [1]. The heterogeneous family of Extracellular Vesicles comprehends exosomes, ectosomes, microvesicles, microparticles, prostasomes, tolerosomes and nanovesicles [1]. They present a huge dispersity, ranging from microvesicles (≈ 100 - 1000 nm) [2] to exosomes (≈ 20 - 100 nm) [2, 3]. It has been found that [EVs](#) are involved in several pathological and physiological processes (i.e. inflammation, immune disorders, neurological diseases and cancer) [4]. For this reason interest in exosomes has grown significantly. They are nano-sized extracellular vesicles released for intercellular communication and the peculiarity is in their content, which depends directly on the cell of origin and it is unique [5]. A schematic representation of exosome biogenesis is shown in [Figure 1.1](#). At the beginning multivesicular endosomes [MVEs](#) are formed, then they carry the exosomes from the inside of the cell to the extracellular space [1]. Exosomes make an important contribution in several biological processes such as intercellular communication, immune function; development of stem cells, neuronal function; cell signalling, tissue regeneration, and vital replication [2, 5]. For example, exosomes play an important role also in the initiation, growth, progression and drug resistance of cancer [6]. Thus, exosomes have a clear strict link to their cells of origin. Due to this and also

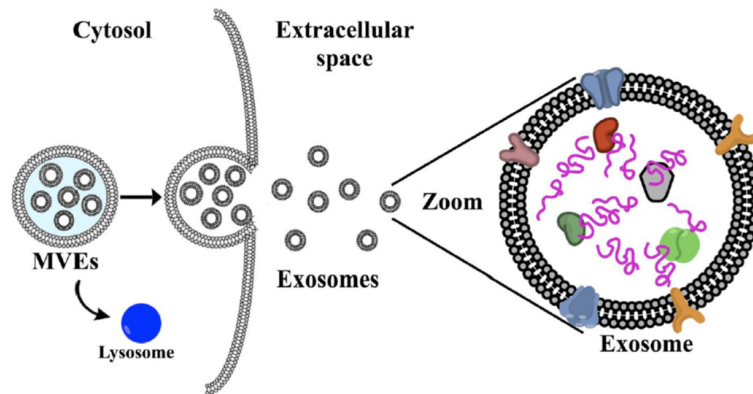


Figure 1.1: Schematic representation of exosomes genesis Multivesicular endosomes (MVEs), which carry the exosomes, are formed in the intracellular space. They are released in extracellular space, after the fusion of MVEs with the cell membrane.[1].

to the requirement of clinical biomarkers by minimally invasive techniques, exosomes have been found to play an important role in the research for treatments and diagnosis. The amount of exosomes released from cancer cells is higher compared to the amount produced by healthy cells. These promote the transformation of local healthy cells into unhealthy cells and contribute then to the formation of a favourable micro environment at future metastatic sites [7]. Exosomes are commonly isolated from human samples using different techniques such as filtration, polymeric precipitation isolation, liquid chromatography and the most used is ultracentrifugation [8]. A brief overview of the commonly used techniques is shown in the following sections.

- **Differential Centrifugation/Ultracentrifugation**

Differential centrifugation is the most applied and basic method for the separation of exosomes from human fluids. The isolation take place due to the difference in size and physical properties between the targeted particles and the rest of the sample. The protocol is composed by a sequence of centrifugation steps with different speeds. In each step, pellet (cells, dead cells and cell debris) and supernatant are separated and this last is then used for the next step [9]. Although this technique is simple and it has a high efficiency of purification, it is also time-consuming, labor-intensive, instrument-dependent and it requires a big amount of serum samples [8, 10]. Furthermore, due to the high gravity force, there is a high tendency for the particles to aggregate and sometimes to break [11].

- **Density Gradient Centrifugation**

In this technique an inert gradient medium is needed. The method is based on the sinking of components in the sample due to their different isodensity zone during a centrifugation. A molecule that is commonly used in the medium to increase the density is the sucrose. The density gradient centrifugation could be thought as

alternative to the traditional ultracentrifugation with a resulted exosomes sample with higher purity. The strong density gradient prevent the mixing, the rupture and deformation of the exosomes which is one of the main advantages. On the other hand, this method is time-consuming (a long process is needed to prepare the gradient medium) and the throughput is not high. Other shortcomings are the high costs of the instruments required for the density gradient centrifugation and the need of space in the laboratory for locating these machineries [12].

- **Extraction Using Immunomagnetic Beads**

This method is based on spherical magnetic particles coated with monoclonal antibody specific to a certain marker expressed by the target exosome. Particles with these properties are called immunomagnetic beads. First, a sample in which the beads are linked to the exosomes with the associated receptor molecule has to be prepared then, if a magnetic field is applied, the forced movement of these complexes allows the separation of the desired exosomes population. Although this method is quite simple to carry out and it is very target specific and keep the integrity of the collected exosomes, one of the main disadvantage lies in the bound between the beads and the target vesicles. In fact it is not simple to unbound by elution, thus the complexes cannot be used for all the downstream experiments [8, 13]. Moreover, this technique, due to the high selectivity, let to separate a specific subpopulation which expresses the target biomolecule. This could represent a advantage when the antigen-antibody is known, on the other hand could be a disadvantage since all the desired subpopulation is at the end of the analysis a complex with the beads, thus unusable.

- **Extraction Using Exoquick_{TM}: Exosome Precipitation Reagent**

Exoquick_{TM} is a commercial exosome precipitation reagent, used for the compound polymerization precipitation. Mixing the sample with the Exoquick_{TM} reagent, a mesh-like polymeric grid is formed which captures the exosomes in a range of size that commonly goes from 60 to 180 nm. These are extracted as pellets with a centrifuge working at low speed. This technique has the advantages to be fast and simple and yet it needs just a basic centrifuge [8]. Even though it does not need great amount of sample, this technique present three big disadvantages. The former one is that some contaminant molecules should be extracted with the exosomes. One other disadvantage is that only exosomes with a certain diameter could be extracted, thus the technique is not feasible for larger exosomes.

- **Chromatography**

Also called as Size-exclusion chromatography (SEC) is based on the different movement of particles in samples through a commercial filtration column [5]. Macromolecules that have a dimension greater than the pore size cannot pass, meanwhile smaller molecules could enter in the gel pores and be retained in the

column. This permits an high purity throughput, although the volume extracted is very low and the laboratory equipment is extensive [8].

Due to the several limitations of the methods presented above, many novel techniques for the separation of exosomes, which do not involve the use of microfluidic, have been recently developed. Some of these are reported below.

- **Stirred Ultrafiltration**

The pore size of an ultrafiltration membrane can intercept or allow the passage of substances as function of their relative molecular mass. The advantage of stirred ultrafiltration is that it is less time consuming, and it does not need an ultracentrifuge. Moreover, the number of exosomes per sample volume is very high, and yet compared to the ultracentrifugation this method requires lower pressure, thus the integrity of the exosomes is better guaranteed. However, due to the size based principle the purity of the sample is not so high for the presence of compounds or molecules with the same dimension of the extracted exosomes, such as microbubbles and apoptotic bodies [8].

- **Nanoplasmon-Enhanced Scattering (nPES)**

The principles behind this techniques are very similar to the Enzyme-linked Immunosorbent Assay (ELISA). Antibodies against cellular markers usually present on exosome membrane are used to selectively capture and detect them. The procedure begins with a sensor chip which is prepared for sample application. This means that a specific antibody is linked to the silica surface, thus all the exosomes that express the precise marker can be trapped when the sample is loaded. After that, Antibody-coated Gold Nanoparticles probes (GNPs) are inserted in the system so these can be linked to captured exosomes forming GNPs-exosomes complexes. In this way the target exosomes can be separated from the sample and detected through dark-field microscopy. This method is rapid, high-throughput, sensitive and specific but it is also expensive and complex due to the statistical tools needed to detect the amount of radiation.

In conclusion, conventional techniques used to separate nanoparticles present several limitations. The time requirement of some approaches, as chromatography and electrophoresis, is very high. A large volume of sample for separation is commonly required. Furthermore, some traditional ways (i.e. selective precipitation and ultracentrifugation) lead to sample loss, or aggregation, when a sieving separation techniques is used. The finally draw back, is the high expensive equipment dependency of these technique. The advantages and limitations in terms of volumes, recovery, contaminant and clinical applicability are reported in 1.1.

	DC	DGC	SEC	UF	IC	Precip.
Isolation						
Major Contaminant	Similar-sized particles	Lipoproteins	Same size particles	Same size particles	Soluble proteins	Protein
Major artifact	EV-particle aggregates			EV-particle aggregates		Protein complex, EV-particle aggregate
EVs/ μ g protein increase(fold)*	1-15	1-20	70-560	1-10	1-50	1-3
Concentration						
Volume reduction (fold)*	0.2-8	\approx 1	0.2	<240	5	\approx 50
EVs recovery,%*	2-80	10	40-90	10-80		90
Practical						
Assay time,h	3-9	16-90	0.3	0.5	4-20	0.3-12
Sample volume	mL-L	μ L-mL	μ L-mL		μ L-mL	μ L-mL
Clinical applicability	No	No	Yes	No	Yes	Yes

Table 1.1: Advantages and Limitations of conventional techniques to separate Extracellular Vesicles. Adapted from [14].

DC: differential centrifugation, DGC: density gradient centrifugation, EV: extracellular vesicles, IC: immunocapture, Precip.: precipitation, SEC: size exclusion chromatography and UF: ultrafiltration.

*The values come from studies that uses not only different isolation techniques but also different materials and methods thus values cannot be compared between the isolation approaches.

1.2 Separation of nanoparticles with microfluidics

The exosomes (and more in general biovesicles) present a high dispersity and huge differences in properties as function of their content. Moreover, there is a lack in the actual literature about the mechanical properties of these nano-sized particles. It is for this reason that commonly the devices are firstly optimized for the separation of synthetic nanoparticles and further tested with biological samples. Thus, finding a good way to separate nanoparticles has aroused interest, in order to avoid or limit the drawbacks of the methods expressed above (the discontinuity in process, multiple steps of preparation and large sample volumes). Microfluidic technique has offered a simpler, low-cost and continuous alternative. On the other hand, although microfluidics has been well-established and widely applied as micro-particles separation technique, it is now facing several difficulties with the conversion to a nanoscale separation. Generally speaking, microfluidic techniques can be classified as active and passive. Passive separation only relies on specific properties of the microfluidic device, such as geometry, hydrodynamics or surface characteristics, meanwhile the active separation needs an external applied field to achieve the displacement of the particles. The main approaches for both passive and active separation will be described below and summarize in Tables 1.2 and 1.3 respectively. Usually to sort particles with active separation, external forces

are necessary to generate a displacement from the initial position. These forces (present for example in dielectrophoresis, acoustophoresis) are strictly dependent on the size of the particle. Due to this effect (for a more detailed explanation see [section 2.2](#)), simply increasing magnitude and frequency could not achieve a higher efficiency. In addition, when the particle size decreases, Brownian motion becomes important, and it could lead to a decrease in separation. Thus, the separation of nanometric entities in microfluidic devices is a challenging point that has gained interest in the scientific community. As mentioned above, instead of using an external field, many studies investigate the use of microstructures in the channel, pores, pillars or membranes to selectively separate particles as function of their size. The main drawback of this approach lies on the usage of sophisticated technologies needed to fabricate and characterize these structures at the nanoscale [11]. One more point that has to be taken in account is the high surface to volume ratio of nanometric particles. This is directly linked to an higher surface energy and thus to possible aggregation and sticking to the walls of the device. This highlights the importance of surface treatments, of the right choice of the buffer solution, and the surfactant for limiting the aggregation during the separation process. In addition, compared to the conventional methods, the throughput of microfluidic separation techniques is still a challenge for industrial scale-up, when high volumes of samples come into play. One of the most common solutions is to stack the microfluidic devices in parallel, but it might not be enough or achievable for all the cases. Both active and passive separation techniques present different advantages and limitations. As briefly described above, the active separation technique uses various forms of external fields. The force generated lead to the manipulation and separation of particles with slightly high performances compared to passive techniques. On the other hand, these last approaches have simpler structures and do not need an external field. In spite of this, the size of the device is relatively large, due to the strict dependency on channel geometry and structures. Moreover, passive approaches use low flow rate leading to a higher time consuming separation [15].

1.2.1 Passive Separation

- **Membrane-based filtration**

This method is based on the usage of a microfluidic device, which is built following the same principles of a size-exclusion chromatography. Two membranes with different pore sizes are placed in series. Particles that are larger than the first filter can not enter the sample chamber, and similarly particles lower than the second pore size flow in the waste chamber and at the end the filtered sample, which have entities with dimensions between these two outer boundaries, can be collected in the sample chamber. The flow can be driven by pressure [12] or by electrophoretic migration . The efficiency of enrichment of the exosomes is much higher than ultracentrifugation. Moreover, this technique, since it uses

a size exclusion principle, does not require any usage of antibody neither of expensive equipment. The main disadvantage in using this kind of systems is the presence of high pressure at the membrane that could lead to the rupture of the vesicles, and thus influence the purity. In addition the integrated double filtration microfluidic device has the same lack in purity as in ultracentrifugation and ultra-filtration methods [8, 16, 17]. Recently a lab-on-chip device, called Exosome Total Isolation Chip (ExoTIC), was developed by Liu and co-workers [18]. The device works based on the simple principle of filtration using nanoporous membranes that can enrich and purify exosomes between 30-200 nm in size. The working protocol of the device is the following. First, the sample is introduced through a syringe pump into the system. After that, the device is rotated by 180°, thus the proteins and free nucleic acids are free to flow out from the outlet and the exosomes are collected on the filtration membrane. It represents a simple, fast, cost-effective, and scalable method. Furthermore, because this protocol achieves a high-yield of extracted exosomes even from small samples, it can be used for point-of-care testing and several other applications and studies [18].

- **Inertial microfluidics**

This is a passive separation based on the geometry of the device. Nowadays different inertial microfluidic systems have been developed for the separation of particles such as straight microchannels, spiral microchannel, serpentine geometry and expansion contraction array [11]. The Brownian motion is predominant when small particles are considered, and it makes the separation challenging at the nanoscale. Inside a straight microchannel the balance of lift forces let the separation happen, while in a spiral chip the centrifuge force has an important role too. When a fluid flows around the surface of a suspended object, a force is generated and its perpendicular component respect to the flow direction is the lift force. Both when a straight or a spiral channel are considered, the net lift force (\mathbf{F}_L) experienced by a particle is the sum of a shear-induced inertial lift force (\mathbf{F}_{IL}) and the wall-induced inertial lift force (\mathbf{F}_{WL}). Former one is a fluid flow dependent force. In fact, in a Poiseuille parabolic velocity profile results in a shear-induced lift force experienced by the particles, which are pushed away from the channel centre. As the particles approach the walls the wall-induced inertial lift force become dominant and move the particles away. The balance between these two oppositely directed forces defines the equilibrium position. The spiral microchannel showed a high efficiency of separation. In more detail, if high flow rates are imposed in a spiral device, even if the laminar flow condition is still valid, a two-vortex shaped secondary flow is established. Small particles can experience these vortexes, meanwhile larger one are pushed forward the wall by the centrifugal force. The magnitude of this phenomena can be described through an adimensional number called Dean Number (De) [19, 20]. Lee et al. [20] used this method to separate efficiently nanoparticles with 150 nm of diameter, from 1 μm

particles.

- **Deterministic Lateral Displacement (DLD)**

Deterministic lateral displacement **DLD** is a technique which utilises a predefined pattern of pillar to precisely generate a unique flow streamlines, that allows the separation of particles. In the last years, this kind of microfluidic technique has been widely investigated for the separation of circulating tumour cells [21], spores [22], blood cells [23], mammalian cells [24], bacteria [25]. The principle behind this technology is to use a particular arrangement of pillar for controlling the displacement/trajectory that the particle could have as function of its diameter [26, 27]. In other words, deterministic lateral displacement does not work on diffusion, thus particles with higher or smaller size follow different, predefined paths determined by the array of pillars. There is a cut-off diameter between two different possible behaviours, as shown in Fig.1.2. The former one is for particles

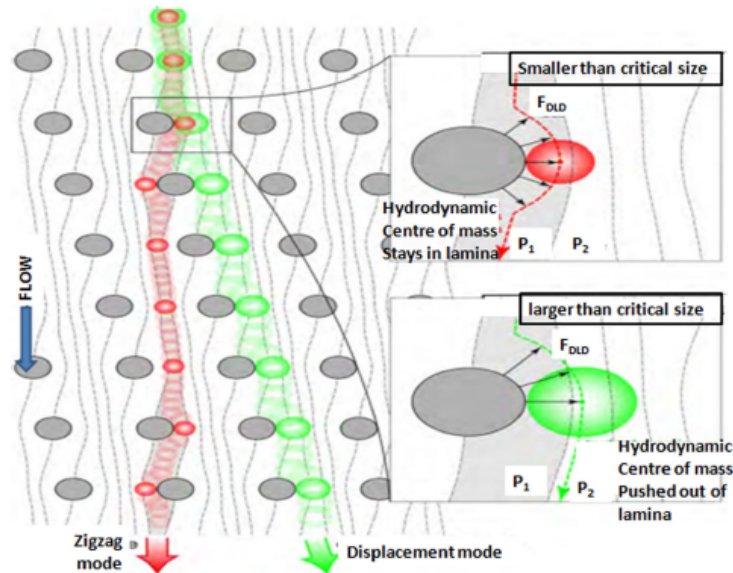


Figure 1.2: Schematic representation of deterministic lateral displacement's phenomena. Two type of particles experience difference behaviours: the green one is moving following a "displacement mode", meanwhile the red one (smaller) is flowing with a zigzag mode, dependently on their centre of mass position respect to the fluid lamina. Adapted from [15].

larger than the width of the fluid streamline attached to the post. These will be forced to follow the streaming far from the posts. They will be bumped deterministically at each subsequent row following the so called "bump mode". On the other hand, if the particles are smaller than the width of the fluid streamline closer to the pillar, they will perform a "zigzag" pattern, near to the posts and

following the streaming [28]. If one has to separate particles at the nanoscale, this critical value will obviously decrease and a smaller gap or row shift fraction is needed and yet diffusion phenomena becomes predominant when the diameter of particles is small. These particular adjustments lead to a less efficient device. A small gap, between two pillars, increases the hydrodynamic resistance, thus higher pressure is required, and the fabrication becomes harder too. On the other hand, a small row shift fraction, lower respect to the common values, lead to a longer separation region and higher probability of diffusion. Although these problems are important and the presence of pillars promote clogging and the throughput decrease fast over time. Moreover, this technique is simple and widely studied and used for micro/nanoparticles separation [11].

Technique	Phenomena	Advantage	Disadvantage
Membrane based filtration	Sieving	Simple technique and high separation efficiency	High chance of membrane clogging and medium-low throughput
Inertial microfluidics	Dean vortices	Very high separation efficiency, simple fabrication and high throughput	Efficiency affected by particle-particle interactions
DLD	Specific patterned pillars	Simple and efficient technique	Low throughput, not simple to fabrication, high possibility of clogging.

Table 1.2: Summary of passive microfluidic technique for nanoparticles separation.

1.2.2 Size-exclusion devices for nanoparticles separation - An example of passive microfluidic technique

Since the first approach used in this work involved developing a passive system which could separate micrometer sized particles from a blood sample, in this section an overview of size-based separation device is presented. These systems usually involve the use of nanofilters, nanoporous membranes or nanoarrays, which could be fabricated for covering the section of the microchannel or set on a inner surface of this. Desired particles could be trapped (or could flow) through the structures while a flowrate or a pressure drop is applied. This kind of technique is widely used for nanoparticles separation, particularly for exosomes. One of the most pioneering studies is Wang et al. [29] which

consist in the fabrication of nanowire-on-micropillar structures for trapping exosome-like lipid vesicles. One of the most known examples of size-based separation technology, as explained in the previous paragraph, is deterministic lateral displacement since the physics behind filtration phenomena is size-dependent (illustrated in Fig. 1.2). a highly innovative device which used this strategy was studied by Huang et al. [27]. They presented a hydrodynamic based microfluidic system which separated micro and nano particles depending on their sizes. They imposed a laminar flow and through the use of periodic array of squared micrometer scaled obstacles they obtain a different migration path for each size was obtained. Another example of device that used deterministic lateral displacement was presented by Santana et al. [30]. They implemented a microfluidic technology that separates microvesicles, as a function of diameter, from a cancer-cell-derived extracellular vesicles population. This system was designed to control particle trajectories using microfluidic obstacle arrays. A ground breaking technique was developed by IBM research team [31], where silicon processes were used to produce nanoscale deterministic lateral displacement arrays. They demonstrated that for low Péclet number (Pe), particles in the range of few hundreds nm can be separated (for a more detailed explanation of the Péclet number, see section 2.1). Another sized-based technique is nanofiltration. In this case the process is very simple. A membrane allows particles smaller than cut-off sizes to flow. In this case the processes and materials for the membranes represents the bottleneck. Over the years several possible solutions were investigated. One example is the Lab-on-a-Chip developed by Kim et al. [32]. A commercial membrane was included within microfluidic channels in order to separate cells from whole blood. Moorthy et al. [33] developed a polymer-based membrane using emulsion photo-polymerization. This porous filter embedded inside a microfluidic channel was used to separate blood cells from serum. Crowley et al. [34] instead demonstrated the use of a passive transverse-flow microfilter device for the separation of plasma from whole blood and the device presented works entirely via capillary action.

1.2.3 Active Separation

- **Field-Flow Fractionation FFF**

It is a technique based on the coupling of hydrodynamic forces, Brownian motion and external force field. The transversal applied field leads the particles motion towards the side walls of the device [11]. The working principle is based on the retention time of the particles that comes from the balance between diffusion movement and the forces generated by the external applied field. In other words, the separation mechanism relies on differences in particle mobility under the forces of the field, in equilibrium with the diffusion transport phenomena. At this point, the parabolic laminar-flow-velocity profile in the channels determines the velocity of the single particle, based on its position from the walls. Since every

particles depending on size/mass will have different travelling speed, the separation occurs [35], as shown in Fig. Figure 1.3. The type of the applied field can differ based on the particles properties used for the separation, i.e. electric field, magnetic field or thermal gradient. This technique presents a high throughput and separation efficiency. However, parameters such as field magnitude, sample types, solvent type, have to be optimize to improve the separation[11].

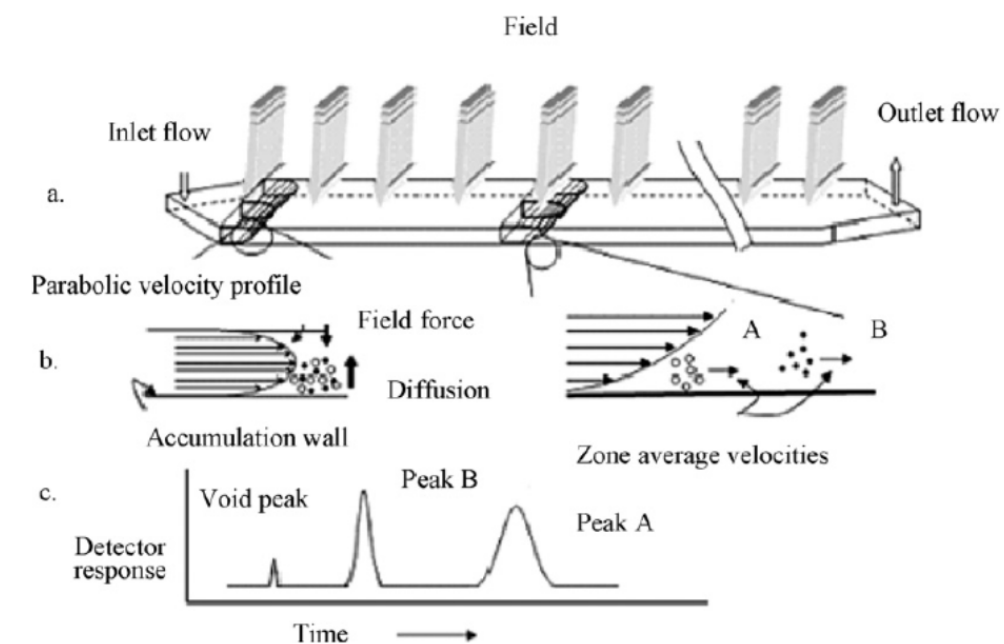


Figure 1.3: (a) Schematic representation of a FFF device. the parabolic profile is shown and the vertical grey arrows represent the external applied field perpendicular to the flow. (b) Sketch of the common mechanism of separation: B component flows faster due to higher diffusion and its equilibrium position corresponds to higher velocity and thus collected earlier than A component. (c) A diagram that represents the collected fractions at the outlet of a FFF device. Adapted from [36].

- **Centrifugal microfluidics**

Usually to overcome the Rayleigh-Taylor hydrodynamic instability in conventional centrifugation, a density gradient is needed, as reported in the previous section. This represent a big disadvantage since a long preparation and the right choice of the chemical are necessary to achieve the right density gradient. A microfluidic device was developed by Arosio et al.[37]. It works as density-free centrifuge and it is not based on surface interactions compared to other techniques. One point of strength of using microfluidic instead of a conventional system is the shorter time to sort nanoparticles without sample dilution. The working principle of centrifugal microfluidic is the difference in displacement due to centrifugal

forces based on particle sizes and densities. Since a centrifugation equipment is needed it makes this technique not common for particles separation. Moreover, it is a discontinuous method, thus it is losing one of the main advantage of microfluidic.

- **Optophoresis**

The first approach to optical manipulation was done by Ashkin in 1970. An optical system was developed for trapping and moving individual particles inducing an optical force as function of their size, shape and optical properties [38]. Nowadays the separation occurs with an optical force perpendicular to the flow which moves the particles in different positions of the microchannel. Three main forces are present in optofluidics: the drag force, the optical scattering force and the optical gradient force. In these systems nanoparticles are affected only by the drag force, meanwhile larger particles displacement is affected both by Stokes force and optical forces, as shown in Fig. Figure 1.4. This techniques presents high separation efficiency and throughput. Although, overheating or photodamage in the sample do to optical source represents one of the main drawback [11].

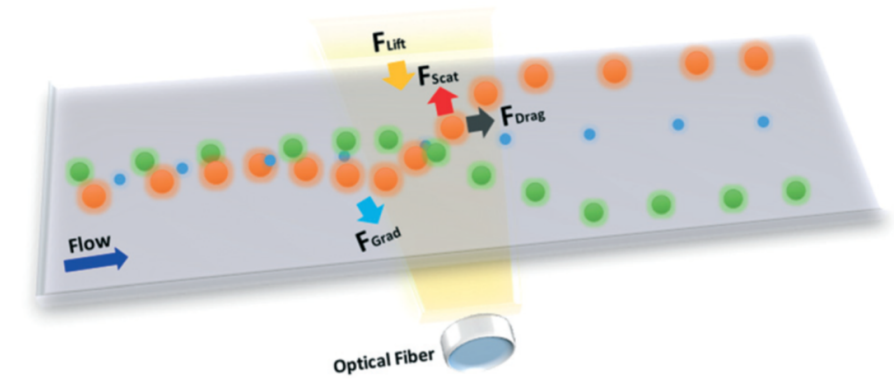


Figure 1.4: Schematic representation of optophoresis principle. The sample contains micrometer particles ($\approx 1\mu\text{m}$, orange), submicrometer particles ($\approx 200\text{ nm}$, green) and the smallest nanometer particles ($\approx 50\text{nm}$, blue). For largest particles (orange), the scattering force is dominant, thus they are pushed away from the optical source. The green particles experience the optical gradient force which leads to a motion towards the optical source. The smallest particles (blue) are experiencing only the hydrodynamic force, so they follow the streamline. Adapted from [11].

- **Magnetophoresis**

Depending on the source of the magnetic field two kind of magnetophoretic devices can be developed. One use electromagnetic strips integrated in the microchannel during the fabrication process. The other one is based on the actuation of an external magnetic field. As function of magnetic susceptibility difference between the particles and the fluid it is possible to have a positive or a negative magnetophoresis. In the positive magnetophoresis the particles are moved toward the greater magnetic field. If the magnetophoresis is negative particles migrate away from the magnetic source. Polymeric materials can be used to produce these kind of systems. This technique presents several advantages: the device is simple to fabricate, magnetophoresis does not require large sample elution and it presents high throughput. When the separation involves paramagnetic particles, they can be simply moved by the magnetic field. For diamagnetic particles a prior conjugation with paramagnetic antibody-conjugated nano-beads. The long procedure to label with antibody the magnetic beads represents one of the main drawback of this technique [11].

- **Affinity-based sorting**

This technique is characterized by the affinity between the target particles and a specific surface, structure or material, which let to separate bound particles from unbound ones. This method is self-standing or can be integrated with other active separation technique, such as magnetophoresis. The affinity-based sorting has the same working principle of chromatography, by selectively binding the target to the stationary surface while the sample is flowing through the chip. Mainly affinity-based sorting is used for the separation of biomolecules or biovesicles since they present a target molecule on their membrane that is used to create the bound with the functionalized surface. For example, the affinity-based sorting was used for trapping circulating extracellular vesicles [39]. Two type of approaches are reported in literature: A device that uses a functionalized inner surface(s), where the interaction takes place or systems that use capture beads. However, in many cases the protocol expects a sample mixing and incubating to achieve complexes formation. The separation, washing and analysis is done downstream on-chip [5]. Although the antibody, or aptamer, binding has a high specificity, the procedure is expensive and it is very hard to prepare the surface in the right way. The non-specific surface adsorption represent a cheaper but less efficient way to perform affinity-based sorting. For example, new investigations demonstrate the use of electrostatic interactions or hydrophobicity [40, 41].

- **Electrophoresis**

Since the equipment is very simple and the forces are easily controlled, electrophoresis is one of the most common used microfluidic technique for the separation of nanoparticles. While particles suspended in the medium are experiencing the drag force, three other forces, generated by the applied electric field, play a fundamental role in the separation: electrophoretic, electroosmotic and

dielectrophoretic (when the electric field is not uniform). Electrophoresis is referring to the movement of charged particles in the presence of an electric field. This motion depends on the particles electrophoretic mobility. This last factor is dependent by the zeta potential of the particles and the physical properties of the fluid. This force is at the base of the charged-based separations. An interesting example of the electrophoresis application in microchannel is the so called miniaturizing free-flow electrophoresis (μ FFE). This technique couples a pressure-driven system with a transversal electric field to achieve a continuous separation [42]. A deep understanding of the phenomena and the forces that take place in this systems is presented in the study of Jeon et al. [43]. Their study was focused on the development and analysis of a pressure-driven flow induced miniaturizing free-flow electrophoretic device (Figure 1.5). It has a common T-junction structure, with one inlet for the sample and two outlets. In their paper the importance of comparing the effects of electroosmosis and electrophoresis to analyse the particle displacement is underlined. The separation is possible when

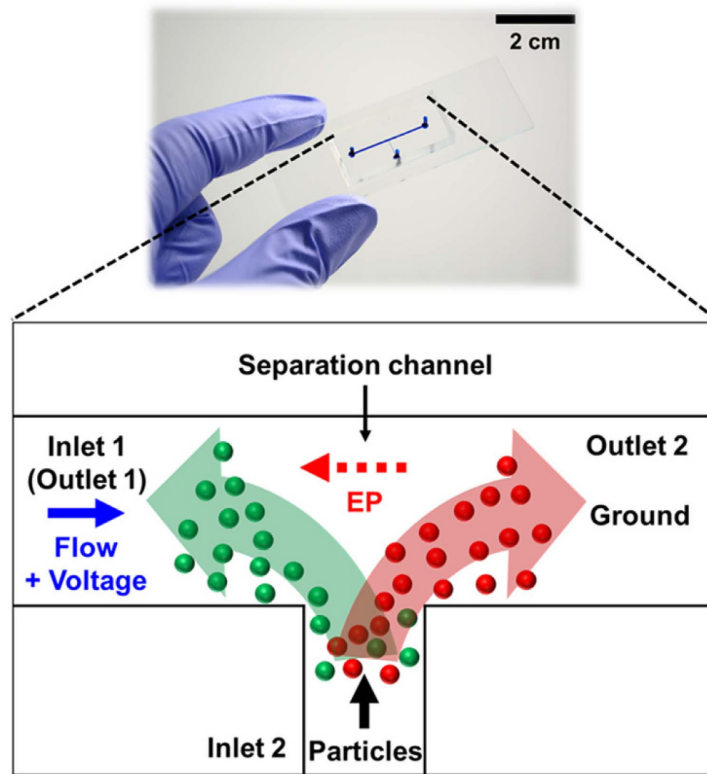


Figure 1.5: On the top an example of polydimethylsiloxane electrophoresis device. On the bottom a schematic representation of the separation principle. The particles experience different electrophoretic forces as function of their properties when an electric field is applied. Adapted [43].

the electroosmotic mobility of the microchannel is lower than the electrophoretic mobility of the particles. When this request is not achieved the electroosmotic force acts opposite than the electrophoretic force, which lead to a hard separation capability. In this perspective is important to choose correctly the material of the device. Recently different materials have been used for electrophoretic microfluidic devices. Nowadays it is possible to produce the whole device using 3D printing approach, as the one proposed by Barbaresco et al. [44]. When a non-uniform electric field is applied to induce a force acting on the particles, the technique is called (Dielectrophoresis (DEP)) Dielectrophoresis. The force has magnitude and direction as function of the gradient of the electric field and particle's electric dipole. It is called positive DEP when ratio between electric permittivity of the particle and the suspending medium is lower than one. This implies a displacement of the particles toward the higher electric region. When this ratio is higher than one it is called negative DEP and the particles will move towards a low electric field region. It was numerically proved the possibility of use a continuous dielectrophoretic separation of 30 nm from 60 nm gold nanoparticles [45]. Another way to achieve an electrophoretic separation is the Ion concentration polarization (ICP), technique based on the usage of Nafion™injunction under an applied electric field. The cations transported by Nafion™cause a ion-depletion zone on the anodic side and a cationic enriched side. This phenomena lead to an amplified electrophoretic force that deflects the particles from the flow streamlines as function of their electrophoretic mobility [11].

- **Electrohydrodynamic vortices** When a microscaled channel is considered, the laminar flow condition is commonly respected (Reynolds number (Re) < 1 , a more detailed explanation of the Reynolds number in section [section 2.1](#)). If parallel microelectrodes strips are placed in a transverse direction respect to the flow, a travelling wave can disrupt the flow and induce vortices. These induced eddies can be used for trapping nanoparticles. One of the main study about the separation of nanoparticles using this technique came from Green et al. [46]. The aim of this study was to separate 93 nm and 216 nm diameter latex particles. Although this approach can present a very high efficiency, it has a very low throughput (2 μ L/h) and the fabrication process is complex[11].
- **Acoustophoresis** When an acoustic field is applied, and particles are moved due to their different properties (e.g. density and compressibility) compared to the suspending medium the phenomena is called acoustophoresis. During the years different studies were performed in order to improve the efficiency of these technology and understanding the physics behind. Two kind of systems have been classified in literature called **BAW** devices and Surface Acoustic Waves (**SAW**) devices. The difference between these is about the type of acoustic wave that is propagated inside the systems, as the names underline. Bulk acoustic wave devices use a standing wave created inside a fluid volume in a confined chamber.

This is possible when the ultrasound wavelength matches the geometric dimension of the microchannel. The limiting part of this technique is the necessity of hard material for the chip since the wave must be completely reflected in the chamber. This leads to harder fabrication processes respect to the use of softer material such as polymers. For example, glass and silicon have very good properties for standing wave, since it presents a large density different compared to aqueous fluids, it is chemically inert and it has a quite high speed of sound [47]. Meanwhile, surface acoustic waves devices do not require acoustic reflection properties of the materials, since the wave is propagated and generated through interdigitated transducers, coated on a piezoelectric material. The shape of the wave is then defined by the design and the location of the interdigitated transducers. There are still limitations of acoustophoretic-based blood component separation systems. For example, the throughput is very low ($\mu\text{L}/\text{min}$ is the common range). Moreover, acoustofluidic separation is mainly studied for manipulate microscaled particles such as cells, platelets and bacteria. It remains challenging to manipulate sub-micron entities in blood including proteins, vesicles, aggregates, virus or biomolecules.

1.2.4 Acoustophoresis in BAW devices for particle manipulation - An example of active microfluidic technique

Generally speaking, a wave is generated when a vibration is propagated through the neighbouring area, which starts to vibrate, causing in turn another neighbouring environment to begin to vibrate and so on. In acoustics, waves are described by a pressure oscillation in the medium (solid or fluid) caused by the wave. This happens because when a wave passes through any medium, the distance between molecules (or atoms) changes periodically. Now consider the medium as a string with one fixed end. A pulse can be sent through the free end down the length of the string. The motion of the particles in the string is directed perpendicularly to the pulse direction. A transverse wave traveling down the length of the string can be seen. If the disturbance is harmonic it can be represented mathematically by a combination of sine and/or cosine. Consider a wave traveling along the x direction with a particle displacement along the y -direction, as expressed in Fig. 1.6. A wave can generally be described by the equation

$$y(x) = A \sin(kx + \phi), \quad (1.1)$$

where A is the amplitude (in this case the maximum displacement of the string) in the y -direction, k represents the wave number and ϕ the phase. As the disturbance moves to the right there is a shift in the position $\Delta x = x_f - x_0$ in a time range Δt , thus with a wave velocity $c = \frac{\Delta x}{\Delta t}$. A traveling wave, then, has to be expressed as function of space and time. A more general equation for a traveling wave is

$$y(x, t) = A \sin[k(x - ct) + \phi]. \quad (1.2)$$

Technique	Phenomena	Advantage	Disadvantage
FFF	Applied external field and asymmetrical flow	High throughput and high separation efficiency	Specific sample, solvent or membrane are needed
Centrifugal microfluidic	Centrifugal and hydrodynamic drag force	High throughput, no density gradient and dilution	Need a centrifugation equipment, discontinuous
Optophoresis	Optical scattering force, Optical gradient force and Stokes force	High throughput and separation efficiency	Overheating and photodamage of the sample
Magnetophoresis	Magnetic susceptibility properties of particles and fluid	High throughput, very low cost	Long antibody labelling process
Affinity based sorting	Specific/non-specific surface interaction	High efficiency and specificity	Expensive antibody, tricky and multiple preparation steps
μ FEE	Applied uniform electric field	High efficiency and resolution	Flow rate change with chemistry and channel material
DEP	Applied non-uniform electric field	High efficiency and throughput	High voltage and dependence on medium conductivity
ICP	Electric field and Nafion	Low voltage, external electrodes	Cannot separate very small particles and low throughput
Electrohydrodynamic vortices	Travelling waves, local thermal convection	High efficiency	Complex electrodes fabrication and low throughput
Acoustophoresis	Acoustic field	High separation efficiency, controlled size separation	Complex fabrication, limits on the materials for the device (for BAW devices)

Table 1.3: Summary of active microfluidic technique for nanoparticles separation.

This equation can be applied for all kinds of mediums. The profile of the wave defined above presents points which are repeated at constant phase. The rate (number of times per second) at which a point of constant phase passes a point in space is defined as frequency. The speed of the wave can be described by the product of the frequency and the wavelength λ (the distance over which the wave shape repeats). One of the more efficient way to understand what a standing wave is, it is through the definition of interference. This is a physical phenomenon generated by two (or more) waves added

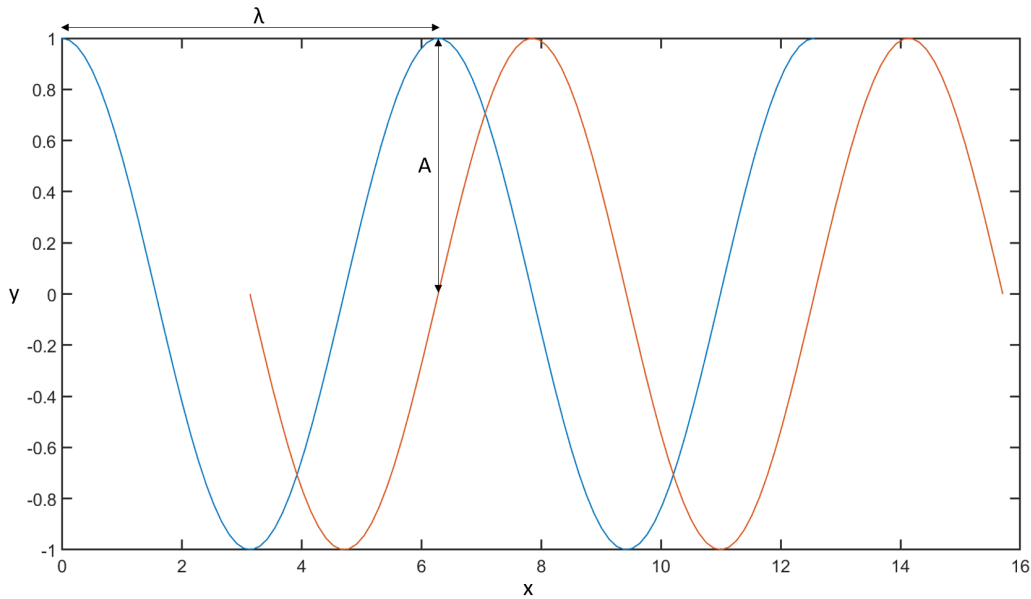


Figure 1.6: One cycle of harmonic wave traveling rightward.

together. If for example two identical traveling waves which move along a string from left to right towards a boundary fixed end and the wave, generated by the first pulse, hits the end, it reflects and change its direction of propagation leftward. When it meets the wave generated by the second pulse along the way, the two waves add together linearly. The displacement (or amplitude of the wave) where the two waves meet each other in space is greater than (or smaller than) the amplitude of the single wave. If the resulting wave has an amplitude lower than the generating waves, the interference between them is called destructive. In the opposite case, if the resulting wave has a higher amplitude, then the two waves are said to have constructively interfered with each other. If the disturbance caused is harmonic, a periodic wave is moved along the string and meet the returning periodic traveling wave, i.e. they interfere. This means that the resulting amplitude is the sum of the amplitudes of each wave, everywhere and at any time. If the returning wave is inverted and the length of the string is tuned to be a multiple of the half-wavelength (derived from the frequency of the harmonic disturbance), the system meets the resonance conditions [48]. The resulting wave is called standing wave. The points in space where the standing wave has its maximum are called antinodes. The points of zero displacement are called nodes (these terms will be discussed in more detail in the subsequent chapters). An example of some harmonics of a standing wave are reported in Fig. 1.7. With regard to acoustics, the wave is described by a pressure wave. Thus, a standing acoustic wave is an harmonic oscillation of compression and rarefaction zones. Sound waves below the frequency of human hearing are called infrasound, while sound waves with frequency above the range

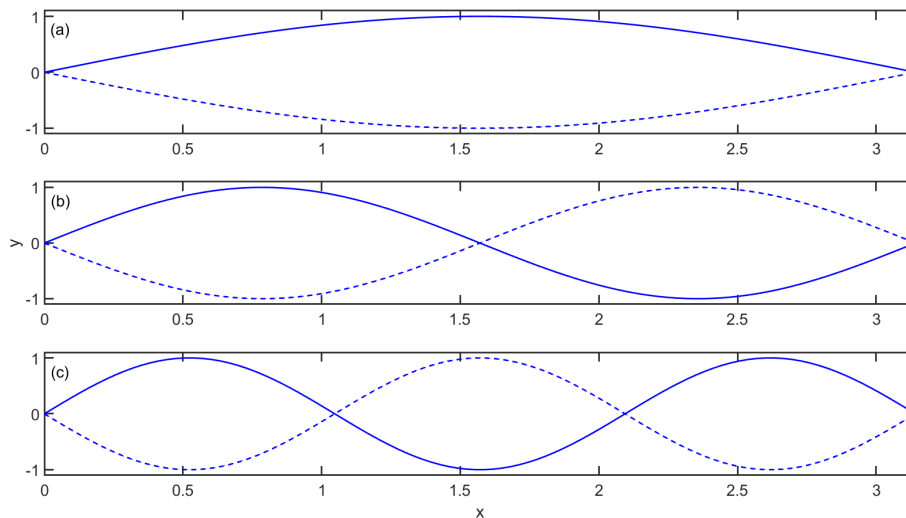


Figure 1.7: Example of standing waves in a string. (a) The fundamental; (b) first harmonic; (c) second harmonic.

of human hearing are called ultrasound. Ultrasound devices operate in a range from dozens of KHz up to GHz. In this particular case, acoustophoretic devices commonly works with a frequency of MHz. The manipulation of particles using acoustic waves is well established in macroscale systems and more recently it has been transferred to microfluidics, offering an innovative and alternative technology for cell and particle manipulation in Lab-on-a-Chip and microfluidic analysis systems [49, 50]. It is a quite new approach and recent studies have shown a good match between acoustophoresis and known methods of manipulating particles such as electrophoresis, hydrodynamical systems and magnetophoresis (for further details on these see [subsection 1.2.1](#)). Different continuous flow acoustophoretic devices were reported in literature such as layered resonators [51], transversal resonators [52] and SAW systems [53]. The common feature of them is the pressure node located in the centre of the flow channel with the antinodes at the sides. Beside that in literature are also present a high number of reports which describe multi-wavelength resonators for cell and particles manipulation or trapping. Since in this project we focused our attention on bulk acoustic waves with half-wavelength transversal microfluidic resonator, a brief overview of some applications of this kind of system is presented.

One of the most reported application is the continuous flow concentration of cells and particles [50, 54, 55, 56, 52]. Generally speaking, a standing acoustic wave is characterized by points that remain fixed during every oscillation. These points are pressure nodes, when the value of the wave is zero, or antinodes, where the magnitude oscillates from the maximum value to the minimum and vice versa (as sketched in [Fig.1.9](#)). Cells, which present a higher density than the suspending medium, are focused at the node of

the acoustic wave creating a concentrated zone and a purified one. The flow is simply split with different outlets obtaining a fraction containing the concentrated particles and another one with a particle free medium. One of the first acoustofluidic cell concentrators was presented by Yasuda et al. [54, 55]. In this study a quartz chamber with half-wavelength width was used to concentrate red blood cells. This work was important for future outlooks, it was the first one to discover that ultrasound (in the range of MHz) does not damage the cells. Silicon is commonly used as bulk material for microfluidic acoustic resonators because it presents high difference in acoustic impedance respect to aqueous solutions. The silicon-based channel is usually sealed with a glass lid. Generally, the process to seal them is the anodic bonding which guarantees hermetic properties of silicon-glass channel structure without the need for adhesive interfaces. One of the first silicon chip with one inlet and two outlets was developed by Harris et al. [56]. The aim of this design was to concentrate particles in the nodal plane parallel to the flow and withdrawn in the central outlet and the clarified medium collected through the others. Nilsson et al. [52] presented the first silicon device which worked with transversal mode. In this type of systems, the standing wave is created perpendicular to the flow, in plane with the section of the chip. Respect to the common silicon etched channel and sealed with the glass lead, a "sandwich-like" microchannel was reported in literature [57]. As the name let to intend, it is silicon etched through the wafer and two glass sealed at the top and the bottom. Wiklund et al. [57] was the first one to use this type of microchannel with an inverted microscope.

Acoustic focusing is another common application of acoustophoresis. While concentration process aims to obtain the higher number of particles per volume of sample, usually in acoustic focusing the purpose is to obtain a particle free sample at the outlet. The configuration is the same but with a flow splitter after a half wavelength acoustic focusing step. This process usually fail with high particle concentrations, due to loss of them into the purified fraction. A multiple step device has been developed to overcome this problem [58]. A dense stream was sequentially purified in the central zone of the channel. The main application of this device is plasmapheresis from undiluted blood. Cells were removed after the focusing through sequential exit holes placed in the centre bottom of microchannel. This permits to decrease the concentration gradually until the final fraction was removed and a flow splitter let to obtain a purified blood plasma with low cells content.

Particle separation using acoustic waves has widely grown interest in research. The main approach is called **FFA**. The net acoustic force generated in the fluid drives particles towards pressure node of the standing wave meanwhile they are dragged in the direction of the flow. In this kind of systems, hydrodynamic and acoustofluidic are coupled and the separation is strictly dependent on the geometry of the channel and flowrates. and In-line multiple particle separation can be achieved in the same device if the laminar flow is divided in different outlets, collecting fractions of bead that have travelled inside the channel at different velocities in relation to the experienced acoustic radiation force. Fig. 1.8 schematically shows the principle of **FFA** with multiplex

mode separation [50]. As could be intended looking at Fig.1.8, it is important in this

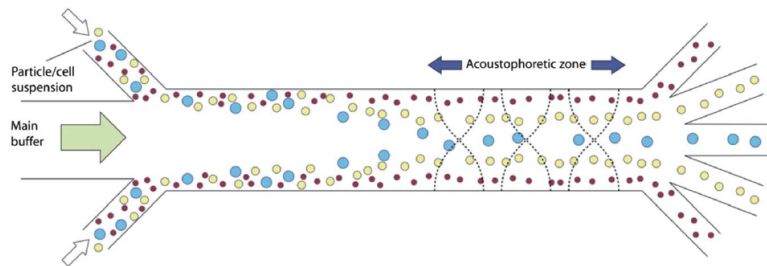


Figure 1.8: Schematic representation of FFA with a particle mixture [50]. As the acoustophoretic is size dependent, particles with same properties but different radius are moved differently toward the node (or the antinode). In this case for example bigger particles, which are focused faster can be easily collected in the central outlet. On the other hand, if the flow rates and the applied field are tuned correctly, it is possible to also isolate the yellow particles and the red ones in different outlets.

kind of systems to tune the flowrates. An important study which report a microchip integrated free flow acoustophoresis in a half wavelength transversal resonator was published by Petersson et al. [59]. In this work a continuous separation of a polystyrene microparticle mixture was investigated. It is now simpler to understand that one of the main goal of a single mode FFA is to divide the mixture in two fractions which can be collected through the central outlet (larger particles) and the sides outlets (smaller particles). From the union of this basic concept and the rising interest in concentrating circulating tumour cells using microfluidic, several studies demonstrate the possibility of the separation of these particles using acoustophoresis. One masterpiece came from Augustsson et al. [60] who described a dual outlet device for enrichment of tumour cells inside a blood sample. After a lysing step of red blood cells (RBC), the remaining white blood cells (WBC) with the tumour cells were processed inside a FFA device and collected in the central outlet.

Another approach to achieve the separation is to use different properties of the particles. If there is an opposite contrast factor (eq. 2.48) between two population of particles, thus significantly different density and compressibility (for further information see section 2.2), particles will be moved by an acoustic radiation force in an opposite direction. This is called "binary acoustophoresis". Particles which present an higher density than the suspending medium and a positive acoustic contrast factor will be pushed toward the node of the acoustic standing wave, at the opposite side particles with a lower density and a negative value of the contrast factor will focus at the pressure antinodes. The first biomedical device for the separation of erythrocytes and lipids was developed by Peterson et al. [61, 62] and a generic sketch is shown in Fig. 1.9. In this study for example, red blood cells present a positive acoustic contrast factor, thus collected in the centre of the cross-section, where it is placed the node of the standing wave. Lipids

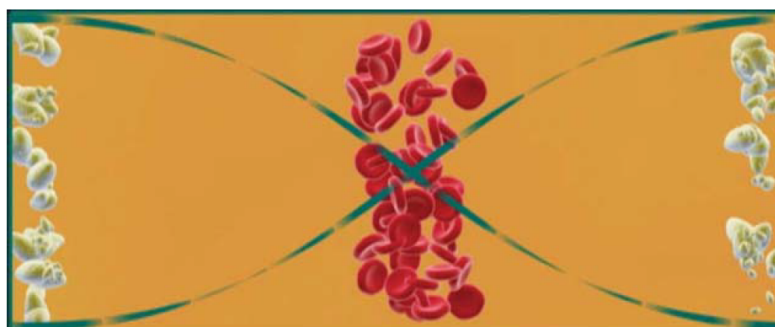


Figure 1.9: Sketch of binary acoustophoretic separation in a rectangular cross-section. Red blood cells which present a positive contrast factor are focused at the node of a standing acoustic wave. Lipids experience the opposite behaviour due to their negative contrast factor [61].

which present a lower density than water are collected at the sides of the channel, as shown in Fig.1.9. Introducing the concept of binary acoustophoresis, it is underlined the importance of knowing the target specie properties. For optimal acoustic separation, for example, fresh cell samples are preferable to avoid the presence of aggregate, cluster, dead cells and thus different behaviour in the acoustophoretic process [50]. Another important aspect for acoustic separation needs to be considered. The size of the particles influence the efficiency of the process, as shown in more detail in [section 2.2](#). In fact, the lower size limit where the acoustic radiation force is dominant is about $1 \mu\text{m}$. Since this force is depending by particles radius with the cubic metre, it is dominant for bigger particles. On the other side, hydrodynamic forces, generated by acoustic streaming and dependent linearly by the radius, move smaller particles making the separation harder. A more detailed explanation of the physics behind this process is explained in [section 2.2](#).

As shown previously in this chapter, several microfluidic approaches for the separation of nano- and micro-particles were developed. The necessity to overcome the common techniques limitations remains an important task. As mentioned above, differential centrifugation is the most widely used method for the isolation of vesicles, but it is time-consuming and the equipment is expensive and only low volume samples can be processed, limiting this method applicability for clinical purposes. In addition, large volumes of sample are normally processed with ultracentrifugation and, even though this could be an advantage when working with cell culture supernatants or certain types of biological fluids (like urine), it could constitute a potential drawback in case of plasma samples. Indeed, plasma recovered from individual patients is limited to few millilitres and the development of purification protocols which use small volumes of plasma are

therefore essential [63]. Ultrafiltration and precipitation represent faster and more efficient methods to isolate exosomes. Although both the techniques present their limits. For example, the purity of the isolated sample is very low due to the presence of contaminant proteins or the vesicles can break due to mechanical stresses. Alvarez et al. [64] compared the yield obtained from some of the most used protocols for exosomes separation. In this case urine was tested as biological sample. The highest number of exosomes per ml of urine ($\approx 2.7 \times 10^9$) was obtained using a modified exosome precipitation technique using ExoQuick_{TM} (section 1.1 - Extraction Using Exoquick_{TM}: Exosome Precipitation Reagent). On the other hand this protocol had very low purity in the obtained sample due to contaminant molecules. In general, every separation technique has its own advantages and disadvantages, and the most suitable method is chosen with their application. For example, the recovery yield is the parameter that has to be maximized for diagnostic purposes or the vesicle structure has to be maintained for drug delivery applications. Since some of the presented microfluidic techniques are label-free, with low mechanical stresses, simple to handle and cheap, the design and the optimization of a device can lead to the development of a powerful tool for the isolation of exosomes. The table below groups all the strategies and feasibility of the different potential applications for each isolation method Table 1.4.

The aim of this thesis was to investigate the development of a multi-staged microfluidic system, where a size-exclusion device was chosen as pre-cleaning stage and an acoustophoretic device for the separation of smaller cells. Furthermore, it is also highlighted the importance of the numerical approach for the design and the optimization of microfluidic devices. A filtration using pillar arrays was chosen because it represents a very intuitive and simple way to cut out big particles from a sample. The system developed can trap micrometer particles, but it presents several disadvantages and it needs further investigations and improvements. The acoustophoretic approach was chosen because is label-free, the sample does not require pre-treatment. Moreover, the device can be fabricated quite easily, it is reusable, and many researchers have utilised this technique to investigate biological particles manipulation.

Method	Type	Advantages	Disadvantages	Nucleic acid quantification and sequencing	Biomarker screening	Protein quantification and identification	Drug delivery systems
Centrifugation	Physical	Simple protocols Preservation of physicochemical properties	Specialized equipment required	Yes	Yes	No	Yes
Ultrafiltration	Physical	Fast protocols Cheap materials High protein and RNA line yield	Low purity Exosome deformation and extrusion	Yes	Yes	No	No
Precipitation	Physico-chemical	Highly reproducible High vesicle and RNA yields Requires only lab-bench equipment	Low purity Exosome aggregation	Yes	Yes	No	No
Chromatography	Physico-chemical	High exosome purity yields Preservation of physicochemical properties	Medium to high processing times Exosome degradation due to selected operation buffers	Yes	Yes	Yes	Yes
Microfluidics	Physical	Miniaturization Device functionalization Short analysis times	Low reproducibility Low exosomal yields Exosome aggregation	Yes	Yes	Yes	Yes
Immuno-capture	Chemical	High specificity High purity Potential scalability	Expensive materials Low exosomal and RNA yields	Yes	No	Yes	No

Table 1.4: General overview of exosome isolation methods. Advantages, disadvantages and main working principle are defined for each technique. The possible applications are identified for each method in the last four columns. Adapted from [64].

Chapter 2

Theoretical Background

In this chapter, the theory behind microfluidics and acoustofluidics is introduced. In the previous chapter ([chapter 1](#)) the importance of microfluidic devices for the separation of nanoparticles is showed, and some acoustophoretic applications are illustrated. The following pages aim to go deeper in the main governing equations to explain the physics behind microfluidics ([section 2.1](#)) and acoustofluidics ([section 2.2](#)).

2.1 Microfluidic Theory

The former section of this chapter aims to explain some theoretical aspects of microfluidic world. At the beginning a general overview of the fluid dynamic in microfluidic devices is reported. The continuum hypothesis is then introduced and the general governing equations, i.e. continuity equations and Navier Stokes equations are quickly explained. A particular attention has been dedicated to specific physical cases which are useful for modelling and analysing passive microfluidic systems. For a more in-depth treatment of the theoretical topics, we refer the reader to cited textbooks [[65](#), [66](#), [67](#), [68](#), [69](#)]

The term microfluidics is referred to the science of manipulating and controlling fluid in systems with characteristic dimensions in the scale between 100 nm and 100 μm . Microfluidic is a field that has seen great improvement in recent years with the development of several devices capable of overcoming classical laboratory techniques, allowing new functionalities and studying phenomena undetectable in macroscale systems.

To have a better understanding of the advantages of working at this scale, such as rapid diffusion [[70](#)], laminar flows, Dean vortices, faster thermal transport, the physics of fluid at the microscale is explained below. The main purpose of microfluidic devices is to handle fluids. These, which comprehend liquids and gasses, are characterized by properties that could change continuously, particularly when exposed to external forces. For example, in a fluid the presence of shear forces, will results in changing relative positions of fluid elements.

The most important dimensionless number is called Reynolds number (Re) which describe the ratio of inertial forces to viscous forces in a fluidic system, as follow,

$$Re = \frac{\rho v L}{\mu}, \quad (2.1)$$

where ρ is the fluid density, v is the mean velocity, L is the characteristic length and μ is the dynamic viscosity. Physically speaking L is an important dimension that gives information about the scale of the system. For example, if the flow in a pipe is considered, the characteristic length in Eq. 2.1 is the diameter of the pipe. In the case of non-circular tubes, as usually for microfluidic channels, it is equal to the hydraulic diameter D_h , defined as follow

$$D_h = 4A_c/p \quad (2.2)$$

Where A_c is the cross-sectional area of the tube and p is the wetted perimeter. Due to the linear dependency of the Reynolds number to the characteristic dimension of the system, in the microscale Re is reduced. When the Reynolds number is below 2000, the fluidic regime is called laminar [71]. For example, if a microfluidic system composed by a straight channel with a width of $100 \mu\text{m}$ is considered, where water is flowing with a mean velocity of 1 mm/s . The fluid density of 1 g/cm^3 and a viscosity of 0.001 N s/m^2 , the Reynolds number is of the order of 0.1. As expressed before, in such low values of Re , turbulent phenomena do not occur, and hence diffusion of species is a very slow process, respect to the convection.

One of the main solutions for enhancing the mixing of two species is the significant increasing of the contact area. This is achievable for example by injecting the samples through discrete via holes or multichannels in the microfluidic system. Other several approaches were proposed in literature to enhance the mixing both active and passive, such as hydrodynamic focusing, alternate injection, geometry effect, electrokinetic and stirring by particles [72].

Another important dimensionless number, which relates the advection and diffusion of molecules in a fluid domain, is called the Péclet Number Pe ,

$$Pe = \frac{vL}{D}, \quad (2.3)$$

where D is the coefficient of diffusion. Also in this case, the dimensionless number is linearly dependent by the characteristic length. Using other words, in microfluidic systems the advection phenomena is less influential than the diffusive transport.

Another difference between macro- and microscale is the relevance of surface and interfacial tensions. The former one expresses the fluid capacity to adapt its surface to the air to reduce the free energy. The same phenomena is described by interfacial tension, but it happens when an interface fluid-fluid is present, for example, oil in water. When the characteristic length is in the order of microns these tensions dominate on the gravity. This is useful, for example, when capillary forces are used. This last is the

force on a fluid which usually permit it to move through a porous material or narrow chamber.

Also, reaction time scale is lower in microfluidic systems compared to conventional devices. This phenomenon is clearly linked to the faster diffusion of molecules due to the smaller characteristic length. The characteristic diffusion time can be approximated as

$$t_{diff} \approx \frac{x^2}{2D} \quad (2.4)$$

where x is the distance travelled by molecules of solute after a time t , and D is the coefficient of diffusion [71]. It is simple to notice that the decreasing of the characteristic dimension of a system lead to reduced time taken for the molecules to travel across the system.

Another important dimensionless number in microfluidics is the Bond number. It is defined as follow,

$$Bo = \frac{\rho g L^2}{\gamma} \quad (2.5)$$

where ρ is the fluid density, g is the gravitational acceleration, L is the characteristic length of the system, which could be for example the radius of a pipe or the radii of curvature for a drop, and γ is the surface tension. The Bond number express the relation between gravitational force and surface tension force. In microfluidic, due to the scale of the systems, usually the Bond number is small, thus the surface tension force dominates over the gravitational one.

Due to these underlined properties, microfluidic systems have taken a great role in biological and chemical studies. Additionally, since the dimensions of the devices are reduced, reagents demand is lower than conventional systems, making them an optimal alternative when the cost of the chemicals is a problem.

2.1.1 The continuum hypothesis

Instead of fluids are characterized by a scale-length of inter-molecule spaces, in fluid-mechanics and particularly in microfluidics, the fluids are described as a continuum. This means that the fluid properties are examined as the average, rather than the individual molecule's parameters. The continuum approximation states: "The macroscopic properties of the fluid are the same as if the fluid were perfectly continuous, instead of as in reality consisting of molecules" [65]. In this case physical quantities such as the mass, momentum and energy can be considered as the sum of the corresponding quantity for the molecules inside the control volume of fluid [65]. So, the continuum hypothesis is not valid anymore when the considered system is examined on the molecular scale. Since in microfluidics the continuum hypothesis holds most of the times, throughout this study the approximation is used.

2.1.2 The continuity equation

The continuity equation describes the conservation of mass in classical mechanics. The general expression of the continuity equation is

$$\partial_t \rho + \nabla \cdot (\rho \mathbf{v}) = 0 \quad (2.6)$$

where ρ is the fluid density, \mathbf{v} is the velocity field, and their product represents the mass flow per oriented unit area per unit time, or mass current density.

When the flow velocities are much smaller than the speed of sound in the liquid, the fluid can be considered as incompressible [65, 66]. In other terms, there is not changing of the density in time, thus the continuity equation can be simplified in the following form.

$$\nabla \cdot \mathbf{v} = 0 \quad (2.7)$$

The rough meaning behind Eq. 2.7 is that fluid cannot appear from nowhere and cannot vanish into nowhere [69]. For an homogeneous fluid, the density can be known as function of temperature and pressure from the thermodynamic equations of state [66]. If the isothermal condition is taken in account, density is dependent only on pressure.

2.1.3 The Navier-Stokes equations

Newton's second law can be formally stated as,

"the rate of change of momentum of a body is directly proportional to the vector sum of the forces applied, and this change has the direction of the applied forces."

If this law is applied to fluid motion, is called the Navier-Stokes equation. If a particle, with a constant mass m is considered, and external forces are applied, Newton's second law can be expressed as,

$$m d_t \mathbf{v} = \Sigma_j \mathbf{F}_j \quad (2.8)$$

where $\Sigma_j \mathbf{F}_j$ is the vector sum of the applied forces. In the field of fluids is common to consider densities (properties divided by the volume) and, in this case, the mass density ρ and force densities \mathbf{f}_j are obtained. The material (or substantial) time-derivative has to be introduced in the equation to physically correct the equation of motion, thus Eq. 2.8 takes the form

$$\rho D_t \mathbf{v} = \Sigma_j \mathbf{f}_j \quad (2.9)$$

where D_t is the material derivative and \mathbf{f}_j are the force densities. Eq. 2.10 gives a clearer definition of the substantial time-derivation for a generic vector field $g(\mathbf{r}, t)$ [68, 73].

$$D_t g(\mathbf{r}, t) \equiv \partial_t g(\mathbf{r}(t), t) + (g(\mathbf{r}, t) \cdot \nabla) g(\mathbf{r}, t) \quad (2.10)$$

If we express the definition of material derivative in Eq. 2.9, the Navier-Stokes equations now become,

$$\rho(\partial_t \mathbf{v} + (\mathbf{v} \cdot \nabla) \mathbf{v}) = \Sigma_j \mathbf{f}_j \quad (2.11)$$

In the case where passive microfluidic systems are considered, thus there are not external fields applied, the term of force density is composed by gravitational force density, pressure-gradient force density and viscous force density. If a newtonian fluid is considered, thus the viscosity η is independent on stress state, velocity of the flow, space, and time. The Navier-Stokes equation so becomes,

$$\rho(\partial_t \mathbf{v}) = \nabla \cdot (\sigma - \rho \mathbf{v} \mathbf{v}) + \mathbf{f}, \quad (2.12)$$

where σ is the stress tensor for the fluid and \mathbf{f} is the sum of bulk forces acting on the fluid. For a newtonian fluid the stress tensor is

$$\sigma = \eta[\nabla \mathbf{v} + (\nabla \mathbf{v})^T] - \mathbf{I}[p + (\frac{2}{3}\eta - \eta_B)\nabla \cdot \mathbf{v}], \quad (2.13)$$

where \mathbf{I} is the unit tensor, η_B is the bulk viscosity and T denote the transpose. When the fluid is a liquid, i.e. water, thus considerable newtonian and incompressible, bulk viscosity can be neglected [67] and the Navier-Stokes equation is simplified as follow,

$$\rho(\partial_t \mathbf{v} + (\mathbf{v} \cdot \nabla) \mathbf{v}) = -\nabla p + \eta \nabla^2 \mathbf{v} + \rho \mathbf{g}, \quad (2.14)$$

As the Navier-Stokes equations are a partial differential equations with more unknown parameters than equations, it is not possible to obtain a full analytical solution. So, it is important to set the right conditions in particular to the domain boundaries. The most important and most often used boundary condition at the wall, it is the so-called no-slip condition. This states that the velocity of a fluid it is the same of the wall velocity (0 in the case of stationary walls). A well-known solution to the Navier-Stokes equation is obtained considering a steady, fully developed pressure-driven flow of a newtonian fluid in a straight channel. This specific case is called Poiseuille flow, and the solution is called Hagen-Poiseuille solution. From this, it is possible to obtain a relation between the pressure drop and the mass flow rate inside a long straight channel, as follow,

$$Q = \frac{\pi R^4}{8\eta L} \Delta P \quad (2.15)$$

where R is the channel cross-section radius L is the length, μ the dynamic viscosity, Q volumetric flow rate, ΔP is the pressure drop across the channel, also called as hydraulic pressure, meanwhile $\frac{8\eta L}{\pi R^4}$, represent the hydraulic resistance at the flow passage [69].

2.1.4 Stokes Flow and Drag Force

As expressed above, the general form of Navier-Stokes equations is nonlinear, due to the presence of the order two term in \mathbf{v} in the substantial derivation. The linearized

Navier-Stokes equations for steady (time independent) motion are known as creeping motion described by the so-called Stokes equations [66],

$$\nabla \cdot \sigma = -\nabla p + \eta \nabla^2 \mathbf{v} = -\rho \mathbf{f}, \quad (2.16)$$

$$\nabla \cdot \mathbf{v}. \quad (2.17)$$

The creeping flow condition is valid when the Reynolds number Re is small, typically encountered in microfluidic systems.

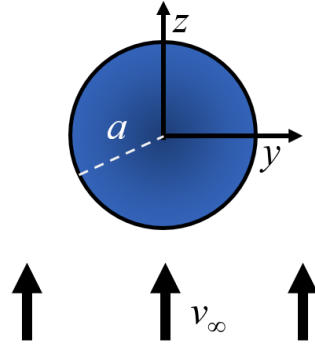


Figure 2.1: Sphere of radius a around which a fluid is flowing.

Considering the situation (Figure 2.1) of a static solid sphere of radius a immersed in a fluid with density ρ_{fluid} in motion in one direction (for example z) with a constant velocity far away from the interface v_∞ , in a condition of $\text{Re} \ll 1$. The submerged particle will modify the fluid trajectory, thus at every point on the sphere surface there are pressure and friction acting. The total force of the fluid on the particle is given by the sum of a buoyant force term and a drag term, as follow,

$$F = F_{buoyant} + F_{drag} = \frac{4}{3}\pi a^3 \rho_{fluid} g + 6\pi \eta a v_\infty \quad (2.18)$$

The first term, as previously expressed, is the force resulted by buoyancy, thus present with fluid at rest. The drag term is a kinetic force resulting by the fluid motion. For example, consider now a particle moving with a velocity \mathbf{u} at a position where the fluid, without the particle, would have a velocity \mathbf{v} . In this case, the drag force far from any wall or other obstacles, can be generalized to

$$F_{drag} = 6\pi \eta a (\mathbf{v} - \mathbf{u}). \quad (2.19)$$

2.2 Acoustofluidic Theory

This section provides the background in theoretical acoustofluidics necessary to introduce the numerical works of this thesis. In [chapter 1](#) we showed that the typical

acoustofluidic setup is a micro-sized cavity, filled with a suspension of particles in a liquid, all in presence of ultrasounds. It is important to underline that in all the study we treat the fluid as newtonian. At the beginning the conservation of mass and momentum are introduced, modified following the so-called perturbation theory, necessary for the acoustofluidic fields. Then we showed two important acoustic effects in microfluidic systems: acoustic streaming and acoustic radiation force. This phenomena are complex and the full treatment of the physics behind is explained in the referenced textbook by Bruus et al. [65] and in the thesis by Karlsen et al. [74]. At the end, the case of inhomogeneous fluid and acoustic streaming suppression is reported.

2.2.1 Basic governing equations - Conservation of mass and momentum

To form governing equations for the fluid, we recall eq. 2.6 and eq. 2.12, so the continuity of fluid mass density and fluid momentum density [75].

$$\partial_t \rho + \nabla \cdot (\rho \mathbf{v}) = 0 \quad (2.20)$$

,

$$\partial_t (\rho \mathbf{v}) = \nabla \cdot (\boldsymbol{\sigma} - \rho \mathbf{v} \mathbf{v}) + \mathbf{f}, \quad (2.21)$$

, where \mathbf{f} represents bulk forces acting on the fluid and $\boldsymbol{\sigma}$ is the stress tensor for a newtonian fluid defined as follow,

$$\boldsymbol{\sigma} = \eta [\nabla \mathbf{v} + (\nabla \mathbf{v})^T] - \mathbf{I} [p + (\frac{2}{3} \eta - \eta_B) \nabla \cdot \mathbf{v}]. \quad (2.22)$$

It is important to notice that in this case, the density in eq. 2.21 is not kept constant, thus because the fluid compressibility it is an important factor for the propagation of the wave (a more precise discussion will be exposed below). Another important aspect of Navier-Stokes equations for acoustofluidics is the presence of the bulk viscosity η_B . This parameter appears in the hydrodynamic equations when a newtonian liquid is considered and its compressibility is important since, coupled with the dynamic viscosity η , controls sound attenuation [76].

2.2.2 Basic governing equations - Diffusive and advective transport of solute

Since part of this work involved the study of the effect of acoustic streaming and the concept of inhomogeneity will be presented too, it is important to recall the advection-diffusion equation. For a concentration field $s(\mathbf{r}, t)$ of a solute with diffusivity D , and using a linear Fick's law for the diffusion flux, the equation is [75],

$$\partial_t s = \nabla \cdot [D \nabla s - \mathbf{v} s], \quad (2.23)$$

where the right-side terms represent the diffusive and the advective contribute, respectively.

2.2.3 Acoustic wave propagation

A particular attention has to be given to the physical interpretation of the equations. It is important to underline that all the theory and numerical models take in account the standard assumption of adiabatic wave propagation. This means that there is not heat exchange during the compression and expansion of the wave propagation, i.e. zero heat conductivity and isentropic system. Since the aim of this thesis is not to underline the maths behind the equations, we refer the reader to the main studies at the base of the acoustic wave propagation, from Epstein and Carhart [77], Allegra and Hawley [78], Landau and Lifshitz [79] and more recently Bruus [80].

Perturbation theory

One of the most used approach to linearise the non-linear conservation equations (i.e. Navier-Stokes equations) is to use the perturbation theory [79, 80, 81]. In simple words the perturbation theory consists in the decomposition of the fields through small perturbation from an equilibrium state denoted with "0". Thus the zero-state is an homogeneous, quiescent and isotropic fluid in an adiabatic system in equilibrium at a constant temperature T_0 .

Thus expanding all the fields to a second order perturbation (first order signed with "1" and second order with "2"), i.e. $g = g_0 + g_1 + g_2$, with a equilibrium quiescent condition $\mathbf{v}_0 = 0$, as already defined above, the fields in the fluid take the form,

$$\mathbf{v} = \mathbf{v}_1 + \mathbf{v}_2 \quad (2.24)$$

$$p = p_0 + p_1 + p_2, \quad (2.25)$$

$$\rho = \rho_0 + \rho_1 + \rho_2. \quad (2.26)$$

For this treatment is important to underline that the external actuation is time-harmonic, so all first-order field have a harmonic time dependent nature ($g(\mathbf{r}, t) = g(\mathbf{r}e^{-i\omega t})$). We will see later than this statement is very useful since the time derivatives of the first order fields can be written as $\partial_t \rightarrow -i\omega$.

First-order adiabatic equations

The acoustic field can be considered as a perturbation of the "0 state", and the acoustic small perturbation is defined through a parameter ϵ_{ac} ,

$$\epsilon_{ac} = \frac{|\rho_1|}{\rho_0} \ll 1. \quad (2.27)$$

Considering only the first-order perturbation and expressing the time derivatives as explained above, eq. 2.20 and eq. 2.21 take the form,

$$-i\omega\rho_1 = -\rho_0\nabla \cdot \mathbf{v}_1, \quad (2.28)$$

$$-i\omega\rho_0\mathbf{v}_1 = \nabla \cdot \boldsymbol{\sigma}_1, \quad (2.29)$$

$$\boldsymbol{\sigma}_1 = \eta_0[\nabla\mathbf{v}_1 + (\nabla\mathbf{v}_1)^T] - \mathbf{I}[p_1 + (\frac{2}{3}\eta_0 - \eta_0^B)\nabla \cdot \mathbf{v}_1]. \quad (2.30)$$

At this point, another equation is necessary to solve the system, so a relation of the first-order pressure p_1 and the mass density ρ_1 has to be developed. To do this the adiabatic approximation has an important role, i.e. the wave propagation in the fluid happens with negligible viscous losses [82]. So, it is possible to define the isentropic compressibility, choosing pressure and entropy s , as the two thermodynamic variables, as follow.

$$k_0 = -\frac{1}{V}\left(\frac{\partial V}{\partial p}\right)_s = \frac{1}{\rho_0}\left(\frac{\partial \rho}{\partial p}\right)_s, \quad (2.31)$$

where V is the volume of a given fluid particle and the subscript s implies that the differentiation is evaluated in isentropic conditions, $ds = 0$. Since the 1st order derivative of the pressure in terms of density has the dimension of velocity squared, it is possible to define,

$$c_0^2 \equiv \left(\frac{\partial p}{\partial \rho}\right)_s, \quad (2.32)$$

where c_0 is the isentropic speed of sound. Thus, coupling eq.2.31 and eq.2.32, the isentropic compressibility can be expressed as

$$k_0 = \frac{1}{\rho_0 c_0^2}. \quad (2.33)$$

A Taylor expansion to 1st order is used (around $p_0 = p(\rho_0)$), and the expression for the mass density becomes,

$$\rho(p) \approx \rho_0 + p_1 \rho_0 k_0 = \rho_0 + \frac{p_1}{c_0^2}, \quad (2.34)$$

where the relation between the speed of sound and compressibility (eq. 2.33) is used. Inserting eq.2.34 in eq. 2.28, it becomes,

$$-i\omega k_0 p_1 = -\nabla \cdot \mathbf{v}_1, \quad (2.35)$$

Solving the equations system given by eq. 2.35 and eq. 2.29, it is possible to obtain the vectorial 1st order velocity field and scalar 1st order pressure field (an example is shown in fig. 2.2). When the wave propagation is studied, viscous boundary layer thicknesses has great importance. It is defined as,

$$\delta_s = \sqrt{\frac{2\eta_0}{\rho_0\omega}}. \quad (2.36)$$

For water at room temperature, an actuation frequency $f=4$ MHz, the viscous boundary layer is around $0.3\mu m$. This represents the distance from all fluid-solid interfaces (i.e.

walls) where the viscous effects decay. Without going deeper in the nature of the shear waves, the higher damping is on the length scale of δ_s , with the maximum at the solid-fluid boundaries, meanwhile can be neglected at distances larger than $5\delta_s$ from any solid-fluid interface [82].

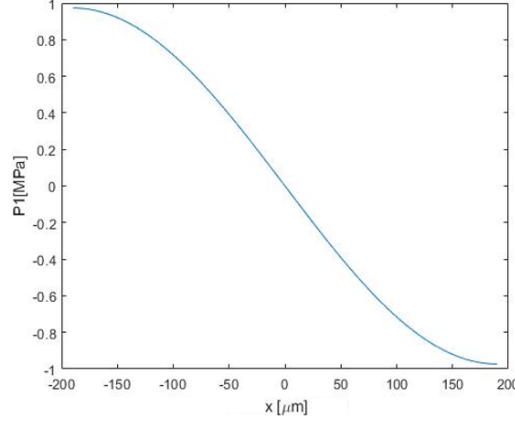


Figure 2.2: 1-st order pressure field at mid-height of a rectangular cross-sectioned microchannel, 380 μm width, 160 μm height at an actuation frequency $f=1.9669$ MHz

Second-order equations

Moving on to the second-order perturbation, eq.2.27, eq.2.24 and eq.2.25 are coupled to the continuity and Navier-Stokes equations, and products of first-order fields can give rise non-zero time-averaged effects [80, 82, 83, 84]. On the other hand, due to the harmonic time dependence of all first order fields, their time-average over period $T = \frac{2\pi}{\omega}$ is zero.

From now on, the time-average of a generic time-dependent field $g(t)$ is defined as,

$$\langle g \rangle = \frac{\omega}{2\pi} \int_0^{\frac{2\pi}{\omega}} g(t) dt. \quad (2.37)$$

Moreover, the time-average of any time derivative of the function $g(t)$ is zero $\langle \partial_t g(t) \rangle = 0$. In the following pages, all pure second-order fields are considered to be time-averaged, thus the angled bracket are neglected. So, the time averaged mass continuity equation 2.20 and momentum continuity equation 2.21 become respectively,

$$0 = \rho_0 \nabla \cdot \mathbf{v}_2 + \nabla \cdot \langle \rho_1 \mathbf{v}_1 \rangle, \quad (2.38)$$

$$0 = \nabla \cdot (\sigma_2 - \langle \rho_0 \mathbf{v}_1 \mathbf{v}_1 \rangle), \quad (2.39)$$

where the 2nd order stress tensor σ_2 is,

$$\sigma_2 = \eta_0 [\nabla \mathbf{v}_2 + (\nabla \mathbf{v}_2)^T] - \mathbf{I} [p_2 + (\frac{2}{3} \eta_0 - \eta_0^B) \nabla \cdot \mathbf{v}_2]. \quad (2.40)$$

One key part of developing these equations is based on the following rule, used to calculate the time average between products of 1st order fields [80, 82, 83, 84]. If $A(t)$ and $B(t)$ are harmonic time-dependent fields,

$$\langle A(t)B(t) \rangle = \frac{1}{2} \text{Re}[A^*(0)B(0)], \quad (2.41)$$

where * is used for complex conjugation.

Acoustic Streaming

When eq.2.38 and eq.2.39 are solved to obtain v_2 and p_2 , the so-called acoustic streaming fields are derived. Acoustic streaming is a steady oscillation time-averaged vortical flow driven by a divergence in the nonlinear momentum-flux-density tensor arising in the second order approximation [74, 75]. In microscaled systems this divergence is caused by the viscous dissipation mechanism [85]. This phenomenon was firstly investigated by Faraday [86] through experiments in 1831, and the first theoretical work was presented by Lord Rayleigh [87] at the end of the same century. This steady fluid motion is happening in a different time-scale respect to the 1-st order field [75, 82]. The slow-time scale hydrodynamic is in the order of millisecond to second compared to the fast first-order time scale which is proportional to $\frac{1}{f}$, i.e. μs at MHz frequencies. The steady streaming velocity v_2 plays an important role in microscale acoustofluidics, since the acoustic streaming field moves the particles and makes the focusing harder. In the case of a horizontal standing wave, as represented in Fig.2.3, a steady momentum flux is generated, commonly oriented from the pressure antinodes to the pressure nodes. Since this point are spatially fixed along the section, this results in the so-called inner boundary layer streaming (Schlichting streaming). Once they are generated, counter rotating streaming vortices inside the bulk of the fluid are induced [85]. These are called outer boundary layer streaming, or more commonly Rayleigh streaming [87]. From Landau and Lifshitz theory [79], it is shown that the boundary layer driven acoustic streaming has a noticeable magnitude if this condition is respected,

$$\lambda \gg h \gg \delta_s, \quad (2.42)$$

where λ is the wavelength, h is the characteristic dimension of the fluidic chamber and δ_s is the length of the viscous boundary layer.

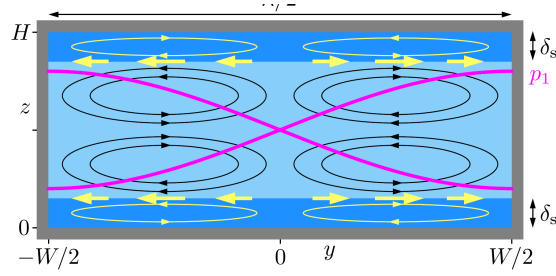


Figure 2.3: Sketch of boundary-driven acoustic streaming in the rectangular cross-section of a channel of width W and height H . The magenta line represents the horizontal half-wave standing pressure field. Yellow lines represent the inner boundary layer streaming, Schlichting streaming. Black loops are the boundary-driven Rayleigh streaming rolls. Adapted from [83].

2.2.4 Acoustic energy density in the fluid domain

In acoustophoretic systems, mechanical displacement is converted in small oscillatory motions and compressions/expansions in the fluid and in the solid of the device, represented by the 1st-order fields p_1 and \mathbf{v}_1 in the fluid domain. This phenomenon is associated with a magnitude of acoustic energy. So, the time average of the summed potential and kinetic energy, which come from the oscillatory movement, is called acoustic energy density E_{ac} with the unity of $[J/m^3]$ or $[Pa]$. This parameter is useful to characterize the acoustic field and commonly goes from 1 to 100 Pa [88], with the highest value when the actuation frequency is equal to the resonance frequency of the system. Following the theorem in eq. 2.41 and considering the harmonic time-dependent nature of the 1st-order fields, the time-averaged acoustic energy density is defined through \mathbf{v}_1 and p_1 as follow,

$$E_{ac} = \frac{1}{2}\rho_0\langle(\mathbf{v}_1(\mathbf{r}, t))^2\rangle + \frac{1}{2}k_0\langle(p_1(\mathbf{r}, t))^2\rangle. \quad (2.43)$$

2.2.5 The acoustic radiation force and the acoustic contrast factor

If a wave is propagating in a fluid and it encounters a suspended particles with different acoustic properties, the incoming sound wave is scattered on the particle [89]. This led to a transfer of energy and momentum from the surrounding fluid to the particles, and this last can experience an acoustic radiation force. Speaking about particles separation/concentration, it is clear the importance of the role that acoustic radiation force plays. A deep mathematical study is reported by Settnes and Bruus [89] and later by Karlsen and Bruus [90], and in this thesis the main result will be exposed .

Long-wavelength limit

When the particle radius a is much smaller than the acoustic wavelength λ , the dominant multipole contributions to the scattered field come from the monopole and dipole terms [77, 88]. Therefore, considering a particle of radius a , with a compressibility k_p and a density ρ_p (different from the suspending medium with density ρ_0 and isentropic compressibility k_s), for a general acoustic wave, it experiences an acoustic radiation force \mathbf{F}_{rad} given by [89],

$$\mathbf{F}_{rad} = -\frac{4}{3}\pi a^3 [k_0 \langle (f_0 p_1) \nabla p_1 \rangle - \frac{3}{2} \rho_0 \langle (f_1 \mathbf{v}_1) \cdot \nabla \mathbf{v}_1 \rangle], \quad (2.44)$$

where f_0 and f_1 are the monopole and dipole scattering coefficients respectively, defined as,

$$f_0 = 1 - \tilde{k}, \quad (2.45)$$

$$f_1 = \frac{2(1 - \gamma)(\tilde{\rho} - 1)}{2\tilde{\rho} + 1 - 3\gamma}, \quad \gamma = -\frac{3}{2}[1 + i(1 + \tilde{\delta})\tilde{\delta}], \quad (2.46)$$

with $\tilde{\delta} = \frac{\delta_s}{a}$ is the normalised boundary-layer thickness, $\tilde{k} = \frac{k_p}{k_s}$ is the compressibility ratio and $\tilde{\rho} = \frac{\rho_p}{\rho_0}$ is the density ratio.

Acoustic contrast factor

A standing plane wave in one-dimension (1D) has been widely used in experimental applications [50, 91, 92, 93, 94]. Silicon processed by anisotropic wet etching or Deep Reactive Ion Etching (DRIE) is one of the material used for lateral resonance acoustophoretic devices. Since it is expensive and the fabrication processes are complicated, recent studies presented devices fabricated in glass by isotropic etching [15]. In this case the acoustic radiation force equation (eq.2.44) can be simplified. For a 1D horizontal standing wave, thus parallel to the channel cross-section, the pressure node is placed in the centre of the channel, meanwhile the pressure anti-nodes (velocity nodes) is placed at the sides. With this profile, F_{rad} can be expressed as,

$$F_{rad}^{1D} = 4\pi\Phi_{ac} a^3 k E_{ac} \sin(2ky) \mathbf{e}_y, \quad (2.47)$$

$$\Phi_{ac} = \frac{1}{3} \text{Re}[f_0] + \frac{1}{2} \text{Re}[f_1], \quad (2.48)$$

with $k_y = \pi/W$ is the wavenumber in the half-wave resonance in a channel with width W , and y the horizontal coordinate (as represented in Fig.2.4). Φ_{ac} is the so-called acoustic contrast factor. As mentioned in the previous chapter (subsection 1.2.4), this parameter is fundamental for application such as binary acoustophoresis. In fact, the acoustic radiation force is linearly proportional to Φ_{ac} which takes in account of the difference in properties between the suspended particle and the medium. The sign of \mathbf{F}_{ac} is decided

by the acoustic contrast factor, for $\Phi_{ac} > 0$, the force is directed towards the pressure nodes of the acoustic standing wave (Fig.2.4), while for $\Phi_{ac} < 0$ it is directed in the opposite direction, thus towards the pressure anti-nodes.

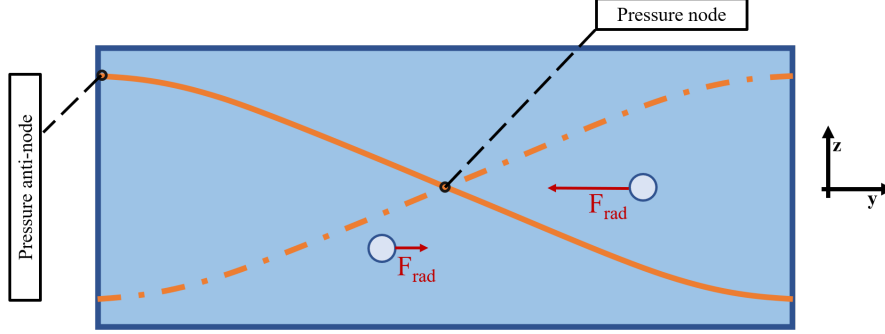


Figure 2.4: Sketch of the typical particle trajectories (red arrow) in a channel cross-section with a standing pressure half-wave acoustic field (orange line). A particle, with positive contrast factor ($\Phi_{ac} > 0$) and the size such that it can experience only acoustic radiation, is represented (blue circle).

2.2.6 Inhomogeneous fluids and acoustic streaming suppression

Until now a homogeneous fluid was considered. This means that all the properties such as ρ_0 , compressibility k_0 , viscosity μ_0 were considered constant in space and time. If an inhomogeneity fluid, which is caused by a solute concentration field $s(\mathbf{r}, t)$, the above mentioned hydrodynamic properties are varying. The concentration field, accordingly, to eq.2.23, is transported by diffusion and advection. So, in this case,

$$\rho_0 = \rho_0[s(\mathbf{r}, t)], \quad k_0 = k_0[s(\mathbf{r}, t)], \quad \mu_0 = \mu_0[s(\mathbf{r}, t)]. \quad (2.49)$$

where the dependencies vary based on the type of chosen solute. This fact lead to a divergence of the momentum-flux-density Π_{ac} and to the presence of an acoustic force density \mathbf{f}_{ac} acting on the fluid [75, 95]. The general expression for \mathbf{f}_{ac} is [75],

$$\mathbf{f}_{ac} = -\nabla \cdot \langle \Pi_{ac} \rangle. \quad (2.50)$$

$\langle \Pi_{ac} \rangle$ is the time-average momentum-flux-density and it is composed by the products of first-order fields, in particular,

$$\langle \Pi_{ac} \rangle = \langle p_{11} \rangle \mathbf{I} + \langle \rho_0 \mathbf{v}_1 \mathbf{v}_1 \rangle, \quad (2.51)$$

where $\langle p_{11} \rangle$ is a local oscillation-time-averaged acoustic pressure. Roughly speaking $\langle p_{11} \rangle$ can be seen as the difference between the potential and kinetic energy which come from the acoustic wave,

$$\langle p_{11} \rangle = \frac{1}{2} k_0 \langle p_1^2 \rangle - \frac{1}{2} \rho_0 \langle \mathbf{v}_1^2 \rangle. \quad (2.52)$$

Combining eq.2.50 and eq.2.51 the general expression for the acoustic force density in viscous inhomogeneous fluid becomes

$$\mathbf{f}_{ac} = -\nabla\langle p_{11}\rangle\mathbf{I} - \nabla \cdot \langle \rho_0 \mathbf{v}_1 \mathbf{v}_1 \rangle. \quad (2.53)$$

This force plays an important role for the suppression of the boundary-driven acoustic streaming: generally, inside the boundary layers the time-averaged stresses, caused by the dissipation of energy, lead to Rayleigh streaming flows. If a gradient in acoustic properties (i.e. density and compressibility) is present, the acoustic force density \mathbf{f}_{ac} tends to stabilize the concentration profile [96, 97], counteracting the advective transport phenomena [75], as shown in Fig.2.5.

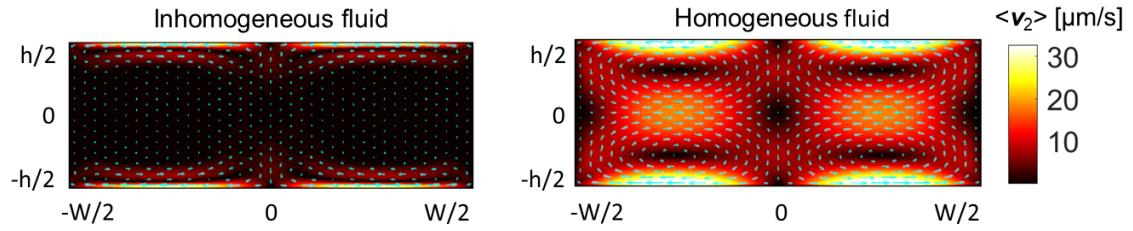


Figure 2.5: Comparison of acoustic streaming between inhomogeneous fluid and the corresponding homogenized fluid. Adapted from [75].

2.3 Numerical Model Background

This is a short section used to explain the Finite Element Method (FEM) and the Finite Volume Method (FVM) for solving partial differential equations (PDEs). The material for FEM is referred to the cited textbooks and thesis [65, 74, 98, 99, 100, 101]. The equations in this case were implemented in weak form and solved in the commercially available FEM software COMSOL Multiphysics®(version 5.4-5.5). Regarding FVM technique we refer the reader to the cited textbooks [73, 102]. In this case the equations solved were implemented in the commercial Computational Fluid Dynamic (CFD) software Ansys FLUENT®(version 18.0).

2.3.1 The Finite Element Method

The principle behind finite element modelling is to expand the interested fields on a set of basis function. As first step, the spatial domain of interest Ω is discretized by a grid (also called as mesh) into elements with node points where each basis function is associated. These functions are one at a node, while they are zero at the neighbouring nodes (as sketched in Fig. 2.6). A set of test functions $\{\hat{g}_n\}$, with the single function \hat{g}_n near the n 'th node, is introduced. In the example shown in Fig. 2.6, the test function is chosen to be linear, while usually are polynomial functions. This means that the set of

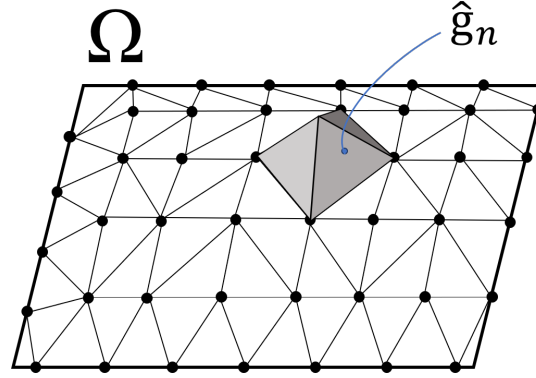


Figure 2.6: Sketch of test function \hat{g}_n on the domain Ω

test functions covers the entire domain, and adjacent \hat{g}_n overlap with the neighbouring functions. If a generic field $g(\mathbf{r})$ is defined on the domain Ω , it can be approximated in terms of test functions as follow,

$$g(\mathbf{r}) = \sum_n c_n \hat{g}_n(\mathbf{r}), \quad (2.54)$$

where c_n is the n 'th expansion coefficient that needs to be determined.

PDEs in weak form

Consider a boundary value problem described by the partial differential equations which govern the generic field $g(\mathbf{r})$ defined in the domain Ω , with the boundary conditions set at the domain boundary $\partial\Omega$. We consider now an inhomogeneous PDE on the general divergence form, derived from conservation laws,

$$\nabla \cdot \mathbf{J} - F = 0, \quad (2.55)$$

where \mathbf{J} is a generalized flux, and F is a generic driving force. It has to be noticed that \mathbf{J} is a vector but could as well be a tensor and F is a scalar which could as well be a vector. The basis of $\{\hat{g}_n\}$ cannot give a *strong solution* of the problem, but it can define a *weak solution*, which is an approximation valid, on average, for each mesh element. The weak form of the generic PDE in eq.2.55 is obtained by multiplying \hat{g}_m and integrating over the volume, as follow,

$$\int_{\Omega} \hat{g}_m(\mathbf{r}) [\nabla \cdot \mathbf{J} - F] dV = 0, \quad \text{for all } m. \quad (2.56)$$

Eq.2.56 represents the weak form of the generic PDE. Applying Gauss's theorem of the divergence and knowing that $\nabla \cdot (\hat{g}_m \mathbf{J}) = \hat{g}_m \nabla \cdot \mathbf{J} + \mathbf{J} \cdot \nabla \hat{g}_m$, it is possible to rewrite eq.2.56

into

$$\int_{\partial\Omega} [\hat{g}_m \mathbf{J} \cdot \mathbf{n}] dA + \int_{\Omega} [-\nabla \hat{g}_m \cdot \mathbf{J} + \hat{g}_m F] dV = 0, \quad \text{for all } m, \quad (2.57)$$

where \mathbf{n} is the outwards pointing surface normal.

Boundary conditions

The boundary conditions have a fundamental role in the boundary value problem.

- **Neumann boundary conditions**

This kind of boundary condition is used when a flux has to be imposed as constraint,

$$\mathbf{n} \cdot \mathbf{J} = N(\mathbf{r}) \quad \text{for } \mathbf{r} \in d\Omega. \quad (2.58)$$

In this case the flux at the boundary in eq.2.57 represented by the $\mathbf{J} \cdot \mathbf{n}$ term, is directly replaced by the desired flux $N(\mathbf{r})$.

- **Dirichlet boundary conditions**

For Dirichlet boundary conditions a function M , with dependency on spatial coordinates, has to be imposed as constraint on the field $g(\mathbf{r})$

$$M(\mathbf{r}) = g(\mathbf{r}). \quad (2.59)$$

2.3.2 The Finite Volume Method

In this section a brief introduction to the finite volume method is reported. **FVM** is a numerical technique that modify the **PDEs** over differential volumes into discrete algebraic equations over finite volumes [73]. As done with Finite Element Method ([subsection 2.3.1](#)), the first step in the solution process is the discretization of the domain Ω , which in the Finite Volume Method is divided into non-overlapping finite volumes [103]. The following step is the integration of the partial differential equations over discrete element. A system of algebraic equations needs then to be solved to obtain the values of the dependent variables for each element.

The Semi-Discretized equations

As explained briefly above, in the first step of the finite volume discretization process, the domain Ω is divided into discrete control volume. Usually, the boundaries (or faces) of control volumes are placed mid-way between two adjacent nodes. So, each node has a neighbouring control volume or cell. After that the governing equations are integrated over finite volumes into which the domain Ω has been discretized, then the Gauss theorem is used to change the volume integrals in surface integrals. This transformation is very important for this technique, since it is possible to obtain the value

of the dependent variables on the so-called face of the grid element [Versteed2007, 73, 102]. To a simpler presentation of the method a two-dimensional transport problem is used as example. The generic steady state form of the conservation equation for a general scalar variable $g(\mathbf{r}, t)$ can be expressed as [73]

$$\nabla \cdot (\rho \mathbf{v} g) = \nabla \cdot (\Gamma^g \nabla g) + Q^g \quad (2.60)$$

where $\nabla \cdot (\rho \mathbf{v} g)$ is the convective term, $\nabla \cdot (\Gamma^g \nabla g)$ is a generic diffusion term and Q^g is a source term. Integrating eq. 2.60 over the volume of element (V_C), the equation takes the form

$$\int_{V_C} \nabla \cdot (\rho \mathbf{v} g) dV = \int_{V_C} \nabla \cdot (\Gamma^g \nabla g) dV + \int_{V_C} Q^g dV. \quad (2.61)$$

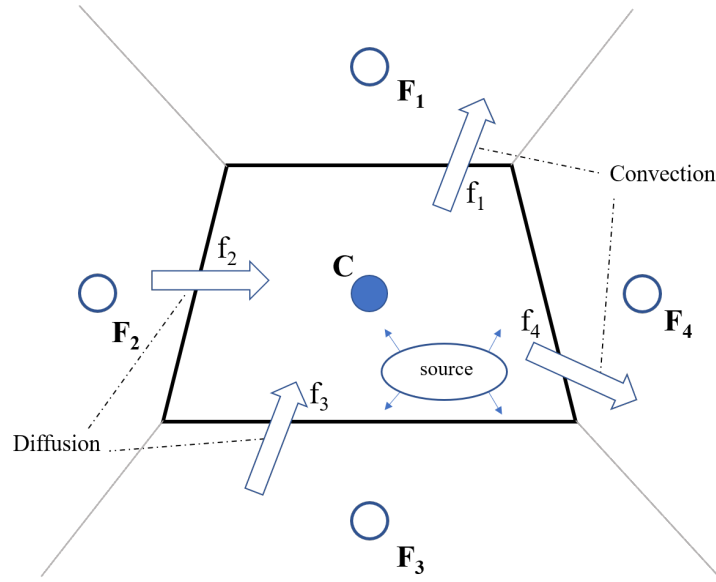


Figure 2.7: Sketch of the conservation in a discrete element C of volume V_C .

Using then Gauss theorem, thus replacing the integrals over volume into surface integrals, the above equation can be written as

$$\int_{\partial V_C} \mathbf{n} \cdot (\rho \mathbf{v} g) dA = \int_{\partial V_C} \mathbf{n} \cdot (\Gamma^g \nabla g) dA + \int_{V_C} Q^g dV. \quad (2.62)$$

Flux term integration over element faces

Using the notation from [73], the diffusion and convection flux terms are replaced by $\mathbf{J}^{g,Dif} = \rho \mathbf{v} g$ and $\mathbf{J}^{g,Conv} = -\Gamma^g \nabla g$ respectively. The total flux, defined as the sum of the two flux terms, is

$$\mathbf{J}^g = \mathbf{J}^{g,Conv} + \mathbf{J}^{g,Dif}. \quad (2.63)$$

If the surface integral over the entire element \mathbf{C} is replaced by the sum of all the fluxes f over all the element faces, the surface integral of the total fluxes become

$$\int_{\partial V_C} \mathbf{J}^g \cdot d\mathbf{A} = \sum_f \left(\int_f \mathbf{J}^g \cdot d\mathbf{A} \right). \quad (2.64)$$

To continue with the discretization the last term in eq. 2.64 has to be evaluated. To do this a Gaussian quadrature has to be used and the integral at the face f becomes

$$\int_f \mathbf{J}^g \cdot d\mathbf{A} = \int_f (\mathbf{J}^g \cdot \mathbf{n}) dA = \sum_{ip} (\mathbf{J}^g \cdot \mathbf{n})_{ip} w_{ip} S_f, \quad (2.65)$$

where ip identifies the integration point along the surface f and w_{ip} is the weighing function. The computational demand rises with the number of integration points over the faces used in the approximation, which obviously becomes more and more accurate. Thus, the total flux surface integral can finally be written as

$$\int_{\partial V_C} \mathbf{J}^g \cdot d\mathbf{A} = \sum_f \left(\sum_{ip} (\mathbf{J}^g \cdot \mathbf{n})_{ip} w_{ip} S_f \right). \quad (2.66)$$

Source term volume integration

For source term integration can be directly used the Gaussian quadrature integration. Thus, the last term in eq.2.61 becomes

$$\int_{V_C} Q^g dV = \sum_{ip} \left(Q_{ip}^g w_{ip} V \right). \quad (2.67)$$

As for the flux term the accuracy increases with increasing the number of integration points ip as well as the computational demand.

Chapter 3

Size Exclusion Passive Microfluidic Device

As expressed in the previous chapter Extracellular Vesicles, in particular exosomes, represent a potentially powerful diagnostic tool for the early detection of several diseases. An efficient separation technique is required to isolate these nano-particles from a biological sample. For obtaining that results a huge number of bigger cells has to be removed, such as red blood cells, white blood cells, platelets. Some of the most used conventional techniques were presented in [chapter 1](#). These approaches present some limitations, such as being time consuming, expensive, and dependent on large amount of volume. In the same chapter some microfluidic techniques are presented as possible approach to overcome these limitations. One passive method, that uses pillar-like structures, is the deterministic lateral displacement. Several studies regarding this technique [[27](#), [30](#), [31](#)] explored the possibility to separate biological cells through patterned obstacles arrays. The separation can be achieved also using pillars as filter. Wang et al. [[29](#)] presented a microfluidic device that can potentially trap exosome-like lipid vesicles through a nanowire-on-micropillar structure. In this study was observed that the lipids on vesicles membrane can be attached on the pillars and released after dissolution of the nanowires. More recently, A microfluidic device that uses linear array pillar was developed [[104](#)]. Balyan et al. studied the separation of poly-disperse suspension of 5 μm and 10 μm polystyrene particles. Other different studies used pillar structures in a cross-flow filtration. Kang et al. [[105](#)] developed a squared pillar structures with a gap smaller than 1 μm to perform plasma/blood separation. Chen et al. [[106](#)] proposed a straight channel closed between two pillar arrays for the cross flow separation of red blood cells. Due to the complexity of biological samples, such as blood, these systems may experience clogging and aggregation issues leading to a loss in separation efficiency and the fabrication of the pillar structures can be hard. The specific objective of this part of the thesis was to investigate the possibility to separate bigger cells in blood using a simple, reproducible, and disposable pre-cleaning device. In this context, a novel passive microfluidic device based on size-exclusion method is presented in this chapter, which

has led to the referenced paper [107]. Taking the idea from a particulate-trap-like filter, numerical simulations using the commercial CFD software ANSYS Fluent 18.0® were performed. Computational resources were provided by HPC@POLITO, a project of Academic Computing within the Department of Control and Computer Engineering at the Politecnico di Torino. The purpose behind the numerical tests was to optimize the geometry of the system and the shape of the pillars for the separation of big corpuscles in blood samples. Obtaining a purified medium it is possible to isolate nanoparticles (i.e. Extracellular Vesicles), which play an important role in several pathological and physiological processes [4]. In this context lies the necessity of separating nanovesicles, for example exosomes, to develop innovative tools for the treatments and diagnosis. Once the final layout was defined the device was produced with standard cleanroom processes. A Cyclic Olefin Copolymer was chosen as material for hot embossing replication.

Firstly a brief explanation of the numerical model is reported, referring to the main equations explained in [chapter 2](#). Then, an overview about materials and methods used for the experimental setup is reported and the results are presented in the last section of the chapter.

3.1 Numerical model

The starting point of this work was to study a particle filter inside a microfluidic channel, with dimensions of the cross section equal to $630 \mu\text{m} \times 15 \mu\text{m}$ ($W \times H$). The filter aims to separate particles bigger than $2 \mu\text{m}$, i.e. blood cells. The first chosen layout is shown in [Fig.3.1](#), where trapezoidal shaped pillars were thought to be spaced by $2 \mu\text{m}$ gaps, at the closest point. The microfluidic channel was thus divided by filtering modules. The distance between the wall and the posts was around $52.5 \mu\text{m}$. As can be seen on [Fig.3.1](#) the major base and the height of the posts were $30 \mu\text{m}$.

To describe the pressure and velocity field the continuity equation (eq. [2.7](#)) and the Navier-Stokes equations for incompressible, newtonian fluid (eq. [2.14](#)) were used.

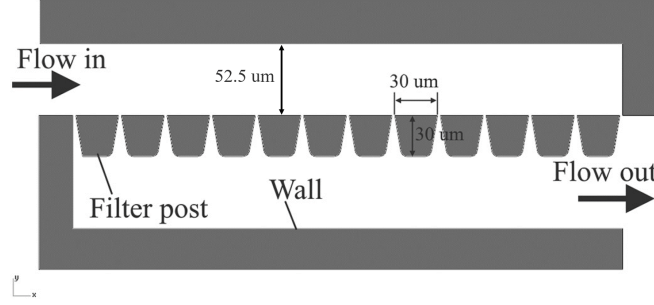


Figure 3.1: Sketch of the first geometrical layout of one filtering module. The distance from the wall to the posts is $52.5 \mu\text{m}$, and the smaller gap between the posts is $2 \mu\text{m}$. Reprinted from [107].

3.1.1 Boundary conditions and convergence analysis

The computational time of the whole 3D domain was decreased setting a symmetry plan at the mid-height of the channel. This assumption was considered reasonable, since the main separation effects took place in the transversal direction (along x-y plane in the coordinate system expressed in Fig. 3.1). A flow rate of $20 \mu\text{l}/\text{min}$ was imposed at the inlet through a constant velocity boundary condition of $3.42 \times 10^{-3} \text{ m/s}$. A pressure outlet boundary condition was set equal to atmospheric value. On all the other boundaries a no-slip condition was chosen, thus the velocity of the fluid was considered 0 m/s at the interface solid-liquid. No roughness was taken in account, and the device was filled by water at 25°C (properties reported in Table 3.1). An unstructured tetrahedral mesh was generated through the ANSYS built-in package. Due to the parabolic profile of the velocity inside a channel, a coarser mesh is present in the bulk, while it is going to be finest near to the walls where the gradient is greater. Thus, decreasing the maximum element size in the bulk and taking records of the residual, it was possible to perform the convergence analysis. The first value of size was chosen as $5 \mu\text{m}$. This last was decreased until the residual in continuity, x-velocity, y-velocity and z-velocity were under 1×10^{-5} . The best compromise for computational time and good convergence (shown in Fig.3.2) was a mesh element size with an element length of $2 \mu\text{m}$.

Property	Symbol	Value
Fluid density	ρ	$998.2 \left[\frac{\text{kg}}{\text{m}^3} \right]$
Dynamic viscosity	μ	$1.003 \times 10^{-3} \left[\frac{\text{kg}}{\text{m}\cdot\text{s}} \right]$

Table 3.1: Properties of water at 25°C .

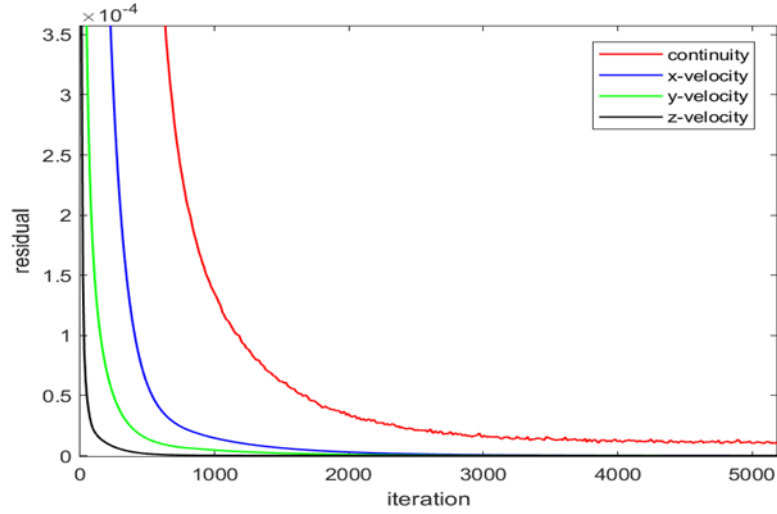


Figure 3.2: Residual of continuity, x-velocity, y-velocity and z-velocity for a maximum element size in bulk of $2 \mu\text{m}$.

3.2 Materials and methods

In this section the numerical approach for the optimization of the geometry is formerly exposed. The used materials, the fabrication process and the protocols for pressure tests and fluorescence tests are presented in the following part of the section.

3.2.1 Numerical optimization of the geometry

Homogeneity of the mass flowrate

Since the tricky problems of the filtration are localized close to the filtering modules, the attention of numerical models was focused on that region. Qualitative and quantitative analyses were necessary to guarantee both an homogeneous mass flowrate and a low pressure drop. The filtering module shown in Fig.3.1 was replicated four times occupying the whole width of the channel as shown in Fig.3.3(a). This layout corresponded to a filtering area of $1560 \mu\text{m}^2$. A contour plot of the velocity field obtained from the simulation of the steady laminar problem with the first layout is reported in Fig. 3.3(a). Looking at the contour plot, the velocity field seems to be homogeneous through all the filter's modules but analysing Fig.3.4, it is possible to notice that the last module, labelled as number 4, presented a huge difference in mass flowrate respect to the others. The necessity to avoid heterogeneity through the filtering modules led us to change the layout. This step was important because we were also able to improve the filtering area. Thus, the second layout, reported in Fig.3.3(b), was proposed. The total filtering area was now increased to $2730 \mu\text{m}^2$, changing the number of modules from four to

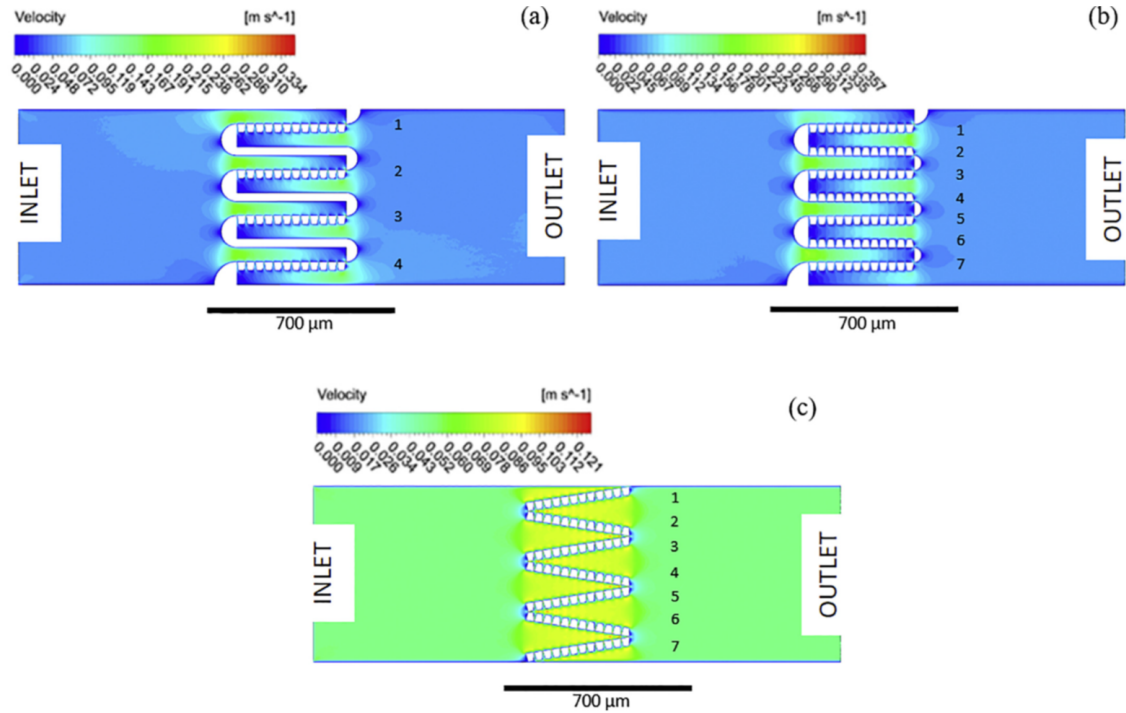


Figure 3.3: Velocity contour plots obtained with (a) the first, (b) the second and (c) the third layout. Colourbars from blue (0 velocity) to red (highest magnitude). Reprinted from [107]

seven. Instead of that, the obtained results were not better. The velocity magnitude increased, leading to an higher pressure drop and the mass flowrate presented more heterogeneity, as shown with a blue line in Fig. 3.4. A further step to overcome these problems is shown in Fig. 3.3(c), where the number of filtering modules was set constant but they were tilted of 8.4° to covering the width of the microfluidic channel. This structure led to an enhanced symmetry and the absence of closed structures which helped to homogenize mass flow rate, maintaining it almost constant among all the modules to 5.2×10^{-8} kg/s (red line in Fig. 3.4). Moreover, other important advantages were noticed: the stagnant regions, i.e. zero velocity areas, were reduced and the velocity magnitude was decreased noticeable, leading to less pressure drops and resultant lower shear stresses on the particles.

Analysis of the pressure drop

A control volume was chosen to analyse the pressure drop. Thus, a length of 2 mm from inlet to outlet was taken to qualitative model the filter. A value of 781.688 Pa for layout in Fig. 3.3(a), 653.365 Pa for layout in Fig. 3.3(b) and 593.701 Pa for layout in Fig. 3.3(c) were obtained imposing a flowrate of $20 \mu\text{l}/\text{min}$. A higher pressure in the first layout

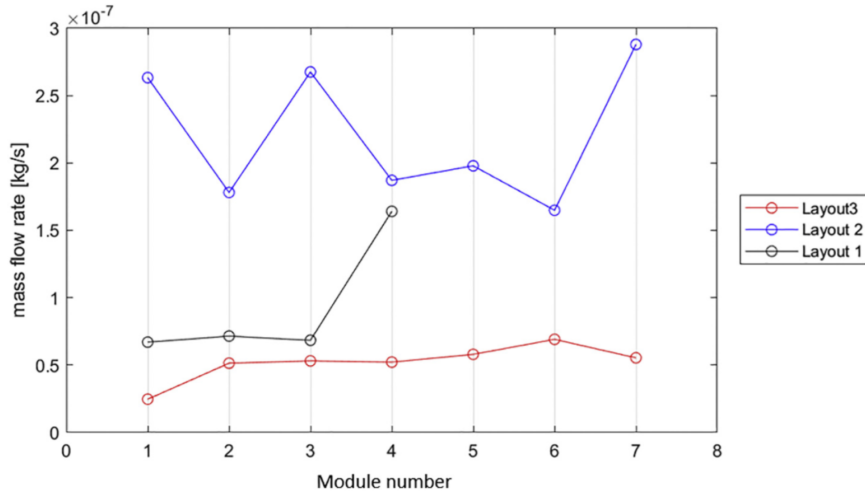


Figure 3.4: Mass flow rate through filtering modules for the first three layouts. Reprinted from [107].

was reasonably led to the presence of a higher number of closed structures. Since one of the main purpose was to have homogeneity in flow rate and lower pressure drops both for the filtration phase and cleaning one, we chose to continue the optimization using layout shown in Fig. 3.3(c). These conditions were set as target of the optimization for the following reasons: A homogeneity of flow rates, among all the modules, lets the sample flows discretized equally through each filter, avoiding unused zone. Furthermore, this condition helps to delay the possibility of clogging when the particles are injected. For what concern the pressure drop, it was a condition necessary to enhance the operational feasibility of the device. In fact, since the gap between the pillars is very narrow, also with low flow rate there should be issues to inject/withdraw the fluid.

A preliminary bonding test was carried out for a $630 \mu\text{m}$ wide and $15 \mu\text{m}$ deep channel. The aspect ratio, defined as width on depth ratio was proven to be too high, leading to channel occlusion due to the cover collapsing. Thus, looking to fabrication demand we chose to introduce walls between each filtering modules with a width of $20 \mu\text{m}$, which avoid the top cover collapsing. Indeed, the tilting angle of the posts had to be changed to a lower value of 5.7° . A sketch of this new layout is reported in Fig.3.5(a). From a numerical point of view the introduction of these walls increases a lot the computational demand due to the higher number of boundaries, thus finer mesh.

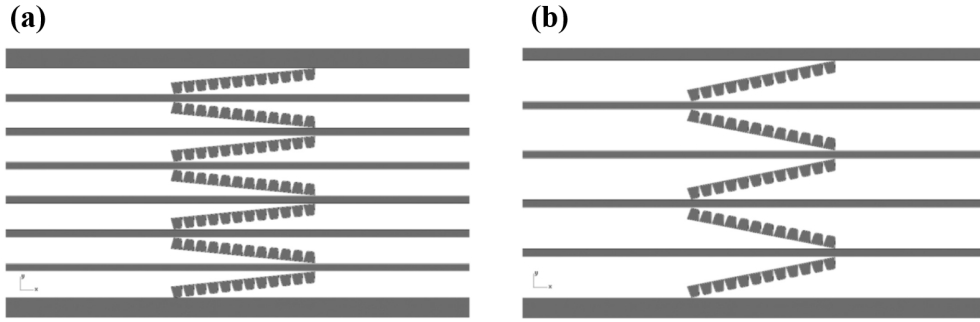


Figure 3.5: Sketches of (a) fourth and (b) fifth layout. Reprinted from [107].

Since each filtering module can be considered as a single channel, we decreased the computational time taking in account a single module and the analogy between microfluidic devices and electric circuits [108]. Considering then this approximation the control volume became a channel $75\ \mu\text{m}$ wide, $15\ \mu\text{m}$ high and $2\ \text{mm}$ long. The presence of walls permits to avoid zones with lower velocities, but the maximum value increased respect to the previous layout due to the decreased cross-section, as shown in Fig. 3.6). Instead of that, the results were promising, recording a pressure drop of $57993.7\ \text{Pa}$ along the channel and a mass flowrate through the module of $4.9 \times 10^{-7}\ \text{kg/s}$.

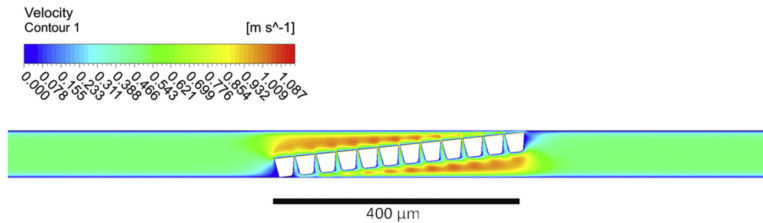


Figure 3.6: Velocity field contour plot in a filtering module of the fourth layout. Colour-bars from blue (0 velocity) to red (highest magnitude). Reprinted from [107].

Since this last layout presented good results, we chose to improve the quality keeping the same structure of the array of posts and aspect ratio, trying to decrease the pressure drops. The last designed layout is shown in Fig. 3.5(b), where the number of modules was decreased from seven to five, with a tilting angle of 11.3° and a total filtering area of $1950\ \mu\text{m}^2$. Following this geometry configuration the single module had $110\ \mu\text{m}$ of width respect to $75\ \mu\text{m}$ of the previous one, guaranteeing a lower velocity magnitude and the mass flow rate was $3.3 \times 10^{-7}\ \text{kg/s}$ ($20\ \mu\text{l}/\text{min}$). A contour plot of the obtained velocity field is shown Fig. 3.7.

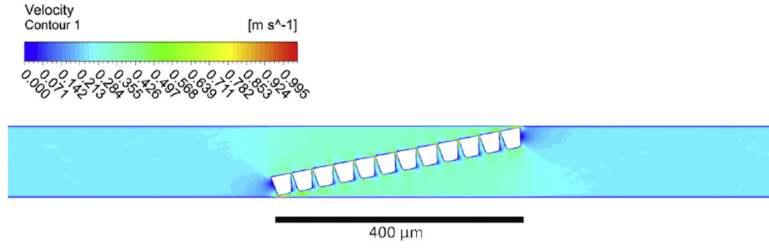


Figure 3.7: Velocity field contour plot in a filtering module of the fifth layout. Colour-bars from blue (0 velocity) to red (highest magnitude). Reprinted from [107].

As expressed in chapter 2 (subsection 2.1.3), a steady, laminar, pressure-driven flow of a newtonian fluid in a straight channel is known as Hagen-Poiseuille flow. Rearranging eq. 2.15 it is possible to have a relation of the pressure drop as function of the flow rate, of the fluid properties and the channel geometry.

$$\Delta P = \frac{8\eta LQ}{\pi R^4}, \quad (3.1)$$

where Q is the volumetric flow rate, R is the cross-sectional radius, in this case computed as half of the hydraulic diameter (eq. 2.2), L the length of the channel, η the viscosity of the fluid and ΔP is the pressure drop along the channel. Imposing a flow rate of 10 $\mu\text{l}/\text{min}$, ΔP resulting from numerical simulation was of 104.71 Pa and from eq.3.1 was 139.795 Pa.

3.2.2 Fabrication process

Numerical simulations led to the optimization of the filtering module's geometry, shown in Fig. 3.8. This last layout for the microfluidic device was formed by a channel 1 cm long, divided in five sub-channels, each 110 μm wide. The posts were kept in rows as in the first considered layout, but tilted respect to the lateral walls by 5.7° and 174.3° alternatively (Fig. 3.8). The shape of the posts was kept the same for all the studied layouts (Fig. 3.1), thus, trapezoidal with the major base and the height of 30 μm . This shape was selected and oriented, so the lower hydrodynamic resistance was opposite to the forward flow. Moreover, it was chosen to block the particles bigger than the gaps during the filtration step (forward flow), and to guarantee a low resistance during the de-clogging phase (backward flow). The gap between the posts was designed to be 2 μm but for the fabrication processes it was set to 3 μm . The production of the microfluidic device, with the filter inside, involved several cleanroom processes (schematically reported in Fig.3.9):

- **Silicon masking with photolithography**

A thin layer of the positive resist AZ1518 (MicroChemicals GmbH) was used to coat a 275 μm thick, single side polished silicon wafer (orientation 100). The adhesion was guaranteed by a previous spin coating (Spin150 - SPS Europe) of Ti

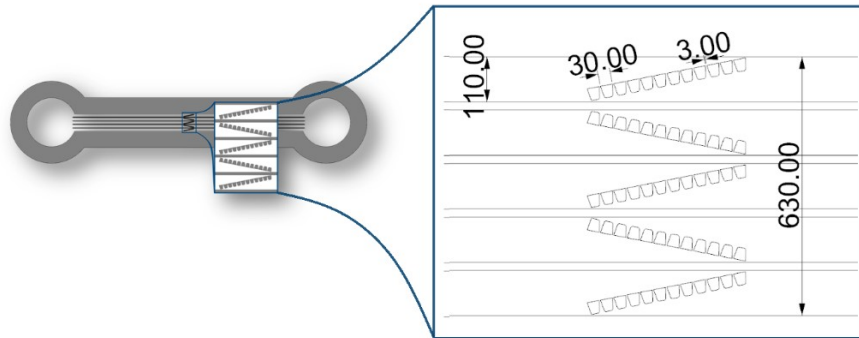


Figure 3.8: CAD drawing of the final layout for the microfluidic device. Dimensions are expressed in μm .

Prime (MicroChemical GmbH), which is an adhesion promoter. A direct photolithography process was carried out, writing six channels on the same wafer using a Laser Writer (LW405-Microtech). Resist was developed in a solution of AZ400K and then treated with Buffered Oxide Etch (BOE) for removing the silicon oxide layer. The next step was the anisotropic dry Deep Reactive Ion Etching (ICP-DRIE Oxford Plasmalab 100), following a conventional cryogenic process [109]. All the residual of the mask were then removed with acetone and BOE, then laser cutting was used to divide the master into six different wafers.

- **Hot embossing**

One of the masters was fixed on the upper plate in the hot embossing machine (HEX01 - JENOPTIK Mikrotechnik). On the lower one, a 1 mm thick Cyclic Olefin Copolymer (COC) foil was placed. The optimize process is a combination of time, pressure and temperature. Thus, the optimal parameters used in this work were 165°C with a load of 2500 N for 240 s. The hot embossing method was chosen for the possibility to rapidly fabricate disposable devices. Once a master is prepared, the hot embossing parameters (in terms of pressure, temperature, and time) are set. By using the same material in the same processing conditions, it can be said that a satisfying reproducibility is obtained. Surely, there are drawbacks. In fact, if the process is not accurate the opening between the filter posts can vary along vertical direction. A strict control over the process is needed to avoid this issue.

- **Final bonding.**

The replica obtained from hot embossing process needed to be treated to remove any exceeding material to have a strong and correct bonding. A numerical control machine was used either to cut the borders of the replica and to create the COC cover, not hot-embossed, for the microfluidic device. This last is just a rectangular foil with two hole drilled, the inlet and the outlet respectively. Before bonding the two parts, a cleaning step with isopropanol (IPA) was performed. After a step

of alignment using a digital microscope (DVM2500 - LEICA), the two foils were processed with hot-embossing. In this case 115 °C, 280 N of load for 360 s were set.

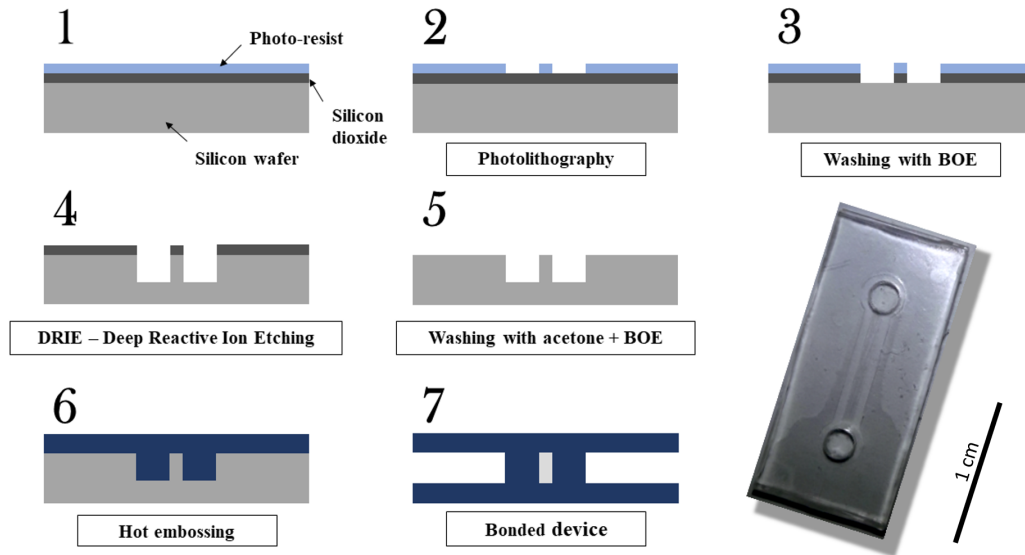


Figure 3.9: Schematic representation of the fabrication process (1 to 7) and example of produced device.

3.2.3 Fluorescence tests

A fluorescent particles dispersion was forced to flow through the filter to characterize the efficiency of the separation. The sample was prepared adding 50 μl of green polystyrene fluorescent particle (FluoSphere[®] - ThermoFisher used as received at a concentration of 5×10^8 particles/ml) into 1 ml of deionized water. The diameter of the particles is 4 μm with a surface modification with sulphate and a laser excitation wavelength (Ex) of 505 nm and a fluorescent emission wavelength (Em) of 515 nm. The size was chosen because it is very close to the platelets one ($\approx 2\text{-}3 \mu\text{m}$). To avoid formation of bubbles, deionized water was previously injected inside the channel until it was completely filled. The flow was guaranteed by a syringe pump system comprising a 250 μl Hamilton Gastight syringe, a New Era NE1000 syringe pump and polyurethane tubing (SMC TU0212C-20). Tests started when a 15 μl droplet was pipetted inside the inlet of the microfluidic channel and then withdrawn from the outlet with a flow rate of 5 $\mu\text{l}/\text{min}$ for 3 minutes. A 20 \times objective of a fluorescent microscope Nikon Eclipse Ti mounting a green filter (with an acquisition at 9.8 ms frame rate), was used to evaluate the efficiency of filtration through observation of the fluorescent streams. The suction

method was chosen to mimic the working of the filter in the described microfluidic platform: ideally, a small volume of blood is dropped directly inside the inlet of the platform and the withdrawn along the fluidic circuit, thus avoiding the dead volume issues linked to the injection of blood sample through a syringe.

3.2.4 Pressure tests

The tests performed to measure the pressure drop were important to both characterize the device and validate numerical results. The same setup from fluorescence tests was used for pressure tests, but in this last a tubing was used to connect the syringe to the inlet through a three-way valve. Deionized water was continuously pumped from the inlet to the outlet with a flow rate of 10 $\mu\text{l}/\text{min}$. The pressure sensor (Honeywell Microswitch - bridge pressure sensor 26PC Series) was placed in the third outlet of the valve and a pressure drop was acquired with the same protocol used by Bertanta et al. [110]. A total of three data series were recorded, starting from the activation of the syringe pump until the pressure plateau was reached. The pressure value obtained from the mechanical connection between the tubing and the microfluidic channel was considered as an offset and subtracted from the recorded data for each series. The maximum value of pressure, which was the one reached at the plateau was extrapolated, was considered for computing the average over the three measurement series.

3.3 Results

In this section all the obtained results from both the fluorescence and pressure tests are reported.

3.3.1 Fluorescence tests results

Fluorescence microscopy tests, as expressed above, were important to qualitative understand the efficiency of the proposed filter design. The photograms reported in Fig 3.10 show results from one of these tests. In particular, the flow of 4 μm green, fluorescent particles dispersion was studied. In the first photogram (Fig.3.10(a)) it is possible to notice the particles approaching the filtering module. Moreover, the channel is well filled by liquid dispersion and there are no bubbles, which indicates a successful bonding process. After 3 min withdrawal from the outlet of the channel (Fig. 3.10(b)), we observed that the particles were all collecting before the filter. At this point the flow was reversed to start the cleaning phase. Almost all the particles were pushed away from the filtering modules, and as it is possible to notice from Fig. 3.10(c), no particles were observed downstream the filter. All the tests were performed with an exposure time of 9.8 ms for the brightfield and 900 ms for the green field.

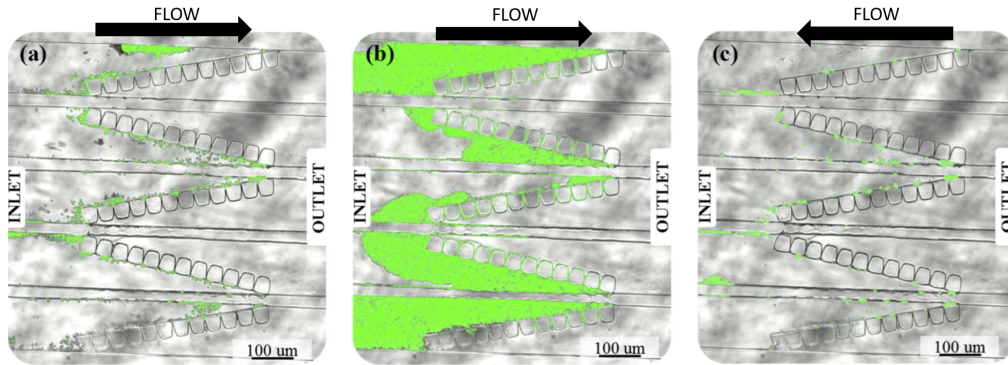


Figure 3.10: Photograms obtained from fluorescence tests inside the COC filter with $4\ \mu\text{m}$ particles dispersion. (a) particles approaching the filter, (b) infusion after 3 min and (c) filtering modules after cleaning phase. Reprinted from [107].

3.3.2 Pressure tests results

Following the protocol described above in section 3.2.4, we obtained a good match with numerical and analytical results. For an imposed $10\ \mu\text{l}/\text{min}$ flow rate, a pressure drop equal to 260 Pa was recorded. The absolute value is obviously different from the two obtained with eq.3.1 and simulations, but the order of magnitude is the same. This is reasonable if operational errors and experimental setup are taken in account.

3.4 Conclusions

In this chapter a passive microfluidic device was presented. Filtering modules were introduced inside a straight microfluidic channel produced through an embossing process involving a single master and polymeric replicas. This aspect has two advantages. The former is the usage of low-cost materials respect to silicon and Pyrex. The second lies on the reproducibility on the production of the device. A Numerical optimization of the design was performed to enhance the homogeneity of the mass flow through the filtering module and to have the lower pressure drop along the channel. Moreover, the device was studied to guarantee efficient alternating filtration and cleaning cycles. Pressure and fluorescence tests showed positive results. Using a suspension of polystyrene particles with $4\ \mu\text{m}$ diameter, filtration was proved to have a high efficiency. Also, the de-clogging phase presented good results, allowing for a clean device increasing its life. A possible further step should be the usage of biological fluids (e.g. plasma or plasma-like medium) to investigate the fluid-dynamic efficiency of the device. Blood samples could be used to analyse a more realistic condition. Another possible step could involve the investigation of a different cleaning system which could recover the particles

cake formed in the filtration phase. Using a complete blood sample could lead to different issues, since the concentration of blood cell is very high. The filter object of this study was intended as a preliminary approach to the filtration of the whole blood. This means that, with the aim of obtaining an efficient device, more elements should be investigated and introduced in the final microfluidic platform integrating the proposed passive two-way filter. For example, a dilution and a waste chamber should be added. The dilution chamber in order to slightly reduce the haematocrit level and add blood thinners to avoid clots due to the contact with microfluidic walls. A waste chamber to be used when reversing flow to allow, as mentioned above, blood big cells discarding a collection. Therefore, the filter would work in a more complex and multifunctional microfluidic circuit managed by alternate phases of infuse-withdraw to extend the device life itself.

Chapter 4

Parametric Numerical Study of Acoustophoretic Device

Trying to separate sub-micrometer particles with the optimized size-based exclusion device, we encountered two main difficulties: the former was the fast clogging of the filtering modules. The second one was the harder fabrication process needed to decrease the gap between the posts. We chose then to study and include an active separation device which could work after a size-based exclusion pre-stage and separate sub-micrometer particles from a previously treated sample. Our attention fell on acoustophoresis, technique that has gained great interest in the field of focusing and separation of particles ([subsection 1.2.4](#)) [111]. In this chapter a brief introduction about a common rectangular cross sectioned channel is reported. This is important to present one of the bulkier result of this work: a parametric numerical investigation of the geometry for the focusing/concentration of particles in a bulk acoustic wave [BAW](#) device. This part of the PhD project led to a published paper [112]. An overview of the numerical model, the used boundary conditions and the mesh convergence analysis is reported. At the end of the chapter the main results are shown and commented.

4.1 Rectangular cross-sectioned chamber

Commonly, the acoustic wave is generated by an actuated piezoelectric material, placed below the channel, which converts the electric voltage to mechanical displacements [113]. Numerous experimental (some reported in [subsection 1.2.4](#)) and theoretical studies [75, 83, 84, 91, 95, 96, 114, 115] investigated the half-wavelength resonance in a rectangular cross-sectioned channel. A sketch of the structure of a [BAW](#) device is shown in [Fig. 4.1](#). The acoustophoresis systems are mainly divided in three type: the layered resonator, the transversal resonator, and the surface acoustic wave resonator. The first one is a quite complex system that requires different layers, and a precise control of their thickness is required to obtain a high-quality factor. The surface acoustic wave

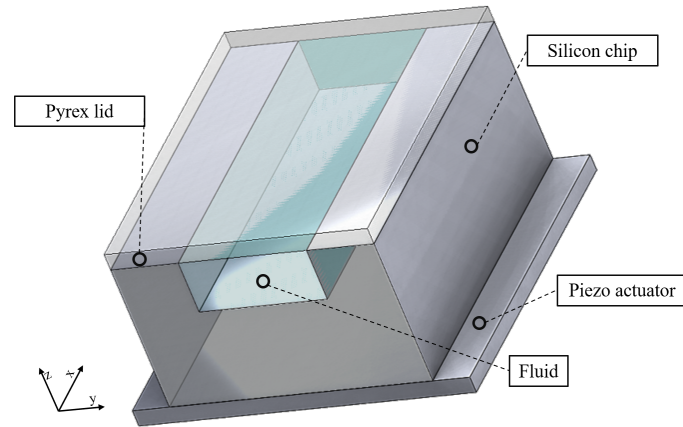


Figure 4.1: 3D sketch of a **BAW** microfluidic device.

(SAW) resonator worked based on the propagation into a fluidic chamber via a wave guiding substrate (usually LiNbO_3 , lithium niobate). In this case also polymeric materials are suitable for designing the chamber because they can have similar characteristic acoustic impedance as the fluid. The transversal resonators base their performances on reflection of the waves between the channel walls (as will be explained in more detail in the following part of the thesis). These systems have high quality factors and make these resonators less dependent on the material thicknesses and matched layers. Another great advantage on using transversal resonator is that the acoustic manipulation is performed in place with the resonator chip, that allows visual analysis of the focusing phenomenon. Furthermore, an integration with other microfluidic chips can be achieved [47]. As shown in Fig. 4.1, and reported above in chapter 1, the most used material for develop bulk acoustic wave devices is silicon sealed with a pyrex lid. In fact, silicon is a transparent material, useful for microscopy analysis, as well as it has an high acoustic impedance necessary to obtain a standing wave inside the fluidic chamber (denoted with "Fluid" in Fig. 4.1), since the walls must behave as reflector of the pressure wave. Since the main phenomena in the acoustophoretic applications happen in the transversal section (y - z directions in Fig. 4.1) and a full 3D numerical simulation has high computational demand, a common simplification is to consider a 2D problem, more particularly just the fluidic domain (Fig. 4.2). If a rectangular cross-section is considered with the width (W) designed to be half of the wavelength ($\lambda/2$) and the lateral walls are actuated following a sinusoidal behaviour, a standing acoustic wave with a single node in the centre of the channel is generated, while two anti-nodes are at the sides (as previously shown in Fig. 2.4.).

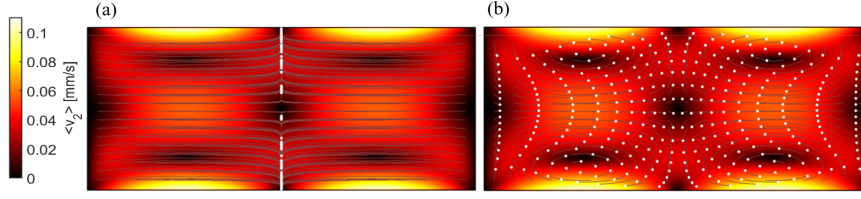


Figure 4.3: Contours plot of the acoustic streaming velocity in $380\mu\text{m} \times 160\mu\text{m}$ ($W \times H$) cross-section. (a) Particle trajectories with $5\mu\text{m}$ diameter. (b) Particle trajectories with $0.5\mu\text{m}$ diameter.

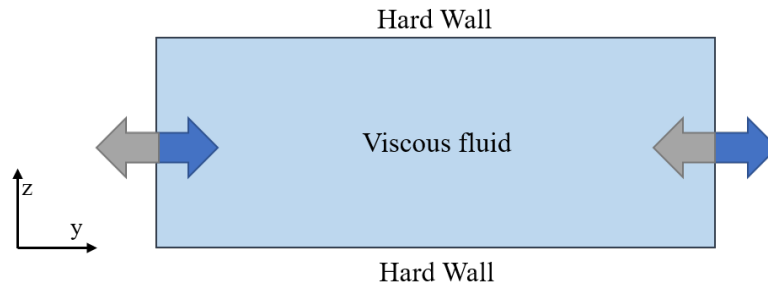


Figure 4.2: 2D sketch of the considered fluidic control volume, where the lateral walls are actuated and the ceiling and bottom are considered as hard walls. The blue and grey arrows indicate a harmonic oscillation.

If the actuation frequency is equal to the resonance frequency of the system the acoustic energy density E_{ac} has the maximum value as well as the corresponding pressure and velocity fields. This phenomenon is underlined in the referenced paper [114]. With this configuration, as theoretically introduced in chapter 2, particles with radius around $1\mu\text{m}$ and with a positive contrast factor Φ_{ac} are moved by the acoustic radiation force F_{ac} forward the node, as shown in Fig. 4.3(a). For particles smaller, the focusing becomes harder due to the acoustic streaming and the corresponding Stokes drag force F_{drag} (Fig. 4.3(b)). This phenomenon represents a limit when the task is to separate nanoparticles (such as exosomes), thus in the recent years, several approaches were numerically explored to overcome this size limit. For example, two half-wavelength resonances excited in a channel with a squared cross-section can generate a different vortex shape. Sub-micrometer particles, that feel both the contribution of the drag force and in minor way the acoustic radiation force, can be then concentrated into a focal point at the centre of the cross-section [116]. A more recent numerical study demonstrates that the simultaneous actuation of two different resonance modes can lead to a modified vortex pattern of the acoustic streaming, this let to decrease the size limit for which it is possible to focus [115]. Hoyo and Castro demonstrated that a pulsed actuation, instead of a steady one, decreased the magnitude of the acoustic streaming,

thus a lower F_{drag} [117]. Another study was focused on the introduction of inhomogeneous fluid in the chamber [75, 95, 96]. Despite the presence of inhomogeneity in the medium leads to a more complex experimental setup, it also suppresses the acoustic streaming (a more detailed explanation will be presented in [chapter 5](#)). One of the latest and pioneering studies was about the suppression of acoustic streaming based on a shape-optimized section [118].

4.2 Numerical model, boundary conditions and convergence analysis

An important result from literature came from Muller et al. [84]. In this study they observed, from a numerical point of view, that by increasing the aspect ratio of the cross-section, this last was not fully covered by the acoustic streaming vortices. This interesting aspect led us to think about a parametric study that could investigate the influence of the cross-sectional aspect ratio on the focusing of particles. We started changing the height of the channel, keeping constant the displacement of the actuated walls (the experimental voltage switching. In a more general case, when the properties of the piezoelectric material, as in the case of this model, are unknown a more meaningful value is the input power. For achieving 100 Pa energy density in a rectangular section of about 300 μm width and 150 μm height about 25-30 mW input power is needed, if the ideal mode is hit.) and the actuating frequency. This setup gave us different values of acoustic energy density for each aspect ratio. As second step we kept constant E_{ac} sweeping the displacement of the walls and keeping constant the actuating frequency at the value of the previous step. The following point was to find the resonance frequency values for all the aspect ratio and tune the displacement in order to have the same acoustic energy density in the systems. As last part of this study we chose to maintain constant the area of the section of the channel and repeat the same tests listed above. All these steps are summarized in [Table 4.1](#). The main purpose of this work was to analyse the enhancement of particle focusing by confining the acoustic streaming in a smaller region of the section without adopting an elaborate and complex strategy.

4.2.1 Numerical model

As described in [chapter 2](#), the first-order and second-order fields were derived using the perturbation theory. The corresponding continuity and the conservation of momentum equations for first-order field are [eq. 2.29](#) and [eq. 2.35](#), while for the second-order field are [eq. 2.38](#) and [eq. 2.39](#). An homogeneous, isotropic, newtonian and compressible liquid is considered and the unperturbed thermodynamic equilibrium state (zeroth order) corresponds to a temperature T_0 , density ρ_0 , pressure p_0 and quiescence $\mathbf{v}_0=0$. The adiabatic assumption was considered.

As mentioned above the 2D simplification was adopted, thus a rectangular cross-section

Constant	E_{ac}	f	l_0
W	Variable	1.9669 MHz	0.1 nm
W	106 Pa	1.9669 MHz	Variable
W	106 Pa	Resonance frequency	Variable
S	106 Pa	Variable	0.1 nm
S	106 Pa	Resonance frequency	Variable

Table 4.1: Summary of the structure of the present study, where W is the width of the channel and S is the cross-sectional area of the channel defined as $W \times H$. Adapted from [112].

filled with water was considered as control volume. The reference dimensions were $380 \mu\text{m}$ for the width and $160 \mu\text{m}$ for the height of the channel. This corresponded to an AR, defined as H/W , of 0.42. All the equations listed above were implemented in the weak form (for more information we remind the reader to subsection 2.3.1) in COMSOL Multiphysics (version 5.4, COMSOL Inc.). The particle trajectories were computed using the built-in module of Particle Tracing for Fluid Flow.

4.2.2 Boundary conditions

As denoted in the previous section one of the most influencing properties of the material is the acoustic impedance. In fact, in order to obtain an efficient standing wave inside the chamber a hard material is required (i.e. silicon/glass which has high Young's modulus). For this reason, we assume the top and the bottom walls as rigid. The actuation on the right and left walls was implemented adding a harmonically oscillating boundary condition on the first order velocity (as sketched in Fig. 4.2). For the 2nd order velocity a zero-mass flux through the right and left walls was set as boundary condition [114].

$$T = T_0 = 25^\circ\text{C} \text{ on all walls,} \quad (4.1)$$

$$\mathbf{v} = 0 \text{ on all walls,} \quad (4.2)$$

$$\mathbf{n} \cdot v_1 = v_{bc}(y, z)e^{-i\omega t} \text{ on the right/ left walls,} \quad (4.3)$$

$$\mathbf{n} \cdot v_2 = - \left\langle \frac{\rho_1(\mathbf{n} \cdot v_1)}{\rho_0} \right\rangle \text{ on the right/ left walls,} \quad (4.4)$$

where \mathbf{n} is the outward normal vector to the surface, $v_{bc} = \omega l_0$, with $l_0=0.1 \text{ nm}$ which is a representative displacement [84, 113] consistent with other numerical works [84,

114] and experiments [83]. For the pressure, a standard null flux condition was set at the walls. A Lagrange multiplier was needed to force the second-order pressure average to zero and obtain the convergence. The properties used both for water and polystyrene particles are listed in Table 4.2.

4.2.3 Mesh converge analysis

The rectangular section of the channel was divided in four subdomains shown in Fig.4.4. Three of them were considered as bulk domain and one as boundary domain near the walls. This was useful to structure the mesh. The bulk domain was set from $\frac{-W}{2} + w_{bd}$ to $\frac{W}{2} - w_{bd}$ where $w_{bd} = 10\delta_s$ and δ_s is the dimension of the viscous boundary layer for a frequency of 2 MHz, obtained from eq. 2.36. The central domain, coloured darker in Fig. 4.5, corresponded to the "focusing region" where we intensified our attention and it goes from $-\frac{W}{2} + 0.25W$ to $\frac{W}{2} - 0.25W$. In the bulk domains the maximum element size of the free quadrilateral mesh was set equal to w_{bd} , while the grid in the boundary mesh was divided in N elements. Since the greatest gradients are inside the boundary domain a convergence analysis varying N was performed. For doing that a relative convergence parameter $C(g)$ was monitored since it achieved a value lower than 1×10^{-3} , as shown in Fig. 4.4. $C(g)$ was estimated considering a general solution for the generic field g and a reference solution g_{ref} , obtained with the finest mesh, as follow:

$$C(g) = \frac{\sqrt{\int (g - g_{ref})^2 dydz}}{\sqrt{\int (g_{ref})^2 dydz}}. \quad (4.5)$$

The reference mesh was chosen with $N=20$, which correspond to an element inside the boundary domain equal to $0.5\delta_s$ (or $\delta_s/w=2$). As can be seen in Fig. 4.4, a value of $\delta_s/w=0.8$ guarantees the relative convergence parameter criteria. Setting this parameters the total number of mesh elements was approximately 6×10^3 .

4.2.4 Particle tracing

A special attention has to be given to the particle tracing computation. After the background fields were computed, we used the results to compute all the forces experienced by the particles. As expressed in 2 the total force exerted on a particle is the sum of the acoustic radiation force and the streaming-induced Stokes drag force. In this work we computed the acoustic radiation force F_{rad} using the equation obtained by Karlsen et al.[115, 90], as follow

$$F_{rad} = -\pi a^3 \left[\frac{2}{3} k_0 \langle C_{M1} \nabla p_1 \rangle - \rho_0 \langle C_D \mathbf{v}_1 \cdot \mathbf{v}_1 \rangle \right], \quad (4.6)$$

$$C_M = \frac{C_{M1} + C_{M2} H}{1 + C_{M3} H}, \quad (4.7)$$

Property	Symbol	Value
Water		
Density ¹	ρ_0	998 [kg m ³]
Speed of sound ¹	c_0	1497 [m s ⁻¹]
Shear viscosity ²	η_0	0.890[mPa s]
Bulk viscosity ³	η_B	2.485 [mPa s]
Specific heat capacity ¹	C_p	4181 [J(kg K) ⁻¹]
Heat capacity ratio ¹	Γ	1.011
Thermal conductivity ⁴	k_{th}	0.6065 [W(m K) ⁻¹]
Isentropic compressibility ⁵	k_0	448[TPa ⁻¹]
Thermal expansion coeff. ²	α_p	2.573×10^{-4} [K ⁻¹]
Polystyrene		
Density ⁸	ρ_{ps}	1050[kg/m ³]
Speed of sound	c_{ps}	2350[m s ⁻¹]
Compressibility	k_{ps}	249 [TPa ⁻¹]
Poisson's ratio ⁹	σ_{ps}	0.35
Heat capacity ¹⁰	$C_{p,ps}$	1220 [J(kg K ⁻¹)]
Heat capacity ratio ¹¹	γ_{ps}	1.04
Thermal expansion coeff. ¹¹	$\alpha_{p,ps}$	2.09×10^{-4} [K ⁻¹]
Thermal conductivity ¹²	$k_{th,ps}$	0.140 [W(m K) ⁻¹]
Isentropic compressibility ⁶	$k_{s,ps}$	238[TPa ⁻¹]
Speed of sound ⁶	$c_{s,ps}$	2350[m s ⁻¹]
Transverse speed of sound ⁷	$c_{t,ps}$	1068[m s ⁻¹]
¹ From polynomial fit from Ref. [114], based on data from Ref. [119]. ² From polynomial fit from Ref.[114], based on data from Ref. [120]. ³ From polynomial fit from Ref. [114], based on data from Ref. [121]. ⁴ From polynomial fit from Ref. [114], based on data from Ref. [122]. ⁵ From reference [101]. ⁶ From reference [115]. ⁷ From reference [115], taken from [90]. ⁸ From reference [84]. ⁹ From reference [115], taken from [123]. ¹⁰ From reference [115], taken from [124]. ¹¹ From reference [90]. ¹² From referencete [115], taken from [125].		

Table 4.2: Properties for water at T=25°C and polystyrene. Adapted from [112].

$$C_D = \frac{C_{D1}(1 - G)}{C_{D1} + 3(1 - G)}, \quad (4.8)$$

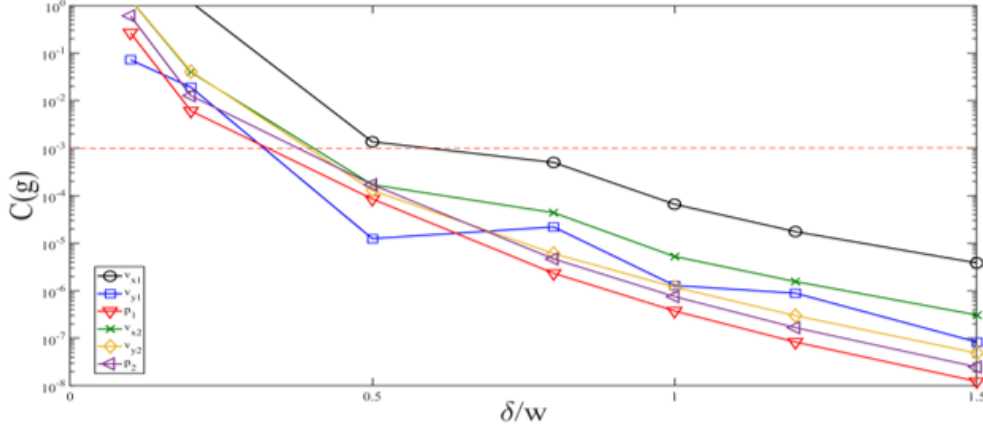


Figure 4.4: Mesh convergence analysis for different element sizes in the boundary domain. Reprinted from [112].

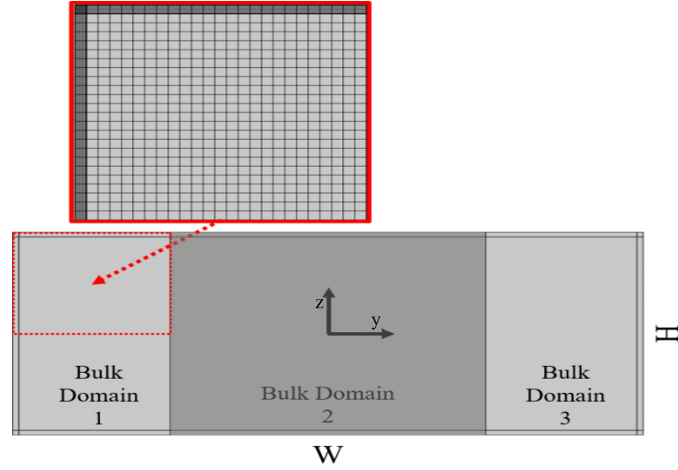


Figure 4.5: Schematic representation of the used rectangular cross section of the channel considered as reference system. The fluid domain was divided in 4 subdomains: 2 lateral bulk domains (lighter grey), 1 central bulk domain (darker grey) and a boundary domain close to the walls. A zoom of a squared zone defined with a red line is reported to show the mesh elements. Adapted from [112].

where a is the particle radius and C_M and C_D are the monopole and dipole scattering terms [115, 90], which come from a difference of properties between the suspended particle and the medium. The monopole scattering coefficient can be derived through these equations [115]:

$$C_{M1} = 1 - \tilde{k}_s, \quad (4.9)$$

$$C_{M2} = 3(\gamma - 1) \left[(1 - \xi)(1 - \chi\xi) - \frac{4}{3} \chi \tilde{\rho}_0 \xi \tilde{k}_s \left(\frac{c_{t,ps}}{c_0} \right)^2 \left(1 - \frac{\xi}{\tilde{k}_s} \right) \right], \quad (4.10)$$

$$C_{M3} = 4(\gamma - 1)\chi\tilde{\rho}_0\left(\xi\frac{c_{t,ps}}{c_s}\right)^2, \quad (4.11)$$

$$H(a, \omega) = \frac{1}{(k^T a)^2} \left[\frac{1}{1 - ik^T a} - \frac{1}{\tilde{k}_{th}} \frac{\tan(k_{ps}^T a)}{\tan(k_{ps}^T a) - k_{ps}^T a} \right]^{-1}, \quad (4.12)$$

where tilde indicates the ratio of particle property to fluid property, e.g. $\tilde{\rho}_0 = \rho_{ps}/\rho_0$, and with the following formulations:

$$\xi = \frac{\tilde{\alpha}_s}{\tilde{\rho}_0 \tilde{c}_p}, \quad \chi = 1 - \frac{4}{3} \left(\frac{c_{t,ps}}{c_{s,ps}} \right)^2, \quad (4.13)$$

$$k^T = \frac{1+i}{\delta_T} \left[1 + \frac{i}{2}(\gamma - 1)(\Gamma_s - \Gamma_T) \right], \quad (4.14)$$

$$k_{ps}^T = \frac{1+i}{\delta_{T,ps}} \frac{1}{\sqrt{1-X}} \left[1 + \frac{i}{8} \frac{\gamma_{ps}^2 \Gamma_{T,ps}}{1-X} \right], \quad X = (1 - \gamma_{ps})(1 - \chi), \quad (4.15)$$

$$\Gamma_s = \frac{1}{2} \left(\frac{\eta_B}{\eta_0} + \frac{4}{3} \right) \left(\omega \frac{\delta_s}{c_s} \right)^2, \quad \Gamma_T = \frac{1}{2} \left(\frac{\delta_s}{c_s} \right)^2, \quad \Gamma_{T,ps} = \frac{1}{2} \left(\frac{\delta_{T,ps} \omega}{c_{s,ps}} \right)^2, \quad (4.16)$$

$$\delta_T = \sqrt{\frac{2k_{th}}{\rho_0 C_p \omega}}, \quad \delta_{T,ps} = \sqrt{\frac{2k_{th,ps}}{\rho_{ps} C_{p,ps} \omega}}. \quad (4.17)$$

The dipole scattering coefficient, which includes viscous and thermal effects has the following sub coefficient and function:

$$C_{D1} = 2(\tilde{\rho}_0 - 1), \quad G(a, \omega) = \frac{3}{k^s a} \left(\frac{1}{k^s a} - i \right) \text{ and } k^s = \frac{1+i}{\delta_s} .s \quad (4.18)$$

The streaming induced drag force it is defined by eq. 2.18, thus the total force, neglecting gravity and buoyancy, acting on the particle can be written as

$$\frac{d(m\mathbf{v}_p)}{dt} = F_T = F_{rad} + F_{drag}, \quad (4.19)$$

where m is the mass of the particles and F_T is the sum of the forces acting on the particles. The left side term expresses the acceleration of the particle. If a micrometer-sized particle accelerated by the drag force is considered, the characteristic unsteady time can be approximated as $\tau_{unsteady} \approx \frac{2}{9} a^2 \frac{\rho_p}{\eta_0} \approx 1 \mu\text{s}$. On the other hand the characteristic steady time, considering a terminal velocity \mathbf{v}_p , is $\tau_{steady} \approx 1 \text{ ms}$, derived from $\mathbf{v}_p = \frac{F_{rad}}{6\pi\eta_0 a}$. Thus, the acceleration can be reasonably neglected.

Particles were released from a regular grid with an initial velocity equal to 0. The interaction between the particles were not considered. Mono-dispersed particles with

radius of 250 nm, 500 nm, 750 nm, 1 μm and 2 μm were studied. Since the number of particles, especially for small radius, influenced the results, some tests were performed using the most critical situation (i.e. AR of 0.42 and radius of 250 nm) in order to obtain the optimal concentration. As can be seen in Fig. 4.6, the fraction of particle collected in the central subdomain presented greater oscillation with a decreasing number of particles. An optimal number, derived from the study of the standard deviation of the fraction of particles collected, was found. Accordingly to Fig. 4.7, a spacing grid of 5 μm was chosen. It corresponds to a number of particles higher than 2000. We found that this concentration of particles was compatible with the assumption of neglecting hydrodynamic interaction between micron-sized particles [116].

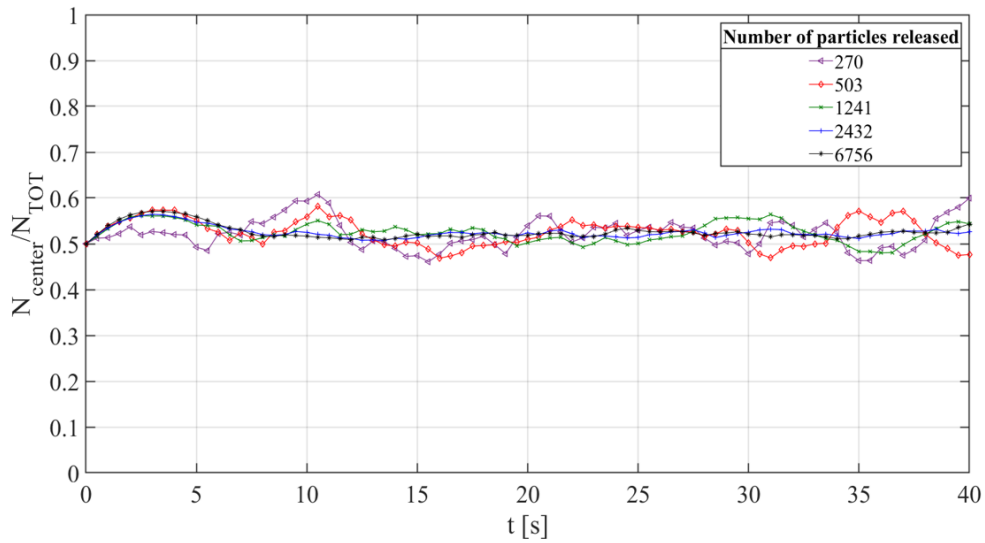


Figure 4.6: Fraction of the particles collected in the central subdomain as function of time for 0.42 AR and radius a of 250 nm. The number of particles used goes from 270 to 6756. Reprinted from [112].

4.3 Validation of 2D model

As said above, the effect of the acoustic radiation force and the drag force are mainly across the cross-section and the 2D assumption is reasonable. Since a flowrate has to be applied to collect the particles in the outlet, in reality there is also a velocity component in the x direction. For investigating the effect of this component on the fraction of the particles collected in the central domain, a 3D study for an aspect ratio of 0.42 was performed. Full 3D numerical models which also solves the phenomena inside the viscous boundary layer have heavy computational demand. For this reason Lei et al. [126, 127] developed a lighter 3D model that uses the limiting velocity theory, which was firstly described by Nyborg in 1958 [128]. This method permits to predict

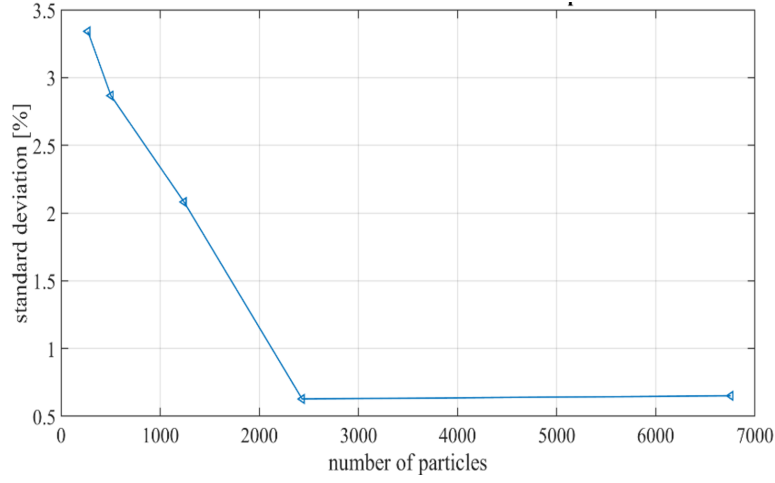


Figure 4.7: Standard deviation of fraction of particles collected in the central subdomain. Reprinted from [112].

analytically the streaming velocity field outside the boundary layer and thus compute only the Rayleigh streaming (for further information we remind the reader to [chapter 2](#)). This means that the mesh inside the boundary subdomain is not needed and it highly reduces the computational effort. The limiting velocity finite element method was used to investigate the influence of the flow rate on the focusing results and to validate the developed 2D model.

4.3.1 3D numerical model

The first-order acoustic fields in this case were simulated using the built-in module in COMSOL called "Pressure Acoustics". With this interface it is possible to solve the harmonic linearised equation, which takes the form

$$\nabla^2 p_1 = -\left(\frac{\omega}{c_0}\right)^2 p_1. \quad (4.20)$$

In this case the actuation was simulated imposing a displacement l_0 at the side walls. With the first-order fields obtained it was possible to compute the limiting velocity equations [127]:

$$u_L = -\frac{1}{4\omega} \text{Re} \left\{ q_x + u_1^* \left[(2+i) \left(\frac{du_1}{dx} + \frac{dv_1}{dy} + \frac{dw_1}{dz} \right) - (2+3i) \frac{dw_1}{dz} \right] \right\}, \quad (4.21)$$

$$v_L = -\frac{1}{4\omega} \text{Re} \left\{ q_y + u_1^* \left[(2+i) \left(\frac{du_1}{dx} + \frac{dv_1}{dy} + \frac{dw_1}{dz} \right) - (2+3i) \frac{dw_1}{dz} \right] \right\}, \quad (4.22)$$

$$q_x = u_1 \frac{du_1^*}{dx} + v_1 \frac{du_1^*}{dy}, \quad (4.23)$$

$$q_y = u_1 \frac{dv_1^*}{dx} + v_1 \frac{du_1^*}{dy}, \quad (4.24)$$

where u_1, v_1, w_1 are the x,y,z first-order velocity components, u_L and v_L are the two limiting velocity components and * denotes the conjugate value. u_L and v_L were added as boundary conditions on the top and bottom walls to compute the second-order fields. The common no-slip condition was used at the right and left walls. For both the inlet ($x=0$) and the outlet ($x=L$) a pressure outlet condition was imposed. A predefined COMSOL's "Creeping Flow" physic was used to solve the 2nd order fields. Considering a Stokes flow the equations that needed to be solved were:

$$\nabla p_2 = \mu \nabla^2 \mathbf{v}_2, \quad (4.25)$$

$$\nabla \cdot \mathbf{v}_2 = 0. \quad (4.26)$$

Also for this validation the "Particle Tracing for Fluid Flow" physic was used to compute the particle trajectories. As in the main part of the work, the position of the particles was computed considering the sum of the total forces acting on them (eq. 4.19).

4.3.2 Geometry and mesh

We chose to compare the 3D model with the reference geometry of the main study, thus a width of 380 μm and height of 160 μm and a length L of 2 cm were set. A tetrahedral mesh was used with an element size of 50 μm . This choice was taken considering that 8-10 elements within the wavelength are enough to compute both the first and second order fields [127]. A representation of the full mesh obtained is shown in Fig. 4.8.

4.3.3 Comparison

Before computing the particle trajectories, we chose to compare the fields between the 2D and 3D models. First, we analysed the amplitude of both the first-order pressure field and streaming field (Fig. 4.9 (a-b-c-d)). As can be noticed, there is no appreciable difference on the macroscopic morphology of the fields and neither in the magnitude. The results from the 3D model were obtained considering an actuation frequency of 1.9678 MHz needed to have an acoustic energy density of 106 Pa (for the same E_{ac} in the 2D model a frequency of 1.9669 MHz was needed). This small difference between the two models could be due by the higher viscous damping inside a 3D system, which slightly shift the frequency value. A 3D overview of the obtained pressure field is shown in Fig. 4.9(e). The second step of validation consisted in the comparison of the fraction of particles concentrated in the central subdomain. So the following values of radius were used: 250 nm, 500 nm, 750 nm, 1 μm and 2 μm . The results obtained were compared and a deviation was calculated, as reported in Table 4.3. From these values can be noticed that the difference of results between the two models is neglectable and thus the particles behaviour is not influenced by the flowrate.

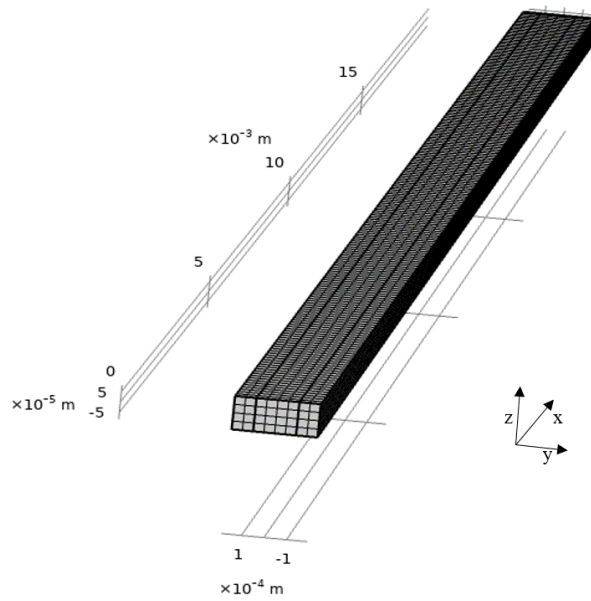


Figure 4.8: Full representation of the tetrahedral mesh used for the 3D model. Reprinted from [112].

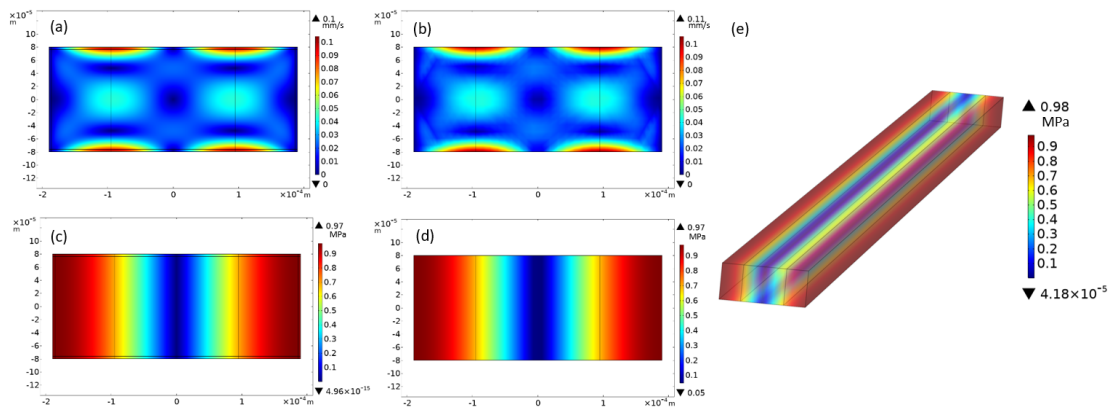


Figure 4.9: Comparison of the first order pressure field between the 2D model (a) and 3D model (b). Second order velocity obtained with (c) 2D model and (d) 3D model. (e) 3D plot of p_1 . Reprinted from [112].

4.4 Results

After a validation step of the 2D assumption, we chose to investigate different geometric parameters covering several experimental conditions, as shown in Table 4.1. We started

Radius	$N_{center}/N_{sides}^{2D}$	$N_{center}/N_{sides}^{3D}$	Deviation between the two models [%]
2 μm	1	1	0
1 μm	0.86	0.82	4.6
750 nm	0.55	0.52	5.5
500 nm	0.52	0.5	3.8
250 nm	0.52	0.5	3.8

Table 4.3: Comparison of the fraction of particles collected in the central subdomain between the 2D and 3D model. Adapted from [112].

considering a constant width of the channel, thus the aspect ratio was varied increasing the height. In a second step the cross-section was kept fixed and W and H were changed in order to obtain the same previous AR values (i.e. 0.42, 1, 1.2, 1.5 and 2).

4.4.1 Constant channel width

E_{ac} variable, constant f and l_0

In this first section of the study, the width W was kept constant at 380 μm and the height changed in order to obtain 5 different values of aspect ratio: 0.42, 1, 1.2, 1.5 and 2. As expected, and predicted briefly by Muller et al. [84], the acoustic streaming pattern changed as function of the AR , as shown in Fig. 4.10(a). As can be seen, distancing the top and bottom walls, a "free zone" is created. The influence of the boundary walls is localized, and it leads to the presence of a portion where the acoustic radiation force is the major force acting on the particles. If a frequency of 1.9669 MHz is chosen to actuate the chamber, which is the resonance frequency of the smaller channel, the acoustic energy density of the other systems will change. We found that E_{ac} presented a maximum for a squared cross-section and it decreased with increasing aspect ratios. Analysing eq. 2.43 it is possible to derive some conclusion about this particular trend. E_{ac} is calculated over the volume of the chamber, this means that an higher cross-section lead to a lower acoustic energy density. Moreover, increasing the height of the actuated walls, a greater mechanical energy is transferred in the fluid volume leading to an higher acoustic energy density respect to 0.42 of AR . Observing the fraction of particles collected in the central subdomain we found that the value oscillate after few seconds, this effect was enhanced for lower AR . This phenomenon can be explained considering two different time ranges. At the beginning the particles are moved forward the centre experiencing the radiation force. When they reach the node of the standing wave, they are pushed at the ceiling and the bottom by the vertical component of the drag force. After that they start to follow the acoustic streaming vortexes and rotate leading to an

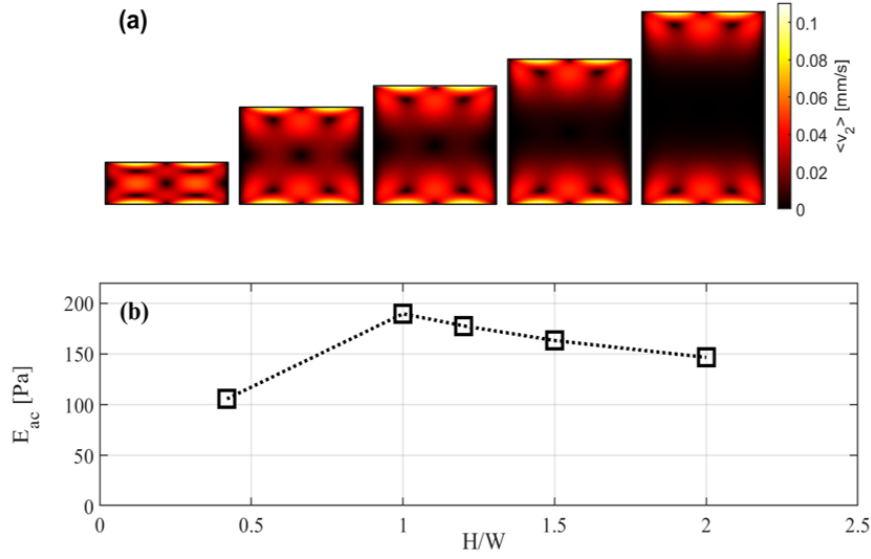


Figure 4.10: (a) Contour plots of acoustic streaming in different aspect ratio (0.42, 1, 1.2, 1.5 and 2 from left to right). (b) Acoustic energy density as function of the aspect ratio with an actuation frequency of 1.9669 MHz and a constant l_0 . Adapted from [112]

oscillating fraction collected in the central domain over time. An optimal time had to be chosen. This was selected considering a transient simulation for an aspect ratio of 0.42 and with particles radius of 250 nm. Therefore, analysing data shown in Fig. 4.11, we opted to consider results for the first 16 seconds when the higher performance condition of focusing was found. This correspond to the instant when the last value of the fraction of particle collected in the central sub-domain has reached a plateau. It is important to underline that this result is not achieved for the smaller AR value, where the acoustic streaming is still influencing all the cross-section, as well as the particles focusing. Merging all the results obtained for different particles radius, Fig. 4.12 was obtained. A light increasing of the focusing efficiency was noticed for all the particle sizes. The higher enhancement was obtained for sub-micrometer particles, for which the focusing fractions changed by 15-20%. For what concern particles with radius of 2 μm , represented by a purple line in Fig. 4.12, F_{rad} is totally dominant with respect to the streaming-induced drag force and the particles are all maintained at the pressure node.

E_{ac} constant, constant f and l_0 variable

In this case the acoustic energy density was kept constant through a sweeping of the walls displacement. The target value of E_{ac} was 106 Pa, obtained for a resonance frequency of 1.9669 MHz in the channel with 0.42 aspect ratio. The fraction of particles

collected in the central subdomain, as performed above, was calculated considering the number of particles in the central region over all the particles released at time $t=0$. Results are shown in Fig. 4.13(a). Comparing these data with the previous condition, the increasing in efficiency of focusing is less marked. An higher fraction was recorded for particle radius equal to 500 nm with increased AR and particles with 750 nm of radius presented a better focusing also for low aspect ratios.

E_{ac} constant, resonance f and l_0 variable

In order to obtain the optimal energy density inside the system, the choice of the correct frequency and voltage is necessary. To investigate the influence of the condition of resonance on the results, we performed the same study as in the sub-section above, but with the frequency at resonance values for each aspect ratio. In Fig. 4.13(b) an overview of the obtained results with this condition is reported. As can be seen, there are not evident differences between the results in Fig. 4.13(a) and Fig. 4.13(b). Therefore, it is possible to conclude that the resonance condition is not essential (even if it is experimentally convenient exploit this favourable energy condition), if the voltage is tuned to have two systems with the same acoustic energy density. One thing has to be highlighted. This assumption is admissible and true when the temperature is controlled, and the needed voltage is not too high. In fact, in reality, high voltage effects in the piezoceramic transducer leads to a fast heating of the device and of the fluid. This changes both the properties of the fluid and the response of the system to the actuation, thus the results could be not comparable with the ones presented.

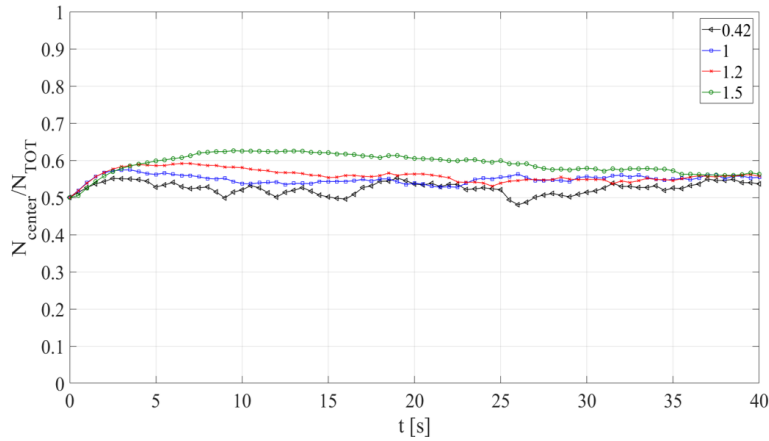


Figure 4.11: Fraction of particles collected in the central subdomain over time for particles with 250 nm radius. Adapted from [112]

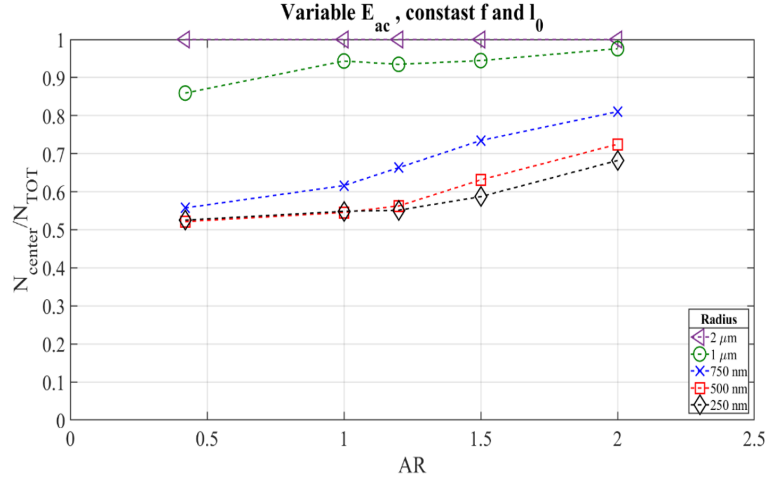


Figure 4.12: Fraction of particles collected in the central subdomain as function of their radius. Reprinted from [112]

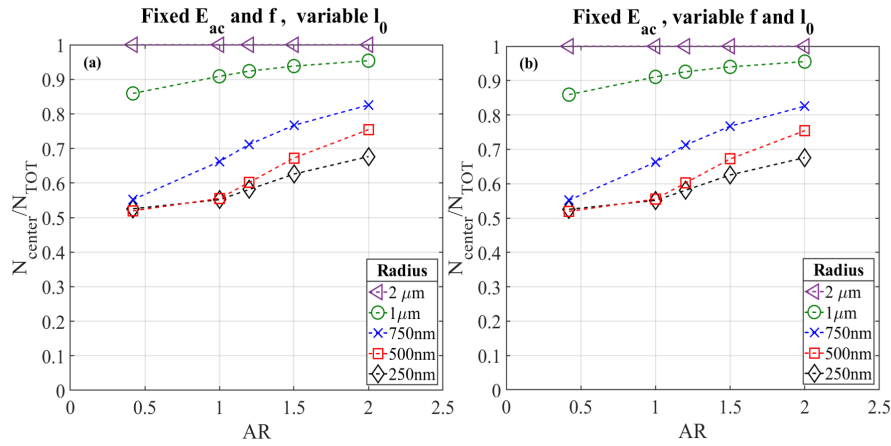


Figure 4.13: Fraction of particles collected in the central subdomain as function of their radius with a constant width of the channel. In this case the acoustic energy density was kept constant at 106 Pa and the walls displacement variable. (a) f was kept constant to 1.9669 MHz, the resonance frequency of the channel with 0.42 AR. (b) f was changed for each aspect ratio to the respective resonance value and the displacement was tuned to obtain the same E_{ac} for all AR. Reprinted from [112]

4.4.2 Constant cross-sectional area

We chose to maintain constant the area of the cross-section at $60800 \mu\text{m}^2$ (corresponding to the aspect ratio with width of $380 \mu\text{m}$ and height of $160 \mu\text{m}$). The same tests performed in the previous section have been repeated with these conditions.

E_{ac} constant, variable f and l_0 constant

Even in this case, to guarantee a constant acoustic energy density, maintaining the same displacement, the frequency had to be swept until E_{ac} was around 106 Pa. The values of width and height for each aspect ratio and the corresponding used frequency are reported in Table 4.4. All the results collected with these conditions are reported in Fig. 4.14(a). The fraction of particles focused on the central subdomain did not change significantly for a radius equal to 250 and 500 nm, respect to the previous conditions. On the other hand, for size equal and greater than 750 nm of radius, the focusing efficiency increased remarkably, reaching almost the 100% of particles in the central subdomain. The decreasing of the width, for higher value of AR, corresponded to smaller mean path

H [μm]	W [μm]	f_{res} [MHz]	AR
247	247	3.0226	1
270	225	3.3177	1.2
302	201	3.7132	1.5
349	174	4.2881	2

Table 4.4: Summary of the height and the width for each aspect ratio value and the corresponding resonance frequency and wall displacement. Adapted from [112].

that particles have to do to move forward the central channel position. Particles with a radius of 1 μm , as can be seen in Fig. 4.14(a) were focused already for aspect ratio equal to 1. This is an interesting improvement in focusing respect to the tests described above, in which the same particles could be collected only for 90%.

E_{ac} constant, resonance f and l_0 variable

The last case of study involved the study of the resonance condition, keeping constant the acoustic energy density at 106 Pa. All the values of frequency and walls displacement are reported in Table 4.5. The obtained results are plotted in Fig. 4.14(b). As can be seen, the data reported are very close to the one shown in the previous subsection. Even in this case, for smaller particles there was not a clear improvement, while for particles with radius equal and greater to 750 nm the increasing in efficiency was significant. Considering these last results, it is possible to say that the parameters which mostly enhanced the performance of concentration efficiency were the cross-section and the acoustic energy density. Moreover, the increasing of the aspect ratio had clearly a positive influence in focusing, also with particles of smaller radius. If Fig.4.13 and Fig. 4.14 are compared, it can be noticed that particles with radius greater than 500 nm can be collected near to 100% in the central subdomain with an AR of 1.2, or greater. On the

H [μm]	W [μm]	f [MHz]	AR	l_0 [m]
247	247	3.028	1	$3.460e^{-11}$
270	225	3.324	1.2	$2.780e^{-11}$
302	201	3.721	1.5	$2.170e^{-11}$
349	174	4.299	2	$1.514e^{-11}$

Table 4.5: Summary of the height and the width for each aspect ratio value and the corresponding applied frequency. Adapted from [112].

other hand, for sub-micrometer particles, a good fraction (maximum 80%) could be collected only with an aspect ratio of 2. These results highly underline the importance of the presence of a "free zone", where the acoustic streaming does not influence the fluid motion, thus the particles are moved only by the acoustic radiation force and they can be focused also with smaller radius.

4.5 Conclusions

A numerical parametric study was performed to investigate the effect of the aspect ratio of the cross-section of a microfluidic device on the acoustophoretic particles focusing. The increasing in aspect ratio presented a streaming-free zone which allows the acoustic radiation force to be dominant. Different values of aspect ratio in a range from 0 to 2 were investigated and the particles focusing with diameter from 500 nm to 4 μm was studied. Two different approaches were used for this study. The former was the investigation of the particles behaviour keeping constant the width of the channel, thus changing just the height. In the second approach, the aspect ratio was changed keeping constant the cross-section area. In both the conditions we showed that a higher aspect ratio enhance the capability of focusing particles also for sub-micrometer particles. From the exposed result the more efficient focusing was achieved with an AR of 2 with a height of 349 μm and width of 179 μm . For all the particles sizes, in fact, the percentage collected in the central subdomain was above the 70% when sub-micrometer particles were considered and 100% for micrometer ones. Any experimental tests were presented in this chapter; thus a validation could be certainly one of the possible further step of the study. An interesting future investigation could involve the usage of biological cells, such as white blood cells, platelets, or red blood cells. Different improvement to the model could be implement, for example particles interactions or the drag force correction close to the walls. Future work should concentrate also in the usage of different suspending medium to verify if this parameter could further improve the particle focusing efficiency. Another important factor that was not considered in

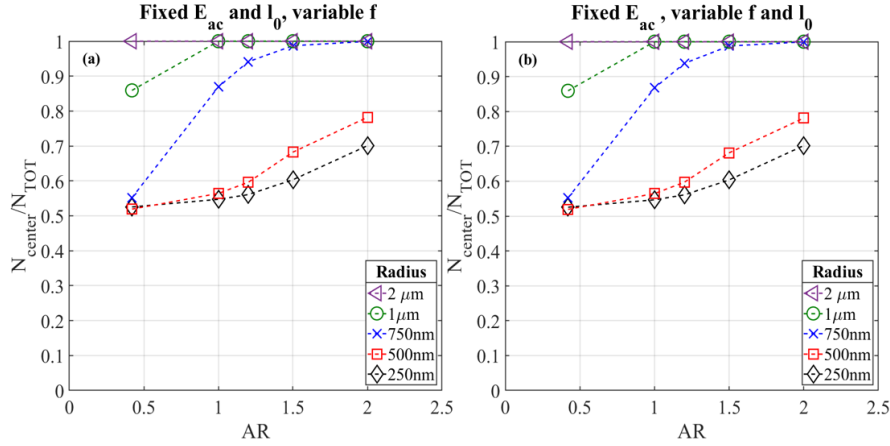


Figure 4.14: Fraction of particles collected in the central subdomain as function of their radius with a constant cross-sectional area. In this case the acoustic energy density was kept constant at 106 Pa and the walls displacement variable. (a) f was kept constant to 1.9669 MHz, the resonance frequency of the channel with 0.42 AR. (b) f was changed for each aspect ratio to the respective resonance value and the displacement was tuned to obtain the same E_{ac} for all AR. Reprinted from [112].

this study was the presence of the secondary acoustic body force. This comes in place when two (or more) particles suspended in a fluid, where a standing acoustic wave is present, are in close proximity to each other and lead to attractive and repulsive forces. This phenomenon has been widely studied theoretically and experimentally for bubbles, but there are fewer studies focusing on the interaction between solid particles/cells in acoustophoresis [129]. What should be expected if this force is introduced in the model is that as the interaction between particles come in place, aggregation could occur. The efficiency of focusing, thus should increase also for radius smaller than $1 \mu\text{m}$. In this study this aspect was neglected but for sure, mainly when the concentration of particles is high, the introduction of the secondary acoustic body force in the model could have a high impact on the model quality and predict a more realistic particles behaviour. Another aspect that should be investigated in the future, is the resonance on the vertical direction (in particular for aspect ratios equal to 1 and 2). For considering this effect, a full model also including the solid part of the device is needed, so that the wall vibration and the resulting streaming can be shown numerically. In this case the model only considers the fluid domain, so the exact condition of wall vibration (particularly for the top and the bottom walls) is unknown and cannot be solved analytically. Since this study was a former investigation of the effect of the aspect ratio on the particles focusing on presence of acoustic streaming, there are certainly several ways to improve the model in the future.

Chapter 5

Acoustofluidics in inhomogeneous medium

The last part of this PhD project involves a collaboration with Lund University, with Per Augustsson's group in the Biomedical Department. This collaboration aimed to investigate the possibility of separating sub-micrometer particles using inhomogeneous fluids. In this section an overview of the principles behind this idea is firstly reported. The validation of the proposed model is described, and it is followed by the main obtained results. This work has led to interesting conclusions, paving the way to further investigations regarding inhomogeneous acoustofluidics for particles separation.

5.1 Acoustic streaming suppression in inhomogeneous fluid

As expressed in different sections of the thesis, acoustic streaming is the steady flow in a viscous fluid driven by the absorption of acoustic waves. In an homogeneous fluid, inside confined space not much larger than the wavelength, the divergence in nonlinear momentum-flux-density tensor is caused by an acoustic energy dissipation mechanism [75]. This is localized inside the boundary layers δ_s where the velocity gradient is high in order to match the no-slip condition at the solid-liquid interface. Recent studies on acoustic fluid dynamics demonstrated that an inhomogeneity in density and compressibility, induced by a solute concentration profile, can be stabilized [96] or relocated into a more stable configuration [60, 97]. Recently Karlsen et al. [96, 130] described that in presence of inhomogeneity an acoustic force density \mathbf{f}_{ac} (eq. 2.50), generated by fast-time-scale acoustic field, act on the fluid leading to the above mentioned stabilization/relocation. In a more recent study [75], it was theoretically and experimentally demonstrated that this kind of inhomogeneity suppress the acoustic streaming. In this work a flow of pure water (lighter fluid) and a solution with 20% iodixanol (denser fluid) were laminated to form a concentration profile with the denser fluid at the centre, as

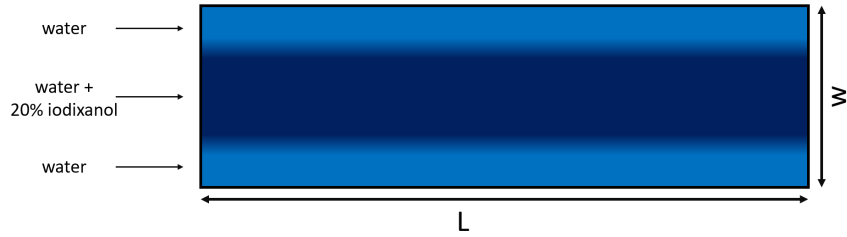


Figure 5.1: Sketch of the concentration profile with three inlet. The higher density fluid (dark blue) is an aqueous iodixanol solution. The lighter fluid is distilled water (light blue).

sketched in Fig. 5.1. This study was conducted in stop-flow condition, thus there was not flow rate. It is shown that the inhomogeneity induced acoustic body force counter acted the advection and diffusion. Despite of that, after a certain time, these last transport mechanisms overcame the force, and the concentration profile was not maintained. Looking at the streaming behaviour, this phenomenon describes a "time-window" when the vortexes are suppressed in the bulk, until the diffusion occurs and the fluid returns a homogeneous solution, leading to the common Rayleigh streaming pattern. The time evolution of the acoustic streaming is reported in Fig. 5.2. Lately Qiu et al. [95] experimentally characterized the acoustic streaming in fluid with gradient of density and compressibility. One of the main results that come from this study is that the transition from a stabilized inhomogeneity to an homogeneous configuration is function of the solute concentration. This indicates that the concentration profile evolution is dominated by diffusion transport in early times (the acoustic streaming is suppressed in the bulk). When the inhomogeneity starts to become weaker and the streaming rolls have

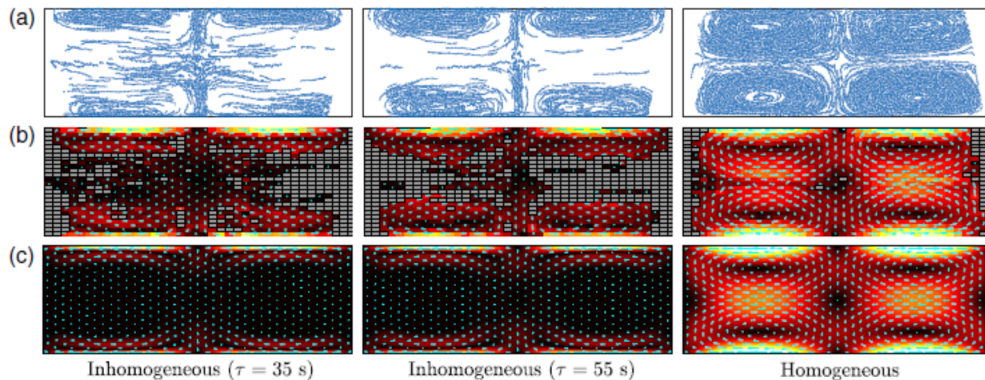


Figure 5.2: Acoustic streaming in a stabilized inhomogeneous fluid in stop flow at different time steps: 35 s (column 1), 55 s (column 2) and after total diffusion (column 3). Experimental particle positions (row a). Gray squares are spatial bins in experimental results (row b). Simulated acoustic streaming (row c). Reprinted from [75].

grown, the advection effect starts to become dominant and help the diffusion in the mixing process. This time evolution is also influenced by the type of molecule used as solute. Thus, the duration and the evolution of the inhomogeneity can be controlled by selecting correct gradients and thus suppressing the acoustic streaming for a sufficient time. Thus, higher will be the impedance difference created by the gradient, the acoustic streaming will be more suppressed. If this happens for enough time, particles would be moved only by acoustic radiation force and thus also sub-micrometer particles could be separated.

5.2 Sub-micrometer particles separation with fluid relocation

Our interest in inhomogeneity induced suppression of acoustic streaming had grown thanks to a recent study by Gautam et al. [131]. In this case the previously investigated acoustic fluid relocation [97, 130] was used to separate sub-micrometer particles. The main principle behind this approach is to have the lateral side of the channel filled by fluid with higher acoustic impedance respect to the central one. If the ultrasound is turned on the denser fluid will relocate to the centre of the channel, while the low-impedance fluid relocates to the sides pushed by the acoustic body force \mathbf{f}_{ac} . When a mixture of micrometer particles (diameter $> 1 \mu\text{m}$) and sub-micrometer particles (diameter $< 1 \mu\text{m}$) are suspended in the low-impedance fluid and injected in the central inlet, micrometer particles will be moved by the acoustic radiation force forward the pressure node of the standing wave, while sub-micrometer particles will follow the relocation of the less dense fluid moved by the drag force to the sides of the channel. The most interesting result obtained from this study is the possibility of separating a mixture of particles with $0.250 \mu\text{m}$ and $2.07 \mu\text{m}$ of diameter. The initial mixture in the central stream contained 52% of nanoparticles and 40 % of micrometer particles. After the relocation, the central outlet counted 81% of particles with $2.07 \mu\text{m}$ of diameter and only 9% of sub-micrometer particles. This result was very interesting for us and we chose to investigate more this effect, for a future outlook to the separation of nanovesicles (i.e. exosomes). Moreover, in the study a saline solution of NaCl and water was used, thus our task was also to investigate the usage of more cell-friendly molecule such as iodixanol or Ficoll.

5.3 Shifting in acoustic resonance for different configurations

As reported in the previous chapters, resonance is the condition necessary to maximize the mechanical energy transmitted by the piezoelectric actuator and thus acoustic energy density inside the fluidic chamber. An important result came from the numerical

study of the resonance in inhomogeneous systems.

As first point, a channel with a width of $375 \mu\text{m}$ filled with water was considered, thus the resonance frequency for an half-wavelength standing wave is calculated analytically by:

$$2W = \frac{c_0}{f} = \lambda. \quad (5.1)$$

Thus considering the speed of sound in water ($c_0 = 1507 \text{ m/s}$), it is possible to find a resonance frequency $f_{res} = 2.009 \text{ MHz}$. The same can be done if the chamber is filled by iodixanol solution, which properties as function of the concentration are reported in Fig. 5.3.

As can be seen, an aqueous solution of iodixanol slightly shift from the water properties. So, if we consider a 10% homogeneous iodixanol solution, the speed of sound will be 1505 m/s . Almost the same resonance frequency is obviously analytically obtained. This kind of calculation is easy when a homogeneous fluid is considered, but it become harder when an inhomogeneity is introduced. We chose to numerical study the resonance frequency of the two "inhomogeneity starting configurations" (i.e. stabilized and relocation as shown in Fig. 5.4). The expected behaviour of the acoustic energy density for the inhomogeneous systems was that the resonance fell between the two values of the homogeneous water and homogeneous 10% iodixanol. The numerical results showed an unexpected outcome. As shown in Fig. 5.5, the resonance shift outside the two "boundary" values depends on the starting position of the higher impedance fluid. In fact if the denser fluid is placed at the centre (i.e. stabilized configuration, Fig.5.4(a)), the resonance frequency is moved to lower value. On the other hand, if the starting configuration is with higher impedance fluid at the side (Fig. 5.4), the system presents a resonance frequency greater than a chamber filled with only water. It has to be noticed that the resonance values, also for the homogeneous systems, are lightly shifted respect to the analytical values obtainable with eq. 5.1, this is probably caused by a viscous damping effect [114]. This phenomenon is an important result that need to be further investigated. The dependency of the resonance on the initial position of the higher density fluid can generate different scenario with unexpected acoustic energy density values. It is important to underline that the observed effect it is appreciable only through analytical/numerical tests. In other words, it is possible to notice this slightly shift because the quality factor [114] in numerical simulation is very high, corresponding to a very narrow acoustic energy pick, which is hard to obtain with experimental devices. This difference lies on the absence of damping and mechanical coupling of the solid material in the presented numerical simulations, which lead to a lower quality factor.

5.3.1 Inhomogeneous model

We decided to proceed to the validation of the 2D model for inhomogeneous fluids used both in the stabilized and relocation phenomena, through a numerical comparison of

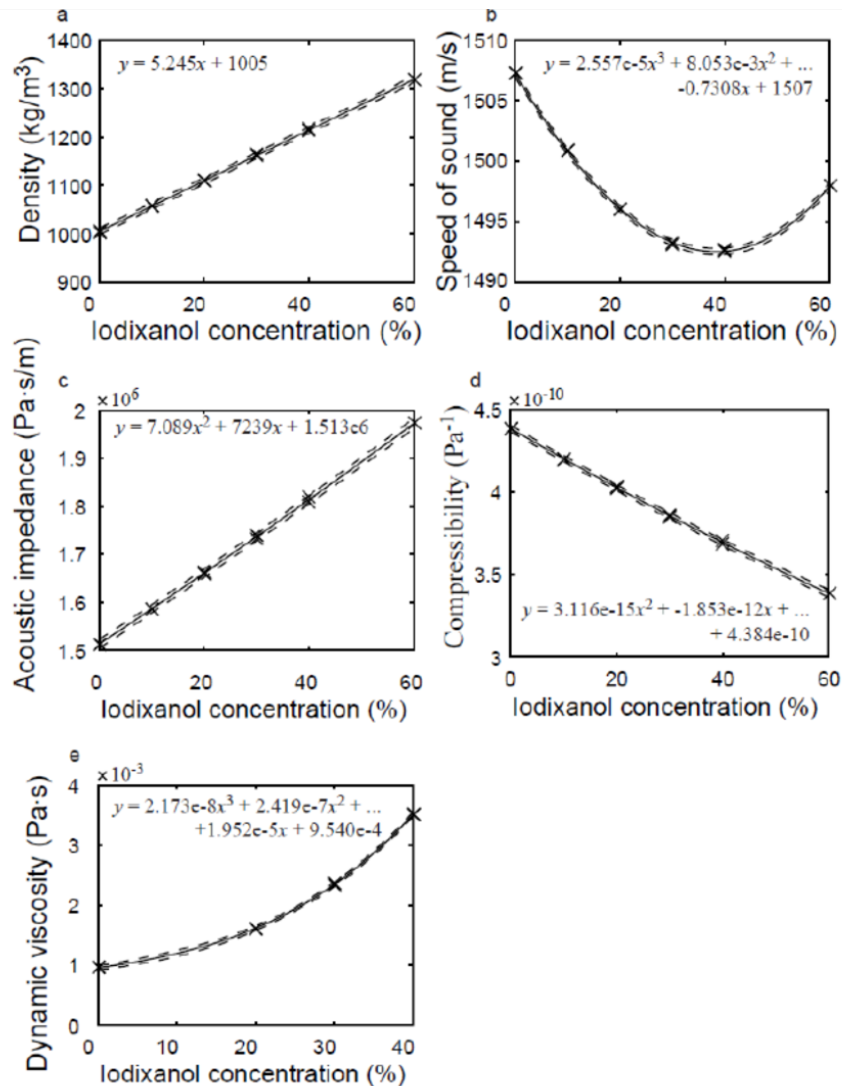


Figure 5.3: Properties Aqueous solution with iodixanol as function of concentration. Reprinted from [60].

the first and second order fields obtained with the model proposed for homogeneous fluids in chapter 4. We chose than to use both the reference and proposed models with two different fluids: homogeneous water and homogeneous solution with %5 iodixanol.

Numerical model

Since the numerical model for homogeneous fluids is the same reported in chapter 4, we refer the reader to this. On the other hand, it is important to underline the different approach for the inhomogeneous model. As proposed by Karlsen et al. [74, 75, 95, 96, 130]

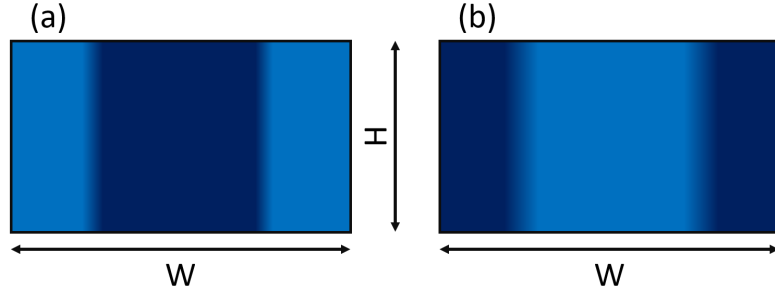


Figure 5.4: Sketch of starting fluid streams for (a) stabilized and (b) relocation.

a acoustics problem with inhomogeneous fluid has to be decomposed in two timescale: the faster one referred to the propagation of the wave, which happens in the order of $1/f$ ($\approx \mu\text{s}$), and the slow hydrodynamic timescale which describes the advection-diffusion transport in the order of ms. A segregated transient solver in COMSOL Multiphysics was used to solve the problem in two steps: First, the acoustic fields were computed in order to obtain the acoustic body force which appears in the slow-time-scale problem. Secondly, the hydrodynamic is solved using a generalized alpha solver with a maximum time step of 7.5 ms, keeping the acoustic energy density constant. The fast-time-scale acoustics is described by the following equations:

$$-i\omega\rho_0\mathbf{v}_1 = \nabla \cdot \boldsymbol{\sigma}_1, \quad (5.2)$$

$$-i\omega k_0 p_1 = -\nabla \cdot \mathbf{v}_1, \quad (5.3)$$

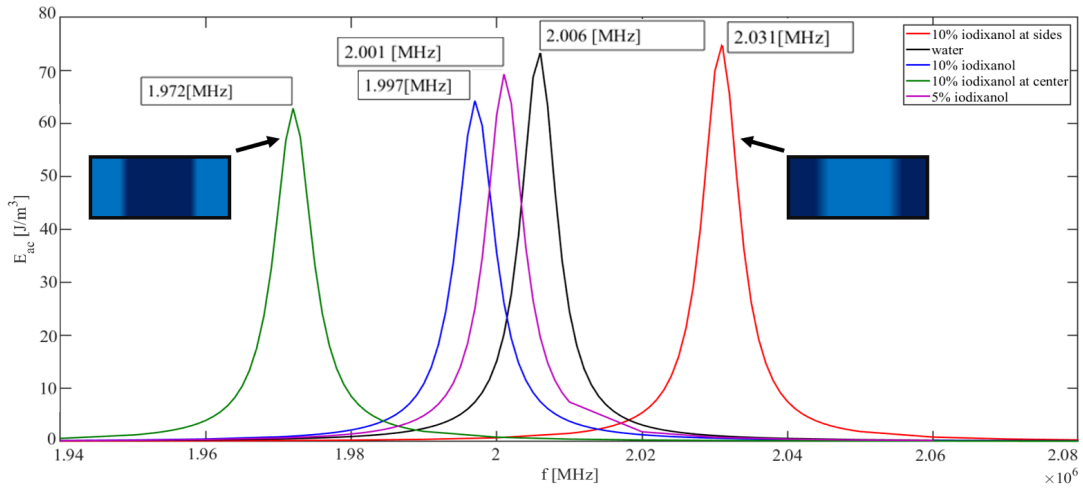


Figure 5.5: Acoustic energy density as function of frequency for different starting conditions.

$$-i\omega\rho_0k_0p_1 = -i\omega\rho_1 + \mathbf{v}_1 \cdot \nabla\rho_0, \quad (5.4)$$

The dynamics on the slow time scale is governed by mass-continuity and momentum-continuity equations for the fluid velocity and pressure which are now function of space and time, and by the advection-diffusion equation for the concentration field of the solute with diffusivity D [96],

$$\partial_t(\rho_0\mathbf{v}) = \nabla \cdot [\boldsymbol{\sigma} - \rho_0\mathbf{v}\mathbf{v}] + \mathbf{f}_{ac} + \rho_0\mathbf{g}, \quad (5.5)$$

$$\partial_t\rho_0 = -\nabla \cdot (\rho_0\mathbf{v}), \quad (5.6)$$

$$\partial_t s = -\nabla \cdot [-D\nabla s + \mathbf{v}s]. \quad (5.7)$$

Here, \mathbf{g} is the gravity acceleration, \mathbf{f}_{ac} is the acoustic body force, $\mathbf{v}(\mathbf{r}, t)$ and $p(\mathbf{r}, t)$ and $s(\mathbf{r}, t)$ are the space-time dependent velocity, pressure and concentration field respectively. It is important to underline, as exposed in [chapter 2](#), that the density, compressibility, and viscosity (and consequently the speed of sound and the acoustic impedance) cannot be considered as constant, but dependent on the concentration field, thus space-time-dependent.

Since the effects inside the boundary layer play an important role in the evolution of the concentration field, the same mesh adopted in [chapter 4](#) was used, thus the convergence analysis was not needed.

Comparison and validation

As mentioned above, we performed a comparison of two different homogeneous fluid with two models. We chose to analyse the acoustic streaming velocity and the first order velocity, as shown in left and right column in [Fig. 5.6](#) respectively. We denoted the one proposed by Muller et al. [84] as "homogeneous model" and the one described in the previous sub-section as "inhomogeneous model". We plotted the acoustic streaming measured along the blue line ([Fig.5.6\(a\)](#)) while the 1st order velocity was measured at the mid-height of the channel (black line in row (a)). In [Fig. 5.6](#) row (b) the comparison for a chamber filled with water is shown. The dashed black line represents the results obtained with the homogeneous model; the red continuous line is for inhomogeneous model data. The same colour-code is used to represent the data obtained with a chamber filled with 5% iodixanol (In [Fig. 5.6](#) row (c)). As can be seen, the results from the two models matched perfectly, thus we considered the model for inhomogeneous fluid validated.

5.4 Pseudo 3D model

Experiments for the separation of nanoparticles involve an imposed flow rate to collect the samples through the outlets. Thus, these are continuous systems dependent on the applied flow rates. On the other hand the 2D model proposed by Karlsen et al. [74,

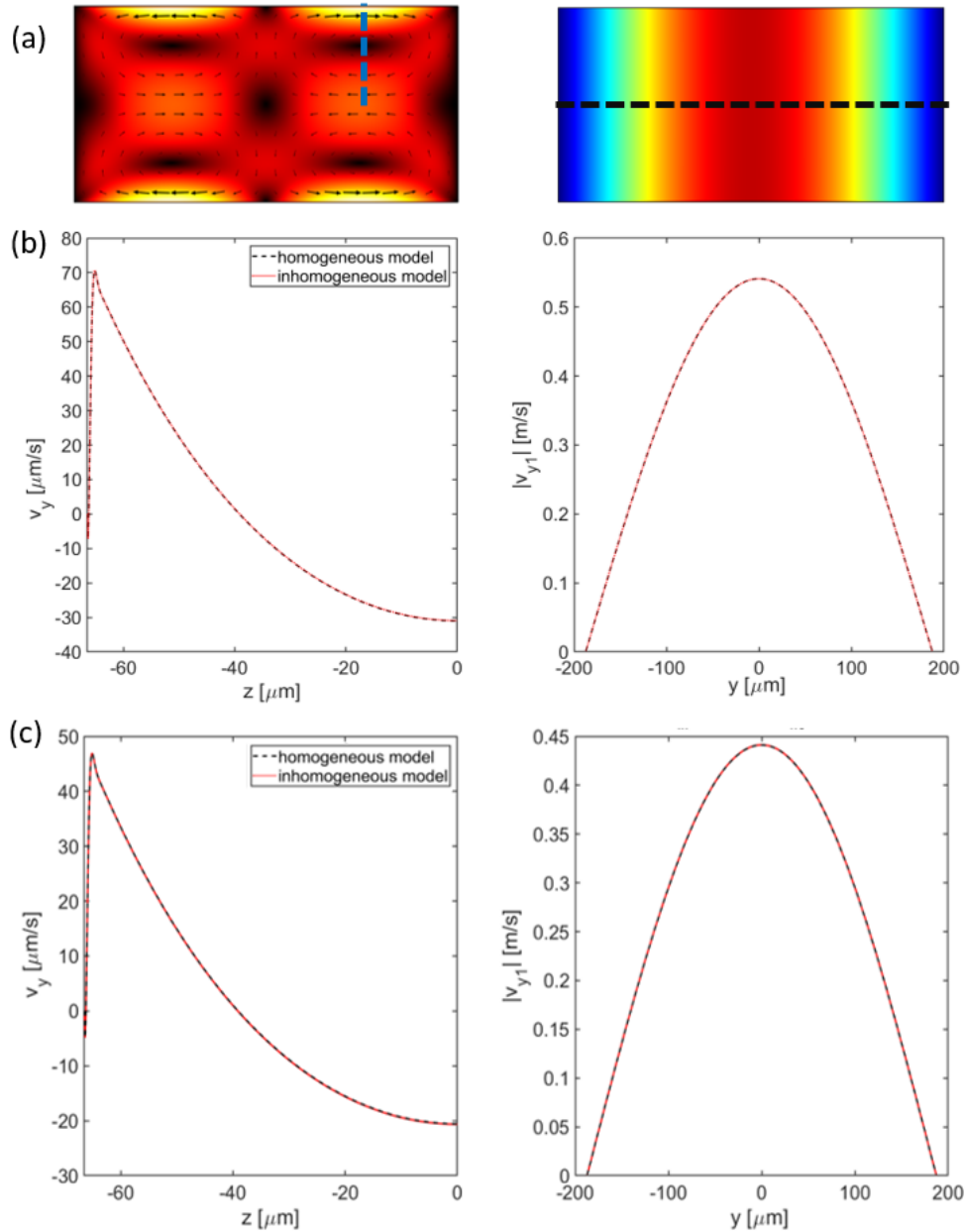


Figure 5.6: Comparison of the "homogeneous" and "inhomogeneous" model for the acoustic streaming (left column) and the first order velocity field (right column). (a) It is sketched through line in the contour plots the reference location for the data. (b) Results for a chamber filled with water. (c) Results for a channel filled with 5% iodixanol.

[75, 95, 96, 130] was used to simulate stop-flow systems. Before approaching to a full 3D model, we chose to use the model shown in the previous subsection, to predict the

particles tracing with a "pseudo 3d model". In this section a general background on the working principle of the method is shown and the results for both the stabilized and relocated inhomogeneity will be exposed.

5.4.1 Idea behind the pseudo 3D model

Since the 2D model, validated above, predicted very well the acoustic body force and the concentration profile (also inside the boundary layers), it was modified and used for a particle tracing in a 3D point of view. Since the impedance is function of the concentration, the particles feel the acoustic radiation force in a different magnitude as function of their position in the cross section, until they have reached their iso-acoustic focusing point (zero acoustic contrast factor Φ_{ac} [60]). This aspect plays an important role in particle separation, as more as if cells/nanovesicles are considered where the compressibility and density is highly variable. The third fluid velocity component could influence the viscosity, density and compressibility profile, thus a "pseudo 3D model" was implemented for taking in account of that problem. Considering for now only the fluid, without particles, what we had was a model which was able to predict the concentration and velocity field in a stop-flow condition (i.e. at a fixed cross-section along the channel and all the fields are function of y-z coordinates and time t). At this point we introduced a changing from a time-dependent problem to a stationary-problem, considering the so-called "plug flow assumption".

The plug flow assumption

In plug flow, the velocity profile is assumed to be constant at any point of all the cross-sections of the considered channel. That assumption should be not reasonable for microfluidic systems, since it does not consider the presence of boundary layers which could influence the velocity profile. We chose anyway to try with that simplification because the velocity in the x direction (i.e. along the length of the channel) is very much higher than the velocity in the other two directions. Thus, our assumption, schematically sketched in Fig. 5.7, consisted in a fluid that moves with a constant mean velocity and let us to convert the system from a transient 2D model to what we called a pseudo 3D. As can be seen in Fig. 5.7 the changing from a dependency in time to space is linked to the mean velocity $v_{p,i}(x, y, z)$. This velocity plays a key role in this step. In fact, considering now the particles, they are affected in the y-z direction by the acoustic streaming velocity and by the "Poiseuille-flow" in the x direction. We computed an analytical solution for the velocity in the x direction in a rectangular cross-sectioned channel, as [65]

$$v_x(y, z) = \frac{4h^2 \Delta p}{\pi^3 \eta L} \sum_{n, odd}^{\infty} \frac{1}{n^3} \left[1 - \frac{\cosh(n\pi \frac{y}{h})}{\cosh(n\pi \frac{w}{2h})} \right] \sin\left(n\pi \frac{z}{h}\right), \quad (5.8)$$

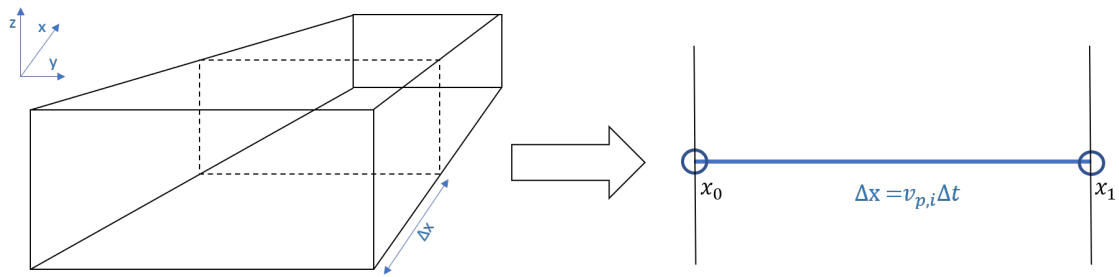


Figure 5.7: Sketch of the transformation from a time-dependent problem to a space-dependent problem through the mean velocity $v_{p,i}(x, y, z)$.

where h is the height of the channel, w is the width of the channel, η is the mean value of the viscosity between the higher and lower viscous fluids, L is the length of the channel and Δp is the pressure drop along the channel. The obtained profile changes dependently on the imposed flow rate. An example is reported in Fig. 5.8. From this profile, it is possible to notice that a particle velocity is strictly dependent on its position in the y - z plane.

Working principle of the model and MATLAB script

The inhomogeneous model was developed using COMSOL Multiphysics and the expansion Livelink with MATLAB. Firstly, the 2D model was implemented in COMSOL as shown in section 5.3.1. Using Livelink with MATLAB was possible, through specific commands, to import and use the background fields for the particle tracing. The working principle of the model is that all the particles experience the same starting concentration profile, but as expressed before a different velocity in all the directions as function of their position in y - z plane. Thus, we considered the motion of one particle for iteration. This let us to compute for each iteration the corresponding field that a particle could experience after a displacement function of its own velocity. The particles trajectories were computed using a Runge-Kutta method. The full script is reported in Appendix B (the % sign denotes the comments). As result of this script we

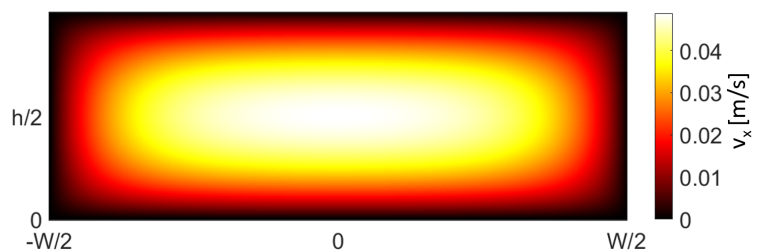


Figure 5.8: Contour plot of the velocity in the x direction $v_x(y, z)$ obtained with eq.5.8 for a flow rate of $500 \mu\text{l}/\text{min}$.

obtained ppx , ppy and ppz , which are the matrices that contain all the positions of the N_p particles.

Particles and fluid properties

For this numerical study we investigated the separation of white blood cells (WBC) and platelets (PLT). As the acoustic radiation is function of the particles properties respect to the medium we performed a literature search about cells in blood (as reported in Table 5.1). It can be seen in Table 5.1, that there is a lack in literature of compressibility

Type	ρ_p [kg/m ³]	k_p [1/Pa]
RBC (Erythrocytes)	1100 [132]	3.33e-10 [133]
	1099 [134]	3.42e-10 [134]
	1099 [134]	3.36e-10 [134]
WBC (Generic)	1054 [135]	3.93e-10 [135]
Leukocytes	1055 [136]	3.99e-10 [137]
	1065 [136]	3.99e-10 [137]
Neutrophils	1075 [136]	3.59e-10 [60](*)
	1085 [136]	3.62e-10 [60](*)
Lymphocytes	1055 [136]	3.69e-10 [60](*)
	1070 [136]	3.75e-10 [60](*)
Monocytes	1055 [136]	3.69e-10 [60](*)
	1070 [136]	3.75e-10 [60](*)
Platelets	1040-1060 [136]	
(*) compressibility calculated from acoustic impedance Z		

Table 5.1: Properties of blood cells from literature.

values for platelets, thus following the trend for the other cells we supposed a compressibility of $3.7\text{e-}10$ [1/Pa] and we set a radius of $1\ \mu\text{m}$. For what concern white blood cells, they present an high heterogeneity in density, size and compressibility. We chose then to set the properties of Neutrophils which are the most present in a blood sample [60]. In this case we set a radius of $5\ \mu\text{m}$. Since this is a former study of the behaviour of particles in absence of acoustic streaming in a inhomogeneous fluid, we starting focusing on the separation based on a slightly difference in size, compressibility and density between the chosen cells. This motivation was also based on the lack in literature of

extracellular physical properties, such as compressibility. Moreover, this last type of cells present a big difference in size which lead to a hard correct modelling of a realistic particle trajectory. We chose to study a different molecule from iodixanol [60] and Ficoll PM 400 [95]. We simulated Ficoll Paque, which properties dependency on concentration is shown in Fig. 5.9. As reflected in the plots, this solute does not introduce a great gradient in properties. This means that the acoustic body force is weaker respect to the two above mentioned solutes. Ficoll-Paque is a ready-to-use density gradient media commonly used for the preparation of mononuclear cells. An aqueous solution with 5% Ficoll Paque is used as high impedance fluid, while water is used as lower density fluid for both the stabilized and relocation simulations. It was calculated that this concentration gradient led to around 0.4% difference in density, 3% in viscosity and close to 0% for speed of sound.

5.4.2 Stabilized inhomogeneity

A stabilized configuration is shown in Fig. 5.10. The high-density buffer is injected in the central stream. The concentration profile is stabilized by the acoustic body force f_{ac} . The suspended particles in water are injected in the side streams. The principle is that bigger particles (WBC in this test) are moved by acoustic radiation force in the central pressure node. The smaller particles, which experience a lower F_{rad} are dragged following the stream forward the outlet, since they need more time to be focused. Thus, the expectation was that the efficiency of this separation lied on the imposed flow rate. We imposes a constant flow rate ratio both to the inlet and to the outlet. We set the side streams to be each 12.5% of the total flow rate and the central one the remaining 75%. For what concern the outlets, the sides streams were set to be the 37.5% of the total flow rate and the central one the remaining 25 %. We chose the frequency to keep constant the acoustic energy density at a value of 50 Pa, sweeping over time the displacement of the lateral walls.

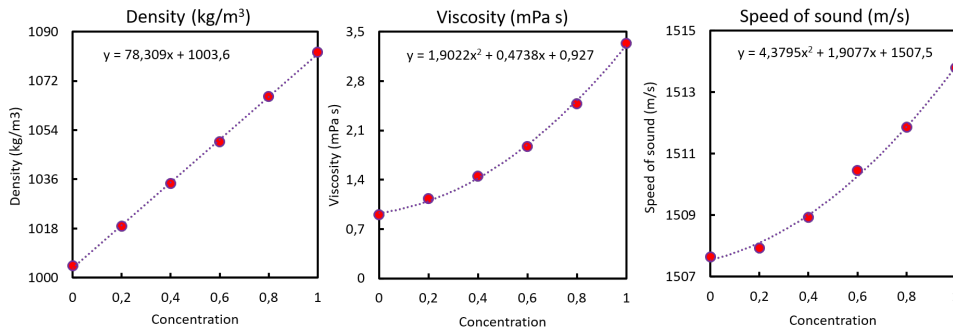


Figure 5.9: Properties of Ficoll Paque as function of the concentration.

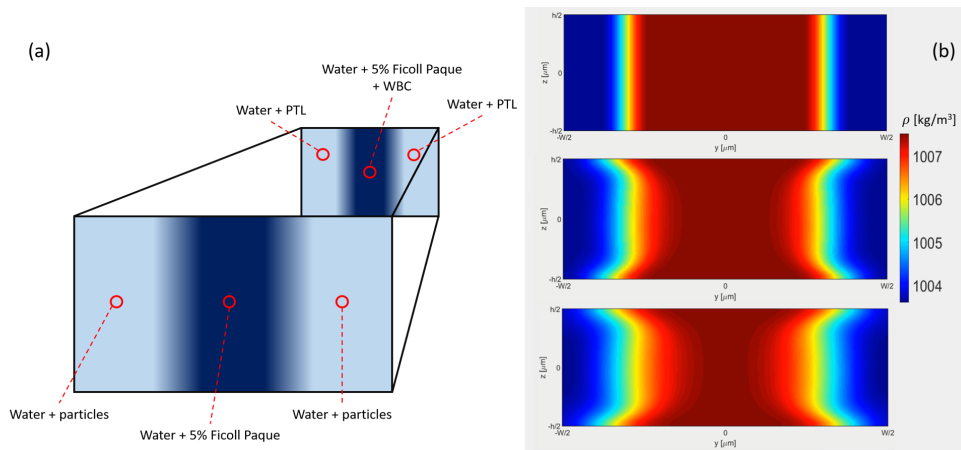


Figure 5.10: (a) Sketch of the separation in stabilized configuration. (b) Three space frames of the concentration profile along the channel for an aqueous solution with 5% Ficoll Paque (inlet at the top and outlet at the bottom of the column). Colourbar from blue, lower density, to red, higher density.

Results of pseudo 3D model for a stabilized configuration

We studied this configuration at different flow rates. The collected results are shown in Fig. 5.11. As can be seen, there is a strict correlation between the separation efficiency and the applied total flowrate. The best condition is achieved for values higher than 300 $\mu\text{l}/\text{min}$ which allows to obtain a pure sample of white blood cells in the central stream.

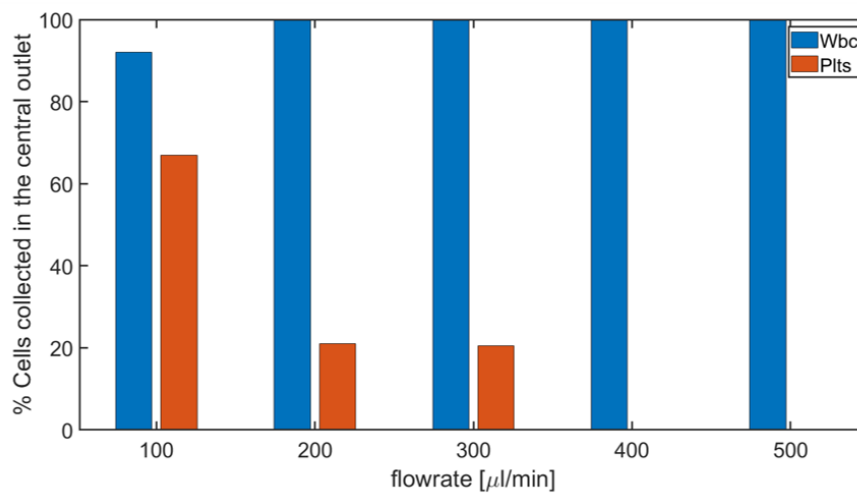


Figure 5.11: Percentages of cells collected in the central outlet as function of the total applied flow rate at the inlet for a stabilized configuration.

5.4.3 Fluid relocation

The fluid relocation, as mentioned above, happens when the fluid with higher impedance is injected at the side streams and the sound is turned on. This configuration led to an acoustic body force which relocates the fluid, moving the higher density fluid at the centre. In this case the working principle is to inject the sample (water and particles) in the central stream and let the high-density buffer to relocate. This will push all the particles at the sides and, since the platelets experience a lower acoustic radiation force, a pure sample of white blood cell, which are faster moved at the pressure node, can be collected through the central outlet (as sketched in Fig. 5.12). What we expected from this configuration, knowing the results from the previous tests, was a higher efficiency for lower flow rates and a less marked dependency on them. Also in this case the flow rate ratio between central and lateral streams was kept constant. For relocation configuration, the 75 % of the total flow rate was set at the lateral stream, while the remaining 25 % was set at the central stream. The same ratio was maintained at the outlets. As done before, we kept constant the acoustic energy density at 50 Pa, through a sweeping of the displacement of the lateral walls.

Results of pseudo 3D model for fluid relocation

Also for the relocation configuration, we studied different flow rates in a range from 100 $\mu\text{l}/\text{min}$ to 500 $\mu\text{l}/\text{min}$. The particles properties are the same listed in the previous section. The results collected for this configuration are shown in Fig. 5.13. The plot does not show a clear trend as function of the flow rate. In this case the best results were obtained for 200 $\mu\text{l}/\text{min}$. This could be explained thinking about the position of the

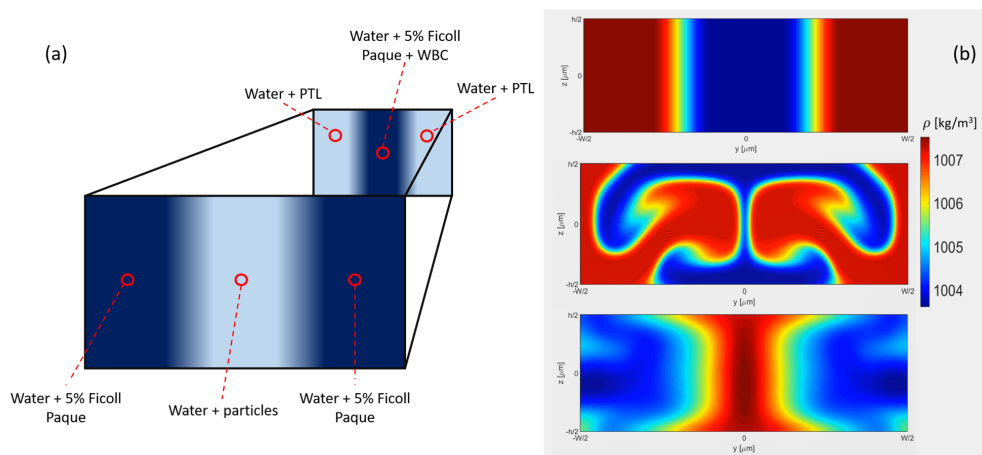


Figure 5.12: (a) Sketch of the separation in fluid relocation configuration. (b) Three space frames of the concentration profile along the channel for an aqueous solution with 5% Ficoll Paque (inlet at the top and outlet at the bottom of the column). Colourbar from blue, lower density, to red, higher density.

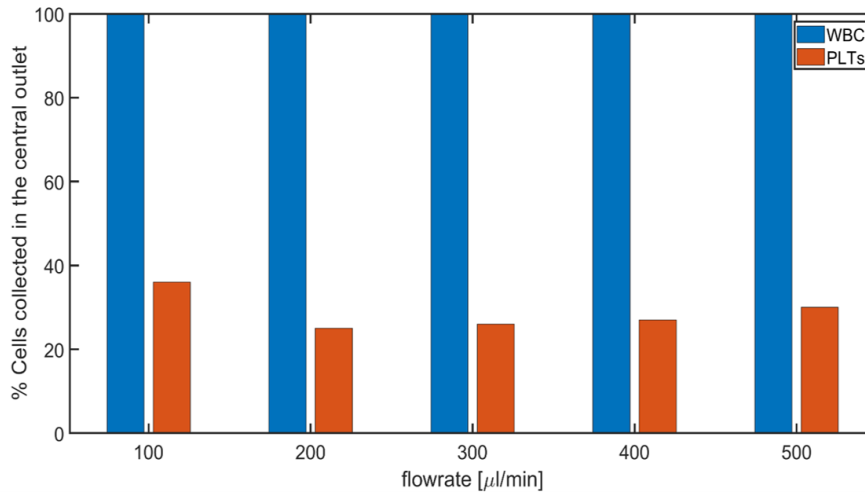


Figure 5.13: Percentages of cells collected in the central outlet as function of the total applied flow rate at the inlet for a fluid relocation configuration.

relocation. At lower flow rate the switch between the fluids happens close to the inlet, giving time to both the smaller and bigger particles to experience the acoustic radiation force and be focused. For higher flow rate the relocation take place in sections closer and closer to the outlet. This means that some platelets have not time to be moved by the drag force during the medium switch, thus are collected in the central outlet (in smaller percentages respect to 100 $\mu\text{l}/\text{min}$).

5.5 Continuous flow 3D model

The plug flow assumption is a very strong "simplification" of the problem. The fluid is moving with a constant mean velocity in the whole sections, and we assumed that was reasonable, particularly if the lightly difference in viscosity and density introduced is by 5% of Ficoll Paque. Despite of that, we chose to confirm this through a 3D model which involved the limiting velocity theory, previously introduced in [chapter 4](#).

Numerical model

The model was structured following the same approach proposed in [chapter 4](#). The first-order acoustic fields were simulated using the built-in module in COMSOL "Pressure Acoustics, used for solving eq. 4.20. Through the obtained 1st order velocity field was possible to calculate the limiting velocities (eq.4.21 and eq.4.22). Despite of using the predefined COMSOL's "Creeping Flow" physic for the slow-time-scale hydrodynamic fields, we implemented them in their weak form. Thus eq. 5.5, 5.6 and 5.7 were

used for the continuity of mass, of momentum and for the advection-convection transport equation, respectively. The 3D device had width of $375 \mu\text{m}$, height of $133 \mu\text{m}$ and length of 2 cm. As done in the previous chapter, the mesh was built with tetragonal elements, and their length was chosen to have at least 8 of them along the width [127]. It is important to underline that also in this case a finest mesh close to the boundary it is not needed cause the limiting velocity theory introduce and analytical solution of the acoustic streaming outside the boundary layers. This permits to decrease the computation demand through a coarser mesh. Obviously, the effects inside the boundary layer are neglected.

Stabilized inhomogeneity

To compare with the pseudo 3D model, we maintained the ratio between the side and the central flow rate (25% of the total flow rate for the lateral streams and 75% for the central at the inlet and the opposite for the outlet). For a convergence point of view, we had to change in this case the concentration of Ficoll Paque from 5% to 10%. Also in this case we chose the proper frequency in order to obtain a constant acoustic energy density of 50 Pa. For the stabilized configuration we obtain a very similar results for the concentration profile (shown in Fig. 5.14).

This test revealed that the x-velocity parabolic profile does not influence the stabilized concentration field.

Fluid relocation

Turning now to the acoustic fluid relocation, also in this case a solution of 10% Ficoll Paque was used, and the acoustic energy density was set at 50 Pa. It can be seen from Fig. 5.15 that the concentration profile is slightly influenced by the Poiseuille flow. This means that the results reported for the relocation approach need to be validated,

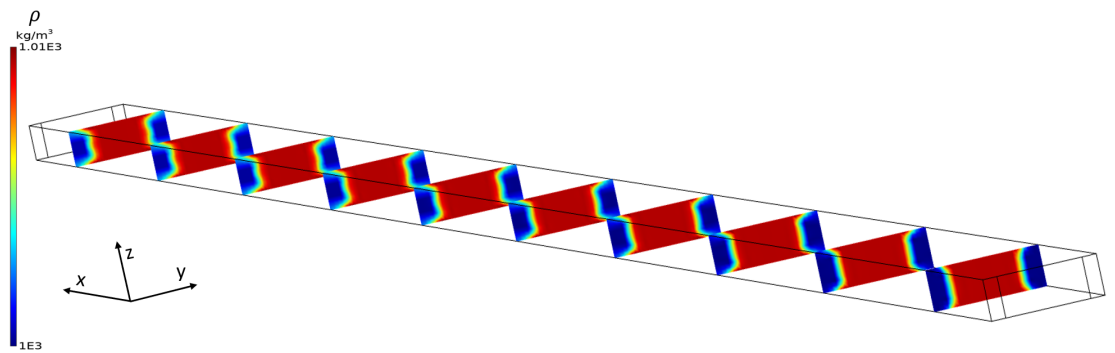


Figure 5.14: Density profile in different slides along the channel with an aqueous solution of 10% Ficoll Paque injected in the central stream. Colourbar from blue, lower density, to red, higher density.

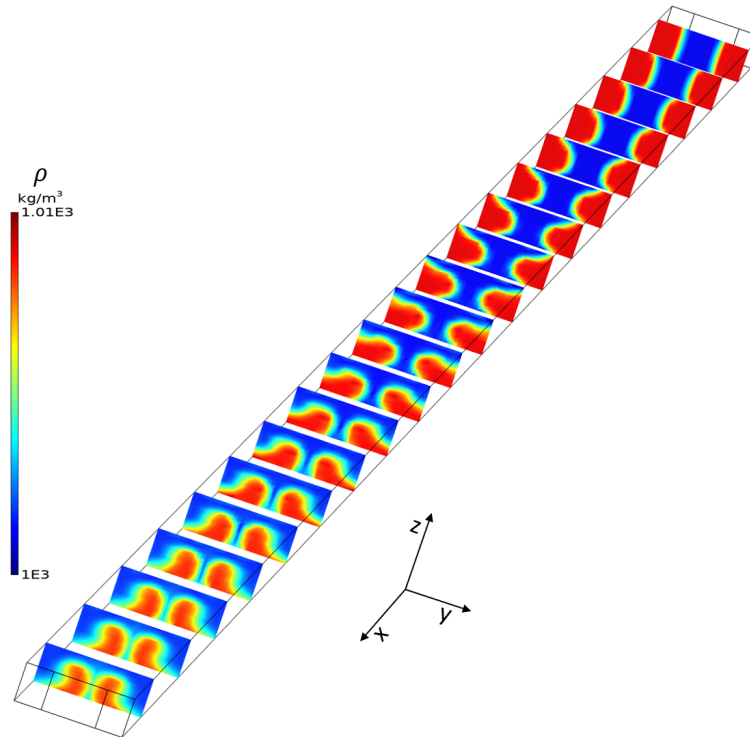


Figure 5.15: Density profile in different slides along the channel with an aqueous solution of 10% Ficoll Paque injected in the lateral streams. Colourbar from blue, lower density, to red, higher density.

an experimental validation of the concentration profile could help in this. What can be expected is a slight difference of the separation efficiency respect to the proposed pseudo-3d model. The higher density fluid seems to relocate with a sharper interface and a more defined concentration profile can be seen. But since the aim of the relocation is to push all the particles on the sides of the channel, and that is achieved in both the proposed models, the separation results should not change significantly.

5.6 Conclusions

The idea of using acoustic fluid relocation for the separation of nanoparticles came from Gautam et al. [131]. A further investigation was needed to understand the potential of this approach respect to the stabilized configuration. A resonance analysis was performed, and an interesting result was shown. The initial configuration of the higher impedance fluid led to a shift in the resonance condition outside from "boundary values" of the homogeneous solutions. This phenomenon needs a deeper understanding, and it could be useful for systems with an higher induced inhomogeneity in the medium. A

pseudo 3D model was initially used to compare the efficiency of the stabilized and relocation configuration for the separation of platelets from white blood cells. This model was based on the one proposed by Karlsen et al. [75, 96, 130] and transformed into a stationary problem through the plug flow assumption. Using this model was possible to obtain results for the separation for both the stabilized and relocation approach. Since the density, viscosity and compressibility are position dependent, the Poiseuille profile, induced by the applied flow rate, could influence the concentration profile. We verified this using the limiting velocity theory [126, 127] for implementing a 3D model with a coarser mesh. We obtained two important pieces of information from this test. The former one is that 5% Ficoll Paque led to a very small variation in properties and the magnitude of the acoustic body force is not enough to move the liquid and relocate it. The second interesting result is that the relocation profile seems quite different between the pseudo 3D model and the full 3D model. Any experimental test has to be performed to validate both the concentration profile and understand which is the most correct. Certainly, this study paves the way to further investigation about the separation of nanoparticles using fluid inhomogeneity approach. In fact, both the proposed models were performed considering WBC and PLT which are micro-metric cells. An interesting future study could be the separation of a mixture of micro- and nano-particles, for example white blood cells and exosomes. In order to perform that, a deeper understanding of the extracellular vesicles properties is needed. The expected result in using smaller biological particles instead of platelets, thus an increased difference in size respect to WBC, could be an improved efficiency in the separation. In fact, due to the strong radiation force experienced by the micrometer sized particles, they would be focused very fast. On the other hand, for the opposite behaviour, the sub-micrometer cells are moved slowly, more than the PLT. This means that the separation can have good results also for low flow rate and the purity of the samples collected can be higher, in both the stabilized and relocated configuration. In conclusion, respect to what presented by Karlsen et al. [90, 95, 130, 75], this study is focused on the understanding of the behaviour that particles with different properties can have when suspended in an inhomogeneous fluid and the separation efficiency of this approach. That was experimentally proposed recently by Gautam et al. [131], which used the relocation of fluid to separate nanoparticles in a mixture with microparticles. In order to have a deeper understanding of the parameters that could influence the separation, we compared both the stabilized configuration and the relocation, coming to a very starting conclusion, that the former one seem to have higher efficiency in terms of purity of the collected samples.

Chapter 6

Conclusions

Nanoparticles world is playing a key role in a lot of research fields. One of the most affected is the biotechnological, pharmaceutical, and medical fields. The study of these nano-scaled bodies aim to detect pathologies and biomarkers and to improve the understanding of important physiological principles of several disease and their treatments. Recently a deeper attention has been given to extracellular nanovesicles (i.e. exosomes). These nano-sized particles are responsible for carrying a disparate type of biomolecules and involved in pathological and physiological processes. For these particular properties, they have attracted huge interest in the world of research as innovative and feasible tool for the diagnosis of several diseases (i.e. cancer). In particular is underlined the necessity to investigate efficient approaches for the concentration/isolation of these nanoparticles. The commonly used techniques for their separation, have the advantages of being very efficient, but they are time-consuming, labour-dependent, discontinuous and they require huge amount of sample volume. The requirement of an alternative, continuous and user-friendly technique for the separation of nanoparticles has grown interest in the scientific community. Microfluidic devices have shown great potentiality in this context. In literature both passive and active micro-systems are presented as performing tools for the separation, concentration, isolation of nanoparticles. At the light of these studies, the presented PhD project aimed to investigate different strategies for the separation of nano-sized particles in a blood sample. The starting point of this work was focused on the development of a first module based on a passive microfluidic device. This system was based on a size-exclusion technique, where the separation occurred as function of the diameter of the treated particles. A pillar-arrays filter was placed inside a straight microfluidic channel to confine particles bigger than the gap between the trapezoidal shaped pillars and let the smaller one to pass through. Several pressure tests and numerical controls were performed in order to obtain the most homogeneous mass-flow and velocity profile through every filtering module inside the channel. This helped us to obtain the most performant layout, which was used for fluorescence microscopy tests as validation of the separation efficiency. These tests showed us very promising results for particles bigger than $2 \mu\text{m}$, i.e. red blood cells or

white blood cells. Experimental preliminary validation showed that it is not the same for smaller particles, which separation requires a very narrower gap between the pillars and thus harder fabrication processes. Thus, it was possible to think at this device as a pre-cleaning stage, where bigger corpuscles such as red blood cells, and white blood cells can be confined and obtain a purer blood sample composed by plasma, platelets, and extracellular vesicles. The second part of the project involved the development of active microfluidic systems, where the fabrication process is less tricky instead of a more complex physics behind. The acoustophoretic technique was chosen as promising method for the separation of nanoparticles. One of the most physical limits of this approach is the presence of the acoustic streaming phenomenon. This damping induced steady fluid flow drags sub micrometer particles making their separation very tricky. In [chapter 4](#), an investigation on the aspect ratio to limit this effect was performed and interesting results were obtained through this study. An increasing in aspect ratio corresponds to the propagation of a "free zone" in the middle of the channel which limits the acoustic streaming rolls closer to the boundaries. This phenomenon has an important influence on particles focusing, achieving good efficiency also for diameter under the micron. The most efficient layout reported was a cross-section with a width of 174 μm and a height of 349 μm , corresponding to an aspect ratio of 2. With this design, particles with a diameter under the micron can be collected at about 80% in a central stream. Moreover, micrometer particles are moved at 100% in the central portion of the section. Unfortunately, an experimental validation was not possible, thus a further investigation considering systematic errors and equipment uncertainty could make these results even more interesting. Moreover, particles with different properties respect to polystyrene (i.e. cells) or other suspending mediums could be used to investigate if it is possible to achieve analogous efficiencies in different conditions. Regarding new medium, a particular attention was given to inhomogeneity properly induced by chosen solute concentration profile. A model which could track the evolution of the fluid properties profile for a stop-flow system was developed. For obtaining a comparison of the separation efficiency, two kinds of configuration were investigated: the stabilized and the fluid relocation. A "pseudo 3D model" was implemented considering a plug-flow assumption, since, from an experimental point of view, the acoustophoretic separation happens in continuous systems. This model predicted fascinating results, strictly dependent on the imposed total flow rate. A mixture of white blood cells and platelets was considered. They do not present a great variation in physical properties, but there is a slight difference in diameter. For a stabilized configuration, a pure sample of white blood cells can be obtained in the central stream with a flow rate higher than 400 $\mu\text{l}/\text{min}$. This corresponds to a pure sample of platelets at the side streams. With fluid relocation this efficiency was not possible. In fact, the best setup found was with a flow rate of 200 $\mu\text{l}/\text{min}$ with 100% white blood cells and about 20% platelets collected in the central stream. Due to this influence of the flow rate on the separation, it was also investigated the dependency of the concentration profile on the third dimension

of the velocity field. The evidence from this study suggests that for a stabilized configuration the concentration field is not hardly influenced by the flow rate, the same cannot be said for the fluid relocation. In fact, with this last configuration, the fluid is not presenting the same behaviour shown in the pseudo 3D model. A sharper concentration profile was observed. This result can lead to a different separation efficiency. Further experimental work needs to be carried out to establish whether the concentration profile is well predicted. Since using inhomogeneous fluid, different parameters can influence the separation of nanoparticles, such as solute concentrations, acoustic energy density and particle properties, future studies on these are therefore required. Thus, we believe that the present findings might help to achieve important result in the isolation/concentration of sub-micrometer particles (i.e. exosomes). In conclusion the presented PhD project achieved important results on the optimization, design, and modelling of microfluidic systems, both passive and active, for the separation of particles. As mentioned above, some of the presented results need a future experimental validation. Moreover, further works should focus on enhancing the quality of the presented results, for example for what concern the comparison of the separation between a stabilized inhomogeneity or a fluid relocation. Moreover, it should be interesting to enhance the concentration induced inhomogeneity and analyse the efficiency of the system when a higher acoustic body force is present. The proposed acoustophoretic approach is not limited only to the detection of biomarker/separation of nanoparticles. In fact, it should be suitable for all the applications that involve the separation of nanoparticles from a poly-dispersed sample. An example is the synthesis of nanoparticles for catalysis. Since smaller diameters correspond to a higher surface area, a separation step could decrease the polydispersity and enhance the catalysis efficiency. Another possible application could be the separation of bacteria or micro/nano pollutants in a water sample. This last, in fact, could be treated in a pre-cleaning acoustophoretic device. The acoustophoretic technique, since it is strictly dependent on the physical properties of the particles, could be used also for enhance the production of nano-carriers. These nanoparticles (or nano-capsules) have inside a drug that need to be carried, therefore they present different density and compressibility respect to empty carriers. Thus, it should be possible to obtain a full sample with particles loaded with the desired drug. Thus, the acoustophoretic approach presents a high potentiality for further studies not only close to the biomedical world.

Appendix A

Acronyms

AR	aspect ratio
BAW	Bulk Acoustic Waves
BOE	Buffered Oxide Etch
CFD	Computational Fluid Dynamic
COC	Cyclic Olefin Copolymer
DEP	Dielectrophoresis
De	Dean Number
DLD	Deterministic Lateral Displacement
DRIE	Deep Reactive Ion Etching
FEM	Finite Element Method
FFA	free flow acoustophoresis
FVM	Finite Volume Method
ELISA	Enzyme-linked Immunosorbent Assay
ExoTIC	Exosome Total Isolation Chip
EVs	Extracellular Vesicles
FFF	Field flow fractionation
GNPs	Antibody-coated Gold Nanoparticles probes
ICP	Ion concentration polarization

IPA	isopropanol
MVEs	Multivesicular Endosomes
nPES	Nanoplasmon-Enhanced Scattering
PDEs	partial differential equations
Pe	Péclet number
PLT	platelets
RBC	red blood cells
Re	Reynolds number
SEC	Size-exclusion chromatography
SAW	Surface Acoustic Waves
μFFE	miniaturizing free-flow electrophoresis
WBC	white blood cells

Appendix B

Matlab Script for Pseudo 3D Model for inhomogeneous fluids

```
1 %% import COMSOL class and load mph model
2 clear all; %clear all the the variable in the workbench
3 close all; %close all the functions
4 import com.comsol.model.*; %import of the class model
5 model = mphload('Inhomogeneous_5%FICOLL_PARQE_working_dummy_relocation.mph'); %
    load the 2D model called : "Inhomogeneous_5%
    FICOLL_PARQE_working_dummy_relocation.mph"
6 vars=getVariables(model); %create a struct called vars which contains all the
    variables defined in COMSOL
7 disp('Loading done') %display "Loading done"
8
9 %% run the stationary solver for initialize the first order
10 import com.comsol.model.util.*
11 ModelUtil.showProgress(true) %show progress bar
12 mphevaluate(model,'f0') %show the set value for the frequency
13 model.param.set('f0',2.007e6); %set the desired value of frequency
14 mphevaluate(model,'f0') %show the set value for the frequency
15 model.study('std3').run() %run the first time-step for initialized the acoustic
    fields
16 disp('stationary solving complete')
17
18 %% Evaluation of acoustic energy density for stationary study
19 Eac_stationary=mpghlobal(model,'avg_bulk(Eac)', 'Dataset', 'dset3');
20 %evaluation of the obtained acoustic energy density
21
22 %% create the mesh for fields in MATLAB
23 W=mphevaluate(model,'W'); %evaluate the width
24 h=mphevaluate(model,'H'); %evaluate the height
25 Ny=W*1e6; %Number of point in y direction
26 Nz=h*1e6; %Number of point in z direction
27 y=linspace(-W/2,W/2,Ny); %create a spacing vector in the y-direction
28 z=linspace(-h/2,h/2,Nz); %create a spacing vectore in the z-direction
```

```
29 [YG,ZG]=meshgrid(y,z); % create a mesh
30 mesh_for_comsol=[YG(:),ZG(:)]'; %convert the mesh of matlab in a structure that
    COMSOL can read
31 disp('all the parameter for the mesh in matlab are imported')
32
33
34 %% Computation of the Poiseuille Flow
35 L=0.03; %set le length of the channel
36 Q=500e-9/60; %set the flow rate
37 vx=PoiseuilleFlow(L,Q,W,h,Ny,Nz); %import the velocity v_x obtained
    analytically by eq. 5.8
38 N=400; %set a value for the length of the 3rd dimension
39 for i=1:N %loop that set the Poiseuille profile along all the channel
40     v_x(:, :, i)=vx;
41 end
42 mean_vx=mean(mean(vx)); %compute the mean velocity through the velocity profile
    vx
43 time_length=L/mean_vx; %compute a mean time for the fluid to exit the channel
    if the velocity is considered constant
44
45 %% set the initial time and the final time
46 model.param.set('tstart',0);
47 model.param.set('tend',time_length);
48 disp('initial and final time are set')
49
50 %% Computation of transient solver
51 model.study('std1').run(); % run the study which will contains all the fields
    in the time-range defined above
52
53 %% initialization of all variables that will change during the particle tracing
    .
54 vy2=zeros(Nz,Ny,N+1);
55 vz2=zeros(Nz,Ny,N+1);
56 rhof=zeros(Nz,Ny,N+1);
57 vis=zeros(Nz,Ny,N+1);
58 C_f=zeros(Nz,Ny,N+1);
59 Kappaf=zeros(Nz,Ny,N+1);
60 vy=zeros(Nz,Ny,N+1);
61 vz=zeros(Nz,Ny,N+1);
62 Frad=zeros(Nz,Ny,N+1);
63 Fnet=zeros(Nz,Ny,N+1);
64 f1=zeros(Nz,Ny,N+1);
65 f2=zeros(Nz,Ny,N+1);
66 Beta=zeros(Nz,Ny,N+1);
67 Gamma=zeros(Nz,Ny,N+1);
68 constrast_factor=zeros(Nz,Ny,N+1);
69 vz=zeros(Nz,Ny,N+1);
70 vy=zeros(Nz,Ny,N+1);
71
```

```

72  %% take the fields at the inlet (t=0 -> x=0), which is equal for all the
    particles
73  temp= mphinterp(model,'vx','coord',mesh_for_comsol,'t',0);
74  vy2(:, :, 1)=reshape(temp,Nz,Ny);
75  temp= mphinterp(model,'vy','coord',mesh_for_comsol,'t',0);
76  vz2(:, :, 1)=reshape(temp,Nz,Ny);
77  temp= mphinterp(model,'rho','coord',mesh_for_comsol,'t',0);
78  rhof(:, :, 1)=reshape(temp,Nz,Ny);
79  temp= mphinterp(model,'k','coord',mesh_for_comsol,'t',0);
80  Kappaf(:, :, 1)=reshape(temp,Nz,Ny);
81  temp= mphinterp(model,'mu','coord',mesh_for_comsol,'t',0);
82  Cf(:, :, 1)=reshape(temp,Nz,Ny);
83  temp= mphinterp(model,'c_f','coord',mesh_for_comsol,'t',0);
84  vis(:, :, 1)=reshape(temp,Nz,Ny);
85  disp('the fields in the first section are computed')
86
87  %% Parameters for particle tracing
88  ky=pi/W; %wavenumber
89  thbou=vars.d_visc; %viscous boundary layer
90  f=vars.f0; %frequency
91  g=9.8; %gravity acceleration
92  rhop=1.058e3; %particles density
93  a=2e-6/2; %particle radius
94  % Z=1.63e6; %Acoustic particle impendance
95  % Kappap=rhop/Z^2; %particle compressibility from acoustic impendance
96  Kappap=3.7e-10; %particle compressibility
97
98  %%definition of time step for particle tracing
99  time=linspace(0,10,N);
100 dt=time(2)-time(1)
101
102 %% define initial position of the particles at the inlet
103 b_y=-W/2+W*0.375+a;
104 a_y=W/2-W*0.375+a;
105 b_z=h/2-3*a;
106 a_z=-h/2+3*a;
107 N_p=100; % number of particles
108 Ini_y=zeros(1,N_p);
109 Ini_z=zeros(1,N_p);
110 vpy=zeros(N+1,N_p);
111 vpz=zeros(N+1,N_p);
112 ppy=zeros(N+1,N_p);
113 ppz=zeros(N+1,N_p);
114 ppx=zeros(N+1,N_p);
115 vpx=zeros(N+1,N_p);
116 rand_left=a_y+(-a_y+b_y).*rand(N_p/2,1)';
117 rand_right=-a_y+(+a_y-b_y).*rand(N_p/2,1)';
118 Ini_y(1,1:N_p/2)=rand_left;
119 Ini_y(1,N_p/2+1:N_p)=rand_right;
120 Ini_z=-b_z+(b_z-a_z).*rand(1,N_p);

```

```

121
122 %% Constrast factor-Radiation Force-and velocity at the inlet.
123 Beta(:,:,1)=Kappap./Kappaf(:,:,1); %ratio of compressibility
124 Gamma(:,:,1)=rhop./rhof(:,:,1);
125 f1(:,:,1)=1-Beta(:,:,1); %monopole term
126 delta=thbou./a;
127 f2(:,:,1)=((2+3.*delta).*(Gamma(:,:,1)-1))./(2*Gamma(:,:,1)+1+(9/2)*delta); %
    dipole term
128 constrast_factor(:,:,1)=f1(:,:,1)/3+f2(:,:,1)/2;
129
130 for ii=1:length(z)
131 for jj=1:length(y)
132 Frad(ii,jj,1)=-2*ky*2*pi*a^3*Eac_stationary*constrast_factor(ii,jj,1)*sin(2*ky*
    y(jj)); %acoustic radiation force at the inlet
133 Fnet(ii,jj,1)=-(rhop-rhof(ii,jj,1)).*g*(4/3)*pi*a.^3;%create a net force from
    bouyancy and gravity on a particle
134
135 %%Computation of particles velocity
136 vz(ii,jj,1)=(Fnet(ii,jj,1))./(6.*pi.*vis(ii,jj,1).*a)+vz2(ii,jj,1);
137 vy(ii,jj,1)=Frad(ii,jj,1)./(6.*pi.*vis(ii,jj,1).*a)+vy2(ii,jj,1);
138 end
139 end
140
141 %% Start particle tracing
142 ppy(1,:)=Ini_y; %initial position in y
143 ppz(1,:)=Ini_z; %initoal position in z
144 ppx(1,:)=zeros(1,N_p); %initial position in x
145 f=waitbar(0,'Starting particle tracing'); %create a waiting bar for the
    particle tracing process
146 for n=1:N_p %loop for all the particles
147 for k=1:N %loop for the spatial discretization
148
149 %Check for clicked Cancel button
150 if getappdata(f,'canceling')
151 break
152 % Update waitbar and message
153 end
154 waitbar(k/(N),f,sprintf('%d = s of particle tracing for particle %d',k/(N),n))
155
156 %Runge-kutta method for computation of velocity
157 vpy(k,n)=interp2(YG,ZG,vy(:,:,k),ppy(k,n),ppz(k,n),'spline');
158 vpz(k,n)=interp2(YG,ZG,vz(:,:,k),ppy(k,n),ppz(k,n),'spline');
159 vpx(k,n)=interp2(YG,ZG,v_x(:,:,k),ppy(k,n),ppz(k,n),'spline');
160 vyK1=vpy(k,n);
161 vzK1=vpz(k,n);
162 vyK2=interp2(YG,ZG,vy(:,:,k),ppy(k,n)+dt/2*vyK1,ppz(k,n)+dt/2*vzK1,'spline');
163 vzK2=interp2(YG,ZG,vz(:,:,k),ppy(k,n)+dt/2*vyK1,ppz(k,n)+dt/2*vzK1,'spline');
164 vyK3=interp2(YG,ZG,vy(:,:,k),ppy(k,n)+dt/2*vyK2,ppz(k,n)+dt/2*vzK2,'spline');
165 vzK3=interp2(YG,ZG,vz(:,:,k),ppy(k,n)+dt/2*vyK2,ppz(k,n)+dt/2*vzK2,'spline');
166 vyK4=interp2(YG,ZG,vy(:,:,k),ppy(k,n)+dt*vyK3,ppz(k,n)+dt*vzK3,'spline');

```

```

167 vzK4=interp2(YG,ZG,vz(:,:,k),ppy(k,n)+dt*vyK3,ppz(k,n)+dt*vzK3,'spline');
168
169 %compute the next position in the y direction
170 py=ppy(k,n)+dt/6*(vyK1+2*vyK2+2*vyK3+vyK4);
171
172 %elastic hit of the particles in the lateral walls
173 if abs(py)>=W/2-a
174 ppy(k+1,n)=sign(py)*(W/2)-sign(py)*(abs(py)-W/2+2*a);
175 else
176 end
177
178 %fix the particle position in the y direction if the particle is
179 %outside the channel
180 if ppx(k,n)>=L
181 ppy(k+1,n)=ppy(k,n);
182 else
183 ppy(k+1,n)=py;
184 end
185
186 %compute the next position in the z direction
187 pz=ppz(k,n)+dt/6*(vzK1+2*vzK2+2*vzK3+vzK4);
188 if abs(pz)>=h/2-a
189 ppz(k+1,n)=sign(pz)*(h/2)-sign(pz)*(abs(pz)-h/2+2*a);
190 else
191 if ppx(k,n)>=L
192 ppz(k+1,n)=ppz(k,n);
193 else
194 ppz(k+1,n)=pz;
195 end
196 end
197
198 %compute the next position in x direction
199 ppx(k+1,n)=vpx(k,n).*dt+ppx(k,n);
200
201 T=ppx(k+1,n)/mean_vx; %compute T which correspond to the displacement dx
202
203 %% extrapolation of the fields at timet T from COMSOL
204 temp= mphinterp(model,'vx','coord',mesh_for_comsol,'t',T);
205 vy2(:,:,k+1)=reshape(temp,Nz,Ny);
206 temp= mphinterp(model,'vy','coord',mesh_for_comsol,'t',T);
207 vz2(:,:,k+1)=reshape(temp,Nz,Ny);
208 temp= mphinterp(model,'rho','coord',mesh_for_comsol,'t',T);
209 rhof(:,:,k+1)=reshape(temp,Nz,Ny);
210 temp= mphinterp(model,'k','coord',mesh_for_comsol,'t',T);
211 Kappaf(:,:,k+1)=reshape(temp,Nz,Ny);
212 temp= mphinterp(model,'mu','coord',mesh_for_comsol,'t',T);
213 Cf(:,:,k+1)=reshape(temp,Nz,Ny);
214 temp= mphinterp(model,'c_f','coord',mesh_for_comsol,'t',T);
215 vis(:,:,k+1)=reshape(temp,Nz,Ny);
216 Beta(:,:,k+1)=Kappap./Kappaf(:,:,k+1); %ratio of compressibility

```

```
217 Gamma(:,:,k+1)=rhop./rhof(:,:,k+1);
218 f1(:,:,k+1)=1-Beta(:,:,k+1); %monopole term
219 delta=thbou./a;
220 f2(:,:,k+1)=((2+3.*delta).*(Gamma(:,:,k+1)-1))./(2*Gamma(:,:,k+1)+1+(9/2)*delta
    ); %dipole term
221 constrast_factor(:,:,k+1)=f1(:,:,k+1)/3+f2(:,:,k+1)/2;
222 for ii=1:length(z)
223 for jj=1:length(y)
224
225 %%Computation of acoustic radiation Force
226 Frad(ii,jj,k+1)=-2*ky*2*pi*a^3*Eac_stationary*constrast_factor(ii,jj,k+1)*sin
    (2*ky*y(jj));
227 Fnet(ii,jj,k+1)=-(rhop-rhof(ii,jj,k+1)).*g*(4/3)*pi*a.^3;%create a net force
    from bouyancy and gravity on a particle
228
229 %%Computation of particles velocity
230 vz(ii,jj,k+1)=(Fnet(ii,jj,k+1))./(6.*pi.*vis(ii,jj,k+1).*a)+vz2(ii,jj,k+1);
231 vy(ii,jj,k+1)=Frad(ii,jj,k+1)./(6.*pi.*vis(ii,jj,k+1).*a)+vy2(ii,jj,k+1);
232 end
233 end
234 end
235 end
```

Bibliography

- [1] C. de la Torre Gomez et al. “Exosomics”-A review of biophysics, biology and biochemistry of exosomes with a focus on human breast milk.” In: *Front. Genet.* 9.MAR (2018), pp. 1–11. ISSN: 16648021. DOI: [10.3389/fgene.2018.00092](https://doi.org/10.3389/fgene.2018.00092).
- [2] M.H. Rashed et al. “Exosomes: From garbage bins to promising therapeutic targets.” In: *Int. J. Mol. Sci.* 18.3 (2017). ISSN: 14220067. DOI: [10.3390/ijms18030538](https://doi.org/10.3390/ijms18030538).
- [3] C. Lawson et al. “Microvesicles and exosomes: New players in metabolic and cardiovascular disease.” In: *J. Endocrinol.* 228.2 (2016), R57–R71. ISSN: 14796805. DOI: [10.1530/JOE-15-0201](https://doi.org/10.1530/JOE-15-0201).
- [4] C. Ciardiello et al. “Focus on extracellular vesicles: New frontiers of cell-to-cell communication in cancer.” In: *Int. J. Mol. Sci.* 17.2 (2016), pp. 1–17. ISSN: 14220067. DOI: [10.3390/ijms17020175](https://doi.org/10.3390/ijms17020175).
- [5] J. C. Contreras-Naranjo, H. J. Wu, and V.M. Ugaz. “Microfluidics for exosome isolation and analysis: Enabling liquid biopsy for personalized medicine.” In: *Lab Chip* 17.21 (2017), pp. 3558–3577. ISSN: 14730189. DOI: [10.1039/c71c00592j](https://doi.org/10.1039/c71c00592j).
- [6] N. Kosaka et al. “Competitive interactions of cancer cells and normal cells via secretory microRNAs.” In: *J. Biol. Chem.* 287.2 (2012), pp. 1397–1405. ISSN: 00219258. DOI: [10.1074/jbc.M111.288662](https://doi.org/10.1074/jbc.M111.288662).
- [7] A. Hoshino et al. “Tumour exosome integrins determine organotropic metastasis.” In: *Nature* 527.7578 (2015), pp. 329–335. ISSN: 14764687. DOI: [10.1038/nature15756](https://doi.org/10.1038/nature15756).
- [8] Li Li Yu et al. “A Comparison of Traditional and Novel Methods for the Separation of Exosomes from Human Samples.” In: *Biomed Res. Int.* 2018 (2018). ISSN: 23146141. DOI: [10.1155/2018/3634563](https://doi.org/10.1155/2018/3634563).
- [9] C. Théry et al. “Isolation and Characterization of Exosomes from Cell Culture Supernatants.” In: *Curr. Protoc. Cell Biol.* (2006), 30:3.22:3.22.1–3.22.29.
- [10] D. K. Jeppesen et al. “Comparative analysis of discrete exosome fractions obtained by differential centrifugation.” In: *J. Extracell. Vesicles* 3.1 (2014), pp. 1–16. ISSN: 20013078. DOI: [10.3402/jev.v3.25011](https://doi.org/10.3402/jev.v3.25011).

- [11] T. Salafi, K.K. Zeming, and Y. Zhang. “Advancements in microfluidics for nanoparticle separation.” In: *Lab Chip* 17.1 (2017), pp. 11–33. ISSN: 14730189. DOI: [10.1039/C6LC01045H](https://doi.org/10.1039/C6LC01045H).
- [12] W. Zhang et al. “Magnetic and Folate Functionalization Enables Rapid Isolation and Enhanced Tumor-Targeting of Cell-Derived Microvesicles.” In: *ACS Nano* 11.1 (2017), pp. 277–290. ISSN: 1936086X. DOI: [10.1021/acsnano.6b05630](https://doi.org/10.1021/acsnano.6b05630).
- [13] R. Szatanek et al. “Isolation of extracellular vesicles: Determining the correct approach (review).” In: *Int. J. Mol. Med.* 36.1 (2015), pp. 11–17. ISSN: 1791244X. DOI: [10.3892/ijmm.2015.2194](https://doi.org/10.3892/ijmm.2015.2194).
- [14] Frank A.W. Coumans et al. “Methodological guidelines to study extracellular vesicles.” In: *Circ. Res.* 120.10 (2017), pp. 1632–1648. ISSN: 15244571. DOI: [10.1161/CIRCRESAHA.117.309417](https://doi.org/10.1161/CIRCRESAHA.117.309417).
- [15] P. Sajeesh and A. K. Sen. “Particle separation and sorting in microfluidic devices: A review.” In: *Microfluid. Nanofluidics* 17.1 (2014), pp. 1–52. ISSN: 16134990. DOI: [10.1007/s10404-013-1291-9](https://doi.org/10.1007/s10404-013-1291-9).
- [16] R.T. Davies et al. “Microfluidic filtration system to isolate extracellular vesicles from blood.” In: *Lab Chip* 12.24 (2012), pp. 5202–5210. ISSN: 14730189. DOI: [10.1039/c2lc41006k](https://doi.org/10.1039/c2lc41006k).
- [17] L. G. Liang et al. “An integrated double-filtration microfluidic device for isolation, enrichment and quantification of urinary extracellular vesicles for detection of bladder cancer.” In: *Sci. Rep.* 7.March (2017), pp. 1–10. ISSN: 20452322. DOI: [10.1038/srep46224](https://doi.org/10.1038/srep46224).
- [18] F. Liu et al. “The Exosome Total Isolation Chip.” In: *ACS Nano* 11.11 (2017), pp. 10712–10723. ISSN: 1936086X. DOI: [10.1021/acsnano.7b04878](https://doi.org/10.1021/acsnano.7b04878).
- [19] A. A. S. Bhagat, S. S. Kuntaegowdanahalli, and I. Papautsky. “Continuous particle separation in spiral microchannels using dean flows and differential migration.” In: *Lab Chip* 8.11 (2008), pp. 1906–1914. ISSN: 14730189. DOI: [10.1039/b807107a](https://doi.org/10.1039/b807107a).
- [20] W. Lee et al. “3D-Printed micro fluidic device for the detection of pathogenic bacteria using size-based separation in helical channel with trapezoid cross-section.” In: *Sci. Rep.* 5 (2015), pp. 1–6. ISSN: 20452322. DOI: [10.1038/srep07717](https://doi.org/10.1038/srep07717).
- [21] Z. Liu et al. “High throughput capture of circulating tumor cells using an integrated microfluidic system.” In: *Biosens. Bioelectron.* 47 (2013), pp. 113–119. ISSN: 09565663. DOI: [10.1016/j.bios.2013.03.017](https://doi.org/10.1016/j.bios.2013.03.017).
- [22] D. W. Inglis, N. Herman, and G. Vesey. “Highly accurate deterministic lateral displacement device and its application to purification of fungal spores.” In: *Biomecrofluidics* 4.2 (2010). ISSN: 19321058. DOI: [10.1063/1.3430553](https://doi.org/10.1063/1.3430553).

- [23] J. A. Davis et al. "Deterministic hydrodynamics: Taking blood apart." In: *Proc. Natl. Acad. Sci. U. S. A.* 103.40 (2006), pp. 14779–14784. ISSN: 00278424. DOI: [10.1073/pnas.0605967103](https://doi.org/10.1073/pnas.0605967103).
- [24] N. Tottori et al. "Separation of viable and nonviable mammalian cells using a deterministic lateral displacement microfluidic device." In: *Biomicrofluidics* 10.1 (2016). ISSN: 19321058. DOI: [10.1063/1.4942948](https://doi.org/10.1063/1.4942948).
- [25] S. Ranjan et al. "DLD pillar shape design for efficient separation of spherical and non-spherical bioparticles." In: *Lab Chip* 14.21 (2014), pp. 4250–4262. ISSN: 14730189. DOI: [10.1039/c4lc00578c](https://doi.org/10.1039/c4lc00578c).
- [26] J. McGrath, M. Jimenez, and H. Bridle. "Deterministic lateral displacement for particle separation: A review." In: *Lab Chip* 14.21 (2014), pp. 4139–4158. ISSN: 14730189. DOI: [10.1039/c4lc00939h](https://doi.org/10.1039/c4lc00939h).
- [27] L. R. Huang et al. "Continuous Particle Separation Through Deterministic Lateral Displacement." In: *Science (80-.)*, 304.5673 (2004), pp. 987–990. ISSN: 00368075. DOI: [10.1126/science.1094567](https://doi.org/10.1126/science.1094567).
- [28] D.W. Inglis et al. "Critical particle size for fractionation by deterministic lateral displacement." In: *Lab Chip* 6.5 (2006), pp. 655–658. ISSN: 14730189. DOI: [10.1039/b515371a](https://doi.org/10.1039/b515371a).
- [29] Z. Wang et al. "Ciliated micropillars for the microfluidic-based isolation of nanoscale lipid vesicles." In: *Lab Chip* 13.15 (2013), pp. 2879–2882. ISSN: 14730189. DOI: [10.1039/c3lc41343h](https://doi.org/10.1039/c3lc41343h).
- [30] S.M. Santana et al. "Microfluidic isolation of cancer-cell-derived microvesicles from heterogeneous extracellular shed vesicle populations." In: *Biomed. Microdevices* 16.6 (2014), pp. 869–877. ISSN: 15728781. DOI: [10.1007/s10544-014-9891-z](https://doi.org/10.1007/s10544-014-9891-z).
- [31] B. H. Wunsch et al. "Nanoscale lateral displacement arrays for the separation of exosomes and colloids down to 20nm." In: *Nat. Nanotechnol.* 11.11 (2016), pp. 936–940. ISSN: 17483395. DOI: [10.1038/nnano.2016.134](https://doi.org/10.1038/nnano.2016.134).
- [32] J. E. Kim, J. H. Cho, and S. H. Paek. "Functional membrane-implanted lab-on-a-chip for analysis of percent HDL cholesterol." In: *Anal. Chem.* 77.24 (2005), pp. 7901–7907. ISSN: 00032700. DOI: [10.1021/ac0510484](https://doi.org/10.1021/ac0510484).
- [33] J. Moorthy and D. J. Beebe. "In situ fabricated porous filters for microsystems." In: *Lab Chip* 3.2 (2003), pp. 62–66. ISSN: 14730189. DOI: [10.1039/b300450c](https://doi.org/10.1039/b300450c).
- [34] T. A. Crowley and V. Pizziconi. "Isolation of plasma from whole blood using planar microfilters for lab-on-a-chip applications." In: *Lab Chip* 5.9 (2005), pp. 922–929. ISSN: 14730189. DOI: [10.1039/b502930a](https://doi.org/10.1039/b502930a).

- [35] F. v. d. Kammer et al. "Separation and characterization of nanoparticles in complex food and environmental samples by field-flow fractionation." In: *TrAC - Trends Anal. Chem.* 30.3 (2011), pp. 425–436. ISSN: 01659936. DOI: [10.1016/j.trac.2010.11.012](https://doi.org/10.1016/j.trac.2010.11.012).
- [36] Fathi A. Messaud et al. "An overview on field-flow fractionation techniques and their applications in the separation and characterization of polymers." In: *Prog. Polym. Sci.* 34.4 (2009), pp. 351–368. ISSN: 00796700. DOI: [10.1016/j.progpolymsci.2008.11.001](https://doi.org/10.1016/j.progpolymsci.2008.11.001).
- [37] P. Arosio et al. "Density-gradient-free microfluidic centrifugation for analytical and preparative separation of nanoparticles." In: *Nano Lett.* 14.5 (2014), pp. 2365–2371. ISSN: 15306992. DOI: [10.1021/nl404771g](https://doi.org/10.1021/nl404771g).
- [38] A. Ashkin. "Acceleration and Trapping of Particles by Radiation Pressure." In: *Phys. Rev. Lett.* 24.4 (1970), pp. 156–159. ISSN: 00319007. DOI: [10.1103/PhysRevLett.24.156](https://doi.org/10.1103/PhysRevLett.24.156).
- [39] S. S. Kanwar et al. "Microfluidic device (ExoChip) for on-chip isolation, quantification and characterization of circulating exosomes." In: *Lab Chip* 14.11 (2014), pp. 1891–1900. ISSN: 14730189. DOI: [10.1039/c4lc00136b](https://doi.org/10.1039/c4lc00136b).
- [40] M. Ebara et al. "A photoinduced nanoparticle separation in microchannels via pH-sensitive surface traps." In: *Langmuir* 29.18 (2013), pp. 5388–5393. ISSN: 07437463. DOI: [10.1021/la400347r](https://doi.org/10.1021/la400347r).
- [41] X. Huang et al. "Microfluidic chip-based one-step fabrication of an artificial photosystem i for photocatalytic cofactor regeneration." In: *RSC Adv.* 6.104 (2016), pp. 101974–101980. ISSN: 20462069. DOI: [10.1039/c6ra21390a](https://doi.org/10.1039/c6ra21390a).
- [42] R. T. Turgeon and M.T. Bowser. "Micro free-flow electrophoresis: Theory and applications." In: *Anal. Bioanal. Chem.* 394.1 (2009), pp. 187–198. ISSN: 16182642. DOI: [10.1007/s00216-009-2656-5](https://doi.org/10.1007/s00216-009-2656-5).
- [43] H. Jeon, Y. Kim, and G. Lim. "Continuous particle separation using pressure-driven flow-induced miniaturizing free-flow electrophoresis (PDF-induced μ -FFE)." In: *Sci. Rep.* 6.January (2016), pp. 1–9. ISSN: 20452322. DOI: [10.1038/srep19911](https://doi.org/10.1038/srep19911).
- [44] F. Barbaresco et al. "Application of a Micro Free-Flow Electrophoresis 3D Printed Lab-on-a-Chip for Micro-Nanoparticles Analysis." In: (2020).
- [45] S. Dash et al. "CFD design of a microfluidic device for continuous dielectrophoretic separation of charged gold nanoparticles." In: *J. Taiwan Inst. Chem. Eng.* 58 (2016), pp. 39–48. ISSN: 18761070. DOI: [10.1016/j.jtice.2015.05.034](https://doi.org/10.1016/j.jtice.2015.05.034).
- [46] N. G. Green and H. Morgan. "Separation of submicrometre particles using a combination of dielectrophoretic and electrohydrodynamic forces." In: *J. Phys. D. Appl. Phys.* 31.7 (1998). ISSN: 00223727. DOI: [10.1088/0022-3727/31/7/002](https://doi.org/10.1088/0022-3727/31/7/002).

- [47] A. Lenshof et al. "Acoustofluidics 5: Building microfluidic acoustic resonators." In: *Lab Chip* 12.4 (2012), pp. 684–695. ISSN: 14730189. DOI: [10.1039/c11c20996e](https://doi.org/10.1039/c11c20996e).
- [48] Leo L. Beranek. *Handbook of Acoustics*. Vol. 77. 12. 2009, pp. 1197–1197. ISBN: 9781493907557. DOI: [10.1119/1.3197171](https://doi.org/10.1119/1.3197171).
- [49] T. Laurell, F. Petersson, and A. Nilsson. "Chip integrated strategies for acoustic separation and manipulation of cells and particles." In: *Chem. Soc. Rev.* 36.3 (2007), pp. 492–506. ISSN: 14604744. DOI: [10.1039/b601326k](https://doi.org/10.1039/b601326k).
- [50] A. Lenshof, C. Magnusson, and T. Laurell. "Acoustofluidics 8: Applications of acoustophoresis in continuous flow microsystems." In: *Lab Chip* 12.7 (2012), pp. 1210–1223. ISSN: 14730189. DOI: [10.1039/c21c21256k](https://doi.org/10.1039/c21c21256k).
- [51] N. R. Harris et al. "A silicon microfluidic ultrasonic separator." In: *Sensors Actuators, B Chem.* 95.1-3 (2003), pp. 425–434. ISSN: 09254005. DOI: [10.1016/S0925-4005\(03\)00448-9](https://doi.org/10.1016/S0925-4005(03)00448-9).
- [52] A. Nilsson et al. "Acoustic control of suspended particles in micro fluidic chips." In: *Lab Chip* 4.2 (2004), pp. 131–135. ISSN: 14730197. DOI: [10.1039/b313493h](https://doi.org/10.1039/b313493h).
- [53] J. Shi et al. "Focusing microparticles in a microfluidic channel with standing surface acoustic waves (SSAW)." In: *Lab Chip* 8.2 (2008), pp. 221–223. ISSN: 14730189. DOI: [10.1039/b716321e](https://doi.org/10.1039/b716321e).
- [54] K. Yasuda, S.I. Umemura, and K. Takeda. "Concentration and fractionation of small particles in liquid by ultrasound." In: *Jpn. J. Appl. Phys.* 34.5S (1995), pp. 2715–2720. ISSN: 13474065. DOI: [10.1143/JJAP.34.2715](https://doi.org/10.1143/JJAP.34.2715).
- [55] K. Yasuda et al. "Using acoustic radiation force as a concentration method for erythrocytes." In: *J. Acoust. Soc. Am.* 102.1 (1997), pp. 642–645. ISSN: 0001-4966. DOI: [10.1121/1.421009](https://doi.org/10.1121/1.421009).
- [56] N. R. Harris et al. "Performance of a micro-engineered ultrasonic particle manipulator." In: *Sensors Actuators, B Chem.* 111-112.SUPPL. (2005), pp. 481–486. ISSN: 09254005. DOI: [10.1016/j.snb.2005.03.036](https://doi.org/10.1016/j.snb.2005.03.036).
- [57] M. Wiklund et al. "Ultrasonic standing wave manipulation technology integrated into a dielectrophoretic chip." In: *Lab Chip* 6.12 (2006), pp. 1537–1544. ISSN: 14730189. DOI: [10.1039/b612064b](https://doi.org/10.1039/b612064b).
- [58] A. Lenshof et al. "Acoustic whole blood plasmapheresis chip for prostate specific antigen microarray diagnostics." In: *Anal. Chem.* 81.15 (2009), pp. 6030–6037. ISSN: 00032700. DOI: [10.1021/ac9013572](https://doi.org/10.1021/ac9013572).
- [59] M. Kumar, D. L. Feke, and J. M. Belovich. "Fractionation of cell mixtures using acoustic and laminar flow fields." In: *Biotechnol. Bioeng.* 89.2 (2005), pp. 129–137. ISSN: 00063592. DOI: [10.1002/bit.20294](https://doi.org/10.1002/bit.20294).

- [60] P. Augustsson et al. "Iso-acoustic focusing of cells for size-insensitive acousto-mechanical phenotyping." In: *Nat. Commun.* 7.May (2016), pp. 1–9. ISSN: 20411723. DOI: [10.1038/ncomms11556](https://doi.org/10.1038/ncomms11556).
- [61] F. Petersson et al. "Continuous separation of lipid particles from erythrocytes by means of laminar flow and acoustic standing wave forces." In: *Lab Chip* 5.1 (2005), pp. 20–22. ISSN: 14730197. DOI: [10.1039/b405748c](https://doi.org/10.1039/b405748c).
- [62] F. Petersson et al. "Separation of lipids from blood utilizing ultrasonic standing waves in microfluidic channels." In: *Analyst* 129.10 (2004), pp. 938–943. ISSN: 00032654. DOI: [10.1039/b409139f](https://doi.org/10.1039/b409139f).
- [63] Hina Kalra et al. "Comparative proteomics evaluation of plasma exosome isolation techniques and assessment of the stability of exosomes in normal human blood plasma." In: *Proteomics* 13.22 (2013), pp. 3354–3364. ISSN: 16159853. DOI: [10.1002/pmic.201300282](https://doi.org/10.1002/pmic.201300282).
- [64] M. L. Alvarez et al. "Comparison of protein, microRNA, and mRNA yields using different methods of urinary exosome isolation for the discovery of kidney disease biomarkers." In: *Kidney Int.* 82.9 (2012), pp. 1024–1032. ISSN: 15231755. DOI: [10.1038/ki.2012.256](https://doi.org/10.1038/ki.2012.256).
- [65] H. Bruus. "Theoretical Microfluidics (Oxford Master Series in Physics)." In: 18 (2007). ISSN: 19454589. DOI: [10.1017/CBO9781107415324.004](https://doi.org/10.1017/CBO9781107415324.004). arXiv: [arXiv: 1011.1669v3](https://arxiv.org/abs/1011.1669v3).
- [66] S. Kim and S. J. Karrila. "Microhydrodynamic Phenomena." In: *Microhydrodynamics* (1991), pp. 1–12. DOI: [10.1016/b978-0-7506-9173-4.50007-4](https://doi.org/10.1016/b978-0-7506-9173-4.50007-4).
- [67] W.E. Bird, R. B. Stewart and E. N. Lightfoot. *Transport phenomena (2nd ed.)* John Wiley & Sons, Inc., 2001, p. 912. ISBN: 978-81-265-0808-2.
- [68] M. Rieutord. *Fluid dynamics*. Vol. 7. 2. 2015, pp. 55–58. ISBN: 9783319093505.
- [69] J. C. Svendsen and E. Winnie. *Lab-on-a-Chip Devices and Micro-Total Analysis Systems*. 2015. ISBN: 9783319086866. DOI: [10.1007/978-3-319-08687-3](https://doi.org/10.1007/978-3-319-08687-3).
- [70] C. L. Hansen et al. "A robust and scalable microfluidic metering method that allows protein crystal growth by free interface diffusion." In: *Proc. Natl. Acad. Sci. U. S. A.* 99.26 (2002), pp. 16531–16536. ISSN: 00278424. DOI: [10.1073/pnas.262485199](https://doi.org/10.1073/pnas.262485199).
- [71] N. Convery and N. Gadegaard. "30 Years of Microfluidics." In: *Micro Nano Eng.* 2.May 2018 (2019), pp. 76–91. ISSN: 25900072. DOI: [10.1016/j.mne.2019.01.003](https://doi.org/10.1016/j.mne.2019.01.003).
- [72] Chia Yen Lee et al. "Microfluidic mixing: A review." In: *Int. J. Mol. Sci.* 12.5 (2011), pp. 3263–3287. ISSN: 14220067. DOI: [10.3390/ijms12053263](https://doi.org/10.3390/ijms12053263).

-
- [73] F. Moukalled, L. Mangani, and M. Darwish. *The finite volume method in computational fluid dynamics : An Advanced Introduction with OpenFOAM and Matlab*. Vol. 113. 2016, E1. ISBN: 9783319168739.
- [74] J. T. Karlsen. “Theory of nonlinear acoustic forces acting on fluids and particles in microsystems.” PhD thesis. 2018, p. 174.
- [75] J. T. Karlsen et al. “Acoustic Streaming and Its Suppression in Inhomogeneous Fluids.” In: *Phys. Rev. Lett.* 120.5 (2018), p. 54501. ISSN: 10797114. DOI: [10.1103/PhysRevLett.120.054501](https://doi.org/10.1103/PhysRevLett.120.054501). arXiv: [1707.07369](https://arxiv.org/abs/1707.07369).
- [76] A. S. Dukhin and P.J. Goetz. “Bulk viscosity and compressibility measurement using acoustic spectroscopy.” In: *J. Chem. Phys.* 130.12 (2009). ISSN: 00219606. DOI: [10.1063/1.3095471](https://doi.org/10.1063/1.3095471).
- [77] P.S. Epstein and R. R. Carhart. “The Absorption of Sound in Suspensions and Emulsions. I. Water Fog in Air.” In: *J. Acoust. Soc. Am.* 25.3 (1953), pp. 553–565. ISSN: NA. DOI: [10.1121/1.1907107](https://doi.org/10.1121/1.1907107).
- [78] J. R. Allegra and S. A. Hawley. “Attenuation of Sound in Suspensions and Emulsions: Theory and Experiments.” In: *J. Acoust. Soc. Am.* 51.5B (1972), pp. 1545–1564. ISSN: NA. DOI: [10.1121/1.1912999](https://doi.org/10.1121/1.1912999).
- [79] L. D. Landau and E. M. Lifshitz. *Course of Theoretical Physics*. 1987. DOI: [10.1007/b138775](https://doi.org/10.1007/b138775). arXiv: [1003.3921v1](https://arxiv.org/abs/1003.3921v1).
- [80] H. Bruus. “Acoustofluidics 2: Perturbation theory and ultrasound resonance modes.” In: *Lab Chip* 12.1 (2012), pp. 20–28. ISSN: 14730189. DOI: [10.1039/c1lc20770a](https://doi.org/10.1039/c1lc20770a).
- [81] J. Lighthill. “Acoustic Streaming.” In: *J. Sound Vib.* 61.3 (1978), p. 391418.
- [82] M.W. H. Ley. “Effective modelling of acoustofluidic devices.” PhD thesis. 2017.
- [83] P. B. Muller et al. “Ultrasound-induced acoustophoretic motion of microparticles in three dimensions.” In: *Phys. Rev. E - Stat. Nonlinear, Soft Matter Phys.* 88.2 (2013), pp. 1–12. ISSN: 15393755. DOI: [10.1103/PhysRevE.88.023006](https://doi.org/10.1103/PhysRevE.88.023006).
- [84] P. B. Muller et al. “A numerical study of microparticle acoustophoresis driven by acoustic radiation forces and streaming-induced drag forces.” In: *Lab Chip* 12.22 (2012), pp. 4617–4627. ISSN: 14730189. DOI: [10.1039/c2lc40612h](https://doi.org/10.1039/c2lc40612h).
- [85] M. Wiklund, R. Green, and M. Ohlin. “Acoustofluidics 14 : Applications of acoustic streaming in microfluidic devices.” In: (2012), pp. 2438–2451. DOI: [10.1039/c2lc40203c](https://doi.org/10.1039/c2lc40203c).
- [86] M. Faraday. “On a peculiar class of acoustical figures; and on certain forms assumed by groups of particles upon vibrating elastic surfaces.” In: *Philos. Trans. R. Soc. London* 121.January (1831), pp. 299–340. ISSN: 0261-0523. DOI: [10.1098/rstl.1831.0018](https://doi.org/10.1098/rstl.1831.0018).

- [87] Lord Rayleigh. “On the circulation of air observed in Kundt’s tubes, and on some allied acoustical problems.” In: *Philosophical Trans.* (1884), pp. 1–21. DOI: <https://doi.org/10.1098/rstl.1884.0002>.
- [88] H. Bruus. “Acoustofluidics 7: The acoustic radiation force on small particles.” In: *Lab Chip* 12.6 (2012), pp. 1014–1021. ISSN: 14730189. DOI: [10.1039/c2lc21068a](https://doi.org/10.1039/c2lc21068a).
- [89] M. Settnes and H. Bruus. “Forces acting on a small particle in an acoustical field in a viscous fluid.” In: *Phys. Rev. E - Stat. Nonlinear, Soft Matter Phys.* 85.1 (2012), pp. 1–12. ISSN: 15393755. DOI: [10.1103/PhysRevE.85.016327](https://doi.org/10.1103/PhysRevE.85.016327). arXiv: [1110.6037](https://arxiv.org/abs/1110.6037).
- [90] J.T. Karlsen and H. Bruus. “Forces acting on a small particle in an acoustical field in a thermoviscous fluid.” In: *Phys. Rev. E - Stat. Nonlinear, Soft Matter Phys.* 92.4 (2015). ISSN: 15502376. DOI: [10.1103/PhysRevE.92.043010](https://doi.org/10.1103/PhysRevE.92.043010).
- [91] R. Barnkob et al. “Measuring the local pressure amplitude in microchannel acoustophoresis.” In: *Lab Chip* 10.5 (2010), pp. 563–570. ISSN: 14730189. DOI: [10.1039/b920376a](https://doi.org/10.1039/b920376a).
- [92] P. Augustsson et al. “Automated and temperature-controlled micro-PIV measurements enabling long-term-stable microchannel acoustophoresis characterization.” In: *Lab Chip* 11.24 (2011), pp. 4152–4164. ISSN: 14730189. DOI: [10.1039/c1lc20637k](https://doi.org/10.1039/c1lc20637k).
- [93] C. Grenvall et al. “Harmonic microchip acoustophoresis: A route to online raw milk sample precondition in protein and lipid content quality control.” In: *Anal. Chem.* 81.15 (2009), pp. 6195–6200. ISSN: 00032700. DOI: [10.1021/ac900723q](https://doi.org/10.1021/ac900723q).
- [94] C. W. Shields et al. “Elastomeric negative acoustic contrast particles for capture, acoustophoretic transport, and confinement of cells in microfluidic systems.” In: *Langmuir* 30.14 (2014), pp. 3923–3927. ISSN: 15205827. DOI: [10.1021/la404677w](https://doi.org/10.1021/la404677w).
- [95] W. Qiu et al. “Experimental Characterization of Acoustic Streaming in Gradients of Density and Compressibility.” In: *Phys. Rev. Appl.* 11.2 (2019), p. 1. ISSN: 23317019. DOI: [10.1103/PhysRevApplied.11.024018](https://doi.org/10.1103/PhysRevApplied.11.024018).
- [96] J. T. Karlsen, P. Augustsson, and H. Bruus. “Acoustic Force Density Acting on Inhomogeneous Fluids in Acoustic Fields.” In: *Phys. Rev. Lett.* 117.11 (2016), pp. 0–6. ISSN: 10797114. DOI: [10.1103/PhysRevLett.117.114504](https://doi.org/10.1103/PhysRevLett.117.114504). arXiv: [1605.06089](https://arxiv.org/abs/1605.06089).
- [97] S. Deshmukh et al. “Acoustic radiation forces at liquid interfaces impact the performance of acoustophoresis.” In: *Lab Chip* 14.17 (2014), pp. 3394–3400. ISSN: 14730189. DOI: [10.1039/c4lc00572d](https://doi.org/10.1039/c4lc00572d).
- [98] *Detailed Explanation of the Finite Element Method (FEM)*. (Visited on 10/13/2020).

-
- [99] M. Putti. “Dispense del corso di Metodi Numerici per l’Ingegneria Appunti di teoria sul Metodo agli Elementi Finiti (FEM).” In: (2011), pp. 1–48.
- [100] A. H. Siddiqi et al. *Applied Partial Differential Equations*. 2018, pp. 389–443. ISBN: 9783319124926. DOI: [10.1201/9781315157153-5](https://doi.org/10.1201/9781315157153-5).
- [101] P.B. Muller. “Acoustic streaming in microchannels.” In: *Thesis* September (2015). ISSN: 00346861.
- [102] J.H. Ferziger, P. Milovan, and R. L. Street. *Computational Methods for Fluid Dynamics*. Springer, Cham, 2020, pp. 81–110. ISBN: 978-3-319-99693-6. DOI: <https://doi.org/10.1007/978-3-319-99693-6>.
- [103] H. K. Versteeg and W. Malalasekera. *An Introduction to Computational Fluid Dynamics - The Finite Volume Method*. 2nd. Pearson Education Limited, 2007. ISBN: 9780131274983. arXiv: [arXiv:1011.1669v3](https://arxiv.org/abs/1011.1669v3).
- [104] Prerna Balyan et al. “Flow induced particle separation and collection through linear array pillar microfluidics device.” In: *Biomicrofluidics* 14.2 (2020). ISSN: 19321058. DOI: [10.1063/1.5143656](https://doi.org/10.1063/1.5143656).
- [105] Tae Goo Kang et al. “A continuous flow micro filtration device for plasma/blood separation using submicron vertical pillar gap structures.” In: *J. Micromechanics Microengineering* 24.8 (2014). ISSN: 13616439. DOI: [10.1088/0960-1317/24/8/087001](https://doi.org/10.1088/0960-1317/24/8/087001).
- [106] Xing Chen et al. “Microfluidic chip for blood cell separation and collection based on crossflow filtration.” In: *Sensors Actuators, B Chem.* 130.1 (2008), pp. 216–221. ISSN: 09254005. DOI: [10.1016/j.snb.2007.07.126](https://doi.org/10.1016/j.snb.2007.07.126).
- [107] L. Spigarelli et al. “A passive two-way microfluidic device for low volume blood-plasma separation.” In: *Microelectron. Eng.* 209.November 2018 (2019), pp. 28–34. ISSN: 01679317. DOI: [10.1016/j.mee.2019.02.011](https://doi.org/10.1016/j.mee.2019.02.011).
- [108] S. Yang, A. Ündar, and J. D. Zahn. “A microfluidic device for continuous, real time blood plasma separation.” In: *Lab Chip* 6.7 (June 2006), pp. 871–880. ISSN: 14730189. DOI: [10.1039/b516401j](https://doi.org/10.1039/b516401j).
- [109] S. Aachboun and P. Ranson. “Deep anisotropic etching of silicon.” In: *J. Vac. Sci. Technol. A Vacuum, Surfaces, Film.* 17.4 (July 1999), pp. 2270–2273. ISSN: 0734-2101. DOI: [10.1116/1.581759](https://doi.org/10.1116/1.581759).
- [110] V. Bertana et al. “3D-printed microfluidics on thin poly(methyl methacrylate) substrates for genetic applications.” In: *J. Vac. Sci. Technol. B, Nanotechnol. Microelectron. Mater. Process. Meas. Phenom.* 36.1 (2018), 01A106. ISSN: 2166-2746. DOI: [10.1116/1.5003203](https://doi.org/10.1116/1.5003203).
- [111] A. Lenshof and T. Laurell. “Continuous separation of cells and particles in microfluidic systems.” In: *Chem. Soc. Rev.* 39.3 (2010), pp. 1203–1217. ISSN: 03060012. DOI: [10.1039/b915999c](https://doi.org/10.1039/b915999c).

- [112] L. Spigarelli et al. “Numerical study of the effect of channel aspect ratio on particle focusing in acoustophoretic devices.” In: *Sci. Rep.* 0123456789 (2020), pp. 1–11. ISSN: 2045-2322. DOI: [10.1038/s41598-020-76367-w](https://doi.org/10.1038/s41598-020-76367-w).
- [113] J. Dual and T. Schwarz. “Acoustofluidics 3: Continuum mechanics for ultrasonic particle manipulation.” In: *Lab Chip* 12.2 (2012), pp. 244–252. ISSN: 14730189. DOI: [10.1039/c11c20837c](https://doi.org/10.1039/c11c20837c).
- [114] P. B. Muller and H. Bruus. “Numerical study of thermoviscous effects in ultrasound-induced acoustic streaming in microchannels.” In: *Phys. Rev. E - Stat. Nonlinear, Soft Matter Phys.* 90.4 (2014), pp. 1–12. ISSN: 15502376. DOI: [10.1103/PhysRevE.90.043016](https://doi.org/10.1103/PhysRevE.90.043016). arXiv: [1408.4970](https://arxiv.org/abs/1408.4970).
- [115] J. van ’t Oever et al. “Numerical study of submicroparticle acoustophoresis using higher-order modes in a rectangular microchannel.” In: *J. Sound Vib.* 415 (2018), pp. 169–183. ISSN: 10958568. DOI: [10.1016/j.jsv.2017.11.012](https://doi.org/10.1016/j.jsv.2017.11.012).
- [116] M. Antfolk et al. “Focusing of sub-micrometer particles and bacteria enabled by two-dimensional acoustophoresis.” In: *Lab Chip* 14.15 (Aug. 2014), pp. 2791–2799. ISSN: 14730189. DOI: [10.1039/c41c00202d](https://doi.org/10.1039/c41c00202d).
- [117] M. Hoyos and A. Castro. “Controlling the acoustic streaming by pulsed ultrasounds.” In: *Ultrasonics* 53.1 (Jan. 2013), pp. 70–76. ISSN: 0041624X. DOI: [10.1016/j.ultras.2012.03.015](https://doi.org/10.1016/j.ultras.2012.03.015).
- [118] J. S. Bach and H. Bruus. “Suppression of Acoustic Streaming in Shape-Optimized Channels.” In: *Phys. Rev. Lett.* 124.21 (May 2020), p. 214501. ISSN: 10797114. DOI: [10.1103/PhysRevLett.124.214501](https://doi.org/10.1103/PhysRevLett.124.214501). arXiv: [2002.11058](https://arxiv.org/abs/2002.11058).
- [119] W. Wagner and A. Pruß. “The IAPWS formulation 1995 for the thermodynamic properties of ordinary water substance for general and scientific use.” In: *J. Phys. Chem. Ref. Data* 31.2 (June 2002), pp. 387–535. ISSN: 00472689. DOI: [10.1063/1.1461829](https://doi.org/10.1063/1.1461829).
- [120] M. L. Huber et al. “New international formulation for the viscosity of H₂O.” In: *J. Phys. Chem. Ref. Data* 38.2 (Apr. 2009), pp. 101–125. ISSN: 00472689. DOI: [10.1063/1.3088050](https://doi.org/10.1063/1.3088050).
- [121] J. Holmes, G. Parker, and W. Povey. “Temperature dependence of bulk viscosity in water using acoustic spectroscopy.” In: *J. Phys. Conf. Ser.* Vol. 269. 1. Institute of Physics Publishing, Jan. 2011, p. 012011. DOI: [10.1088/1742-6596/269/1/012011](https://doi.org/10.1088/1742-6596/269/1/012011).
- [122] M. L. Huber et al. “New International Formulation for the Thermal Conductivity of H₂O.” In: *J. Phys. Chem. Ref. Data* 41.3 (July 2012), p. 033102. ISSN: 00472689. DOI: [10.1063/1.4738955](https://doi.org/10.1063/1.4738955).
- [123] R. Kono. “The Dynamic Bulk Viscosity of Polystyrene and Polymethyl Methacrylate.” In: *J. Phys. Soc. Japan* 15.4 (Dec. 1960), pp. 718–725. ISSN: 13474073. DOI: [10.1143/JPSJ.15.718](https://doi.org/10.1143/JPSJ.15.718).

- [124] E. S. Domalski and E. D. Hearing. "Heat Capacities and Entropies of Organic Compounds in the Condensed Phase. Volume III." In: *J. Phys. Chem. Ref. Data* 25.1 (Jan. 1996), pp. 1–525. ISSN: 00472689. DOI: [10.1063/1.555985](https://doi.org/10.1063/1.555985).
- [125] J. Chiu and P. G. Fair. "Determination of thermal conductivity by differential scanning calorimetry." In: *Thermochim. Acta* 34.2 (Dec. 1979), pp. 267–273. ISSN: 00406031. DOI: [10.1016/0040-6031\(79\)87116-6](https://doi.org/10.1016/0040-6031(79)87116-6).
- [126] J. Lei, P. Glynne-Jones, and M. Hill. "Acoustic streaming in the transducer plane in ultrasonic particle manipulation devices." In: *Lab Chip* 13.11 (2013), pp. 2133–2143. ISSN: 14730189. DOI: [10.1039/c3lc00010a](https://doi.org/10.1039/c3lc00010a).
- [127] J. Lei, M. Hill, and P. Glynne-Jones. "Numerical simulation of 3D boundary-driven acoustic streaming in microfluidic devices." In: *Lab Chip* 14.3 (2014), pp. 532–541. ISSN: 14730189. DOI: [10.1039/c3lc50985k](https://doi.org/10.1039/c3lc50985k).
- [128] W. L. Nyborg. "Acoustic Streaming near a Boundary." In: *J. Acoust. Soc. Am.* 30.4 (Apr. 1958), pp. 329–339. ISSN: NA. DOI: [10.1121/1.1909587](https://doi.org/10.1121/1.1909587).
- [129] Davood Saeidi et al. "A quantitative study of the secondary acoustic radiation force on biological cells during acoustophoresis." In: *Micromachines* 11.2 (2020). ISSN: 2072666X. DOI: [10.3390/mi11020152](https://doi.org/10.3390/mi11020152).
- [130] J.T. Karlsen and H. Bruus. "Acoustic Tweezing and Patterning of Concentration Fields in Microfluidics." In: *Phys. Rev. Appl.* 7.3 (2017), pp. 1–10. ISSN: 23317019. DOI: [10.1103/PhysRevApplied.7.034017](https://doi.org/10.1103/PhysRevApplied.7.034017).
- [131] G. P. Gautam et al. "Separation of sub-micron particles from micron particles using acoustic fluid relocation combined with acoustophoresis." In: *Anal. Bioanal. Chem.* 410.25 (2018), pp. 6561–6571. ISSN: 16182650. DOI: [10.1007/s00216-018-1261-x](https://doi.org/10.1007/s00216-018-1261-x).
- [132] E. S. Shurkhina et al. "Detection of stages of autoimmune hemolytic anemia by evaluating erythrocyte deformability and density." In: *Bull. Exp. Biol. Med.* 138.3 (2004), pp. 280–283. ISSN: 00074888. DOI: [10.1007/s10517-005-0021-z](https://doi.org/10.1007/s10517-005-0021-z).
- [133] A. S. Dukhin, P.J. Goetz, and T.G.M. Van de Ven. "Ultrasonic characterization of proteins and blood cells." In: *Colloids Surfaces B Biointerfaces* 53.2 (2006), pp. 121–126. ISSN: 09277765. DOI: [10.1016/j.colsurfb.2006.08.011](https://doi.org/10.1016/j.colsurfb.2006.08.011).
- [134] M. A.H. Weiser and R. E. Apfel. "Extension of acoustic levitation to include the study of micron-size particles in a more compressible host liquid." In: *J. Acoust. Soc. Am.* 71.5 (1982), pp. 1261–1268. ISSN: NA. DOI: [10.1121/1.387776](https://doi.org/10.1121/1.387776).
- [135] K.W. Cushing et al. "Ultrasound Characterization of Microbead and Cell Suspensions by Speed of Sound Measurements of Neutrally Buoyant Samples." In: *Anal. Chem.* 89.17 (2017), pp. 8917–8923. ISSN: 15206882. DOI: [10.1021/acs.analchem.7b01388](https://doi.org/10.1021/acs.analchem.7b01388).

- [136] P. Sethu, A. Sin, and M. Toner. “Microfluidic diffusive filter for apheresis (leukapheresis).” In: *Lab Chip* 6.1 (2006), pp. 83–89. ISSN: 14730189. DOI: [10 . 1039 / b512049g](https://doi.org/10.1039/b512049g).
- [137] X. Ding et al. “Cell separation using tilted-angle standing surface acoustic waves.” In: *Proc. Natl. Acad. Sci. U. S. A.* 111.36 (2014), pp. 12992–12997. ISSN: 10916490. DOI: [10 . 1073 / pnas . 1413325111](https://doi.org/10.1073/pnas.1413325111).

This Ph.D. thesis has been typeset by means of the \TeX -system facilities. The typesetting engine was $\text{Lua}\mathbb{L}\mathbb{A}\mathbb{T}\mathbb{E}\mathbb{X}$. The document class was `toptesi`, by Claudio Beccari, with option `tipotesi=scudo`. This class is available in every up-to-date and complete \TeX -system installation.